Vortex-induced vibrations in OTEC

An analysis of VIV of a cold water pipe for OTEC plants

Tim de Zwart

Vortex-induced vibrations in OTEC

An analysis of VIV of a cold water pipe for OTEC plants

by

Tim de Zwart

to obtain the degree of Master of Science
at the Delft University of Technology,
to be defended publicly on Thursday December 21, 2017 at 11:00 AM.

Student number:	4227425	
Project duration:	March 23, 2017 – December 21, 2017	
Thesis committee:	Prof. dr. A.V. Metrikine,	TU Delft, chairman
	Dr. H. Hendrikse,	TU Delft, daily supervisor
	Dr. K.N. van Dalen,	TU Delft
	Ir. B.J. Kleute,	Bluerise

Preface

This report contains the results of my graduation project for the Delft University of Technology, conducted for Bluerise. The research has been completed in the time period from March 2017 until December 2017 in order to obtain the Master of Science degree in Offshore & Dredging Engineering at the Faculty of Civil Engineering and Geosciences.

The report is a result of studied literature, own input and many meetings with committee members. I would like to thank my daily supervisor Hayo Hendrikse for always being patient enough to answer my questions, providing me with knowledge and valuable advise and guiding me through the process of completing this thesis. I would like to thank Andrei Metrikine for taking his time to explain to me the mathematics behind the final part of this research and helping me push a little bit further in order to make this a more complete and valuable work. Finally, I would like to thank Bluerise, and more specifically Berend Jan Kleute, for giving me the opportunity to conduct this research in their name and providing me with the idea for the scope of this work.

Tim de Zwart,
Delft, December 2017

Summary

Climate change has become a very serious issue and the need to find renewable and clean energy sources has grown larger and larger. Sources like solar power and wind have all widely been studied, discussed and tapped, but the field of ocean energy has not yet risen to the same level yet. One way to harness energy from the ocean with, theoretically, very high potential is ocean thermal energy conversion (OTEC). This means that a long large diameter pipe is deployed into the ocean to pump up cold water from the bottom ocean layer, while the warm water from the top ocean layer is pumped up as well to power a Rankine cycle, yielding energy.

The problem with pipes in the ocean is that as the ocean water flows past the pipe with a certain current velocity, a phenomenon called vortex-induced vibrations (VIV) might occur, potentially leading to very large oscillations. These oscillations cause forces and high amplitude stress cycles that might lead to severe fatigue damage after a certain amount of time. The aim of this thesis was to analyse these VIV in an OTEC cold water pipe numerically, and to quantitatively discuss the impact of several variables on VIV, such as pipe material, pipe properties, inflow velocity and current velocity.

A short history of OTEC was given to introduce the subject, after which the theory behind VIV was explained. This theory is the fundament of the model that was later set up for the numerical analysis. The pipe was modelled as a fluid conveying Euler-Bernoulli beam with tension varying over the depth. Since the pipe is symmetrical, both degrees of freedom have an equation of motion of the same form. The VIV were modelled using a wake oscillator equation, coupled to the system through the acceleration terms, yielding a set of three partial differential equations.

In order to make the system suitable to be analysed using a numerical solver, the system had to be rewritten into a set of ordinary differential equations (ODEs). Therefore, the equations were discretised over its depth using finite differences, dividing the pipe in multiple nodes. The system of equations was then rewritten into state-space representation, meaning that a set of six ODEs had to be solved for each node. This was done using Python's *odeint* package. The model that was written for this gave multiple useful outputs, of which the most important ones were the natural frequencies and the displacements. These displacements could be used to calculate other useful outputs as forces, moments, stresses and the fatigue damage per year.

In order to check whether the model performed as expected, first a test run was done with a typical steel riser and then with a typical HDPE OTEC pipe. After it was confirmed that the model outputs turned out as expected, the cold water pipe was analysed with different sets of variables. The most significant outcomes were that HDPE is by far the most suitable material for a large sized OTEC cold water pipe due to its fatigue resistance and relative strength. Even at large diameters up to 6.0 m the pipe would not suffer significantly from fatigue. Another significant observation was that the pipe could best be tensioned by a heavy ballast mass, since the effect of suppressing VIV through larger stiffness was more critical than the danger of the pipe yielding from the mass. A final observation was that when the current velocity becomes high, the pipe will most probably suffer from the in-line bending stress due to the displacement caused by drag force and not of vortex-induced vibrations.

Finally, an extra research was set up concerning the stability of the pipe if the inflow velocity varies over time. This might potentially be interesting as it could be used to suppress transverse pipe vibrations. To do this, the pipe model was simplified into the model of a cantilever beam with time varying inflow. Using modal analysis and the one-mode approximation, the model is rewritten into a single degree of freedom system with a periodic coefficient matrix. Floquet theory was then used to find a combination of inflow velocity amplitude and a frequency of change for which the system is stable.

Contents

1

Introduction

Over the course of ages, the climate has drastically changed and as of yet we live in an age where we no longer take our life on earth as it currently is for granted. We feel we have gone on in our 19th-century-hydrocarbon-burning-ways for too long and that it's finally time for a change. Former President of the United States Barack Obama has famously called climate change the "one issue that will define the contours of this century more dramatically than any other" [1]. Meanwhile, around 97% of scientists consent on the fact that humans have had an influence on this climate change [2], resulting in the rise of global temperature and sea levels, and deteriorating air quality. The message is clear, we need to change our ways and rapidly so. If we want to leave this earth to our descendants in a habitable state, we have but one choice and that is to start innovating and restructuring our energy market. We need to stop burning fossil fuels and start searching for durable and clean means of producing energy.

The search for these renewable energy forms is alive and ongoing and there are possibilities aplenty: solar power, wind power, biomass fuel, hydropower and geothermal energy have all been universally researched and applied. According to the Global Status Report 2016 by REN21 [3], as of 2016 renewables made up 23.7% of the global energy production, compared to 19.2% in 2015. This indicates that steps in the right direction are being made, but also that there is still a lengthy way to go. Additionally, the report shows that one of the largest energy sources remains relatively untapped, to wit the ocean.

The ocean alone offers up a great variety of renewable energy sources. Tidal streams can drive turbines to yield large amounts of clean energy, converters can be used to harness the energy of wave motions and the saline water in oceans can be used for producing power from the salinity gradient between salt and fresh water, or so-called blue energy. However, the largest potential might be found in the conversion of thermal energy, or OTEC (Ocean Thermal Energy Conversion). The potential of merely OTEC could reach up to 7 TW without unacceptable effects on ocean temperatures [4], which would be more than sufficient to cover the entire global energy consumption. The process of OTEC is simple, clean and durable and can be applied at any location with a temperature difference of around 20 degrees Celsius between top and bottom water layer. Warm water is extracted from the near-surface of the sea, while a large pipe pumps up cold water from the bottom layer of the sea. The exchanged heat is then used to drive a Rankine cycle as pictured in Fig. 1.1, leading to a significant electricity output. This technology is ideal for harnessing the solar power absorbed by the ocean, and is available continuously during both day and night. This means that the power is readily available whenever it is needed, and unlike wind or solar power, it doesn't come in large amounts with regular intermissions, making the need to store the power rather redundant [5].

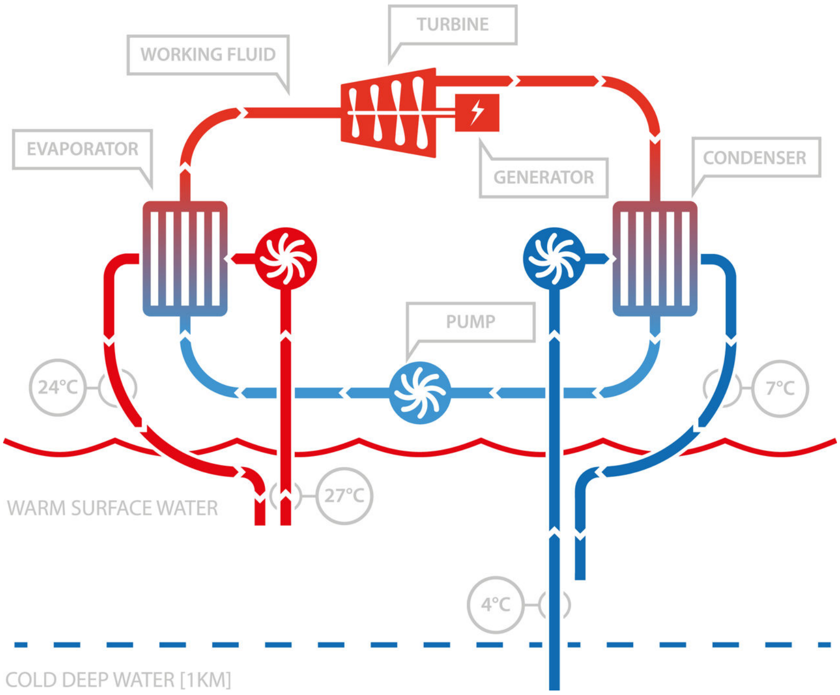

Figure 1.1: Typical OTEC cycle [5]

1.1. General introduction, scope and aim

Ocean thermal energy conversion, as has been introduced shortly before, is one of plenty possibilities to make a shift towards cleaner energy, and it has an enormous theoretical potential. Therefore it is worthwhile to investigate this form of energy conversion and all its difficulties. Hence, OTEC will be the focus of this thesis.

The main difficulty in OTEC lies in the fact that in order to reach economic feasibility, the scale on which the energy is conversed should be very large. This means, more specifically, that the pipe that reaches into the depth of the ocean to pump up the cold water has to be of a size that is not present yet in other offshore operations. For good measure, the largest risers that are typically used in offshore operations are of a size around 0.45-0.50 m (18-20 inch), whereas the typical size of an OTEC cold water pipe will have to be in the range of 2.5-4 m [6]. This means no experience can be drawn from prior knowledge in fabrication techniques, installation or typical pipe behaviour and forces.

As of yet, multiple parties are investigating OTEC and interest in the subject is surging as climate change and exhaustion of hydrocarbons becomes more and more of an issue. Companies are trying to find ways to make larger pipes while tests and studies are being conducted in order to check the feasibility of OTEC, as for example in the study by Acevedo et al. [6]. This thesis draws extensively from that study and tries to take it in a direction that has still remained quite unexplored. The main aim of this thesis is to evaluate the vortex-induced vibrations (VIV) in the cold water pipe of an OTEC plant. VIV may arise as a current flows along a cylinder and vortex shedding occurs in the wake of the pipe. Due to the asymmetrical nature of these vortices, a periodic lift force may cause the cylinder to start vibrating and this phenomenon is known as vortex-induced vibrations. VIV are an omnipresent problem in civil and offshore engineering and therefore knowledge on this is widely available. In OTEC however, it's an issue that has not been evaluated very often.

This thesis will start of with a short history of OTEC and an introduction to the theory behind vortex shedding and wake interaction with the structure. This theory will then be used for the main aim of this thesis , applying the VIV theory to an OTEC cold water pipe and investigating the behaviour of the pipe as it is exposed to a current of a certain magnitude that may cause vibrations. The influence on the pipe behaviour of various parameters as different materials, diameters and current velocities will be analysed. This will be done by developing a model in Python in which the parameters can be implemented and changed, leading to a clear image of the displacement of the pipe at every point in the pipe. The displacements serve for calculating forces and stresses in the pipe, leading eventually to an estimate of the fatigue and life expectancy. Finally, a different approach is used to analyse the system's stability when dealing with an inflow velocity varying over time.

In summary, the aim of this project can be defined as gaining a clear insight in a problem that has been relatively unexplored in previous OTEC studies as for example the study by Acevedo et al. [6]. The theory behind VIV is readily available and can easily be applied to a typical OTEC plant. This thesis will present an overview of the influence of various parameters that are relevant in OTEC on VIV, hopefully contributing in facilitating the development of this technique.

1.2. Motivation

The motivation behind conducting this thesis follows directly from the introduction and aim of the previous section. Climate change is a serious problem that needs to be dealt with without any further hesitation. Therefore, the search for renewable energy sources is of great importance and OTEC has an enormous potential. This thesis is therefore dedicated to further exploring the field of OTEC and contributing a small piece to the entire OTEC development.

1.3. Contents

This report is set up in a way that will first introduce the subject and establish a fundamental understanding of the theory, after which the obtained knowledge is used to perform the further research. After this Chapter 1, in which the aim and motivation of this thesis are explained, Chapter 2 will give an introduction of OTEC in general, and explain the theory behind VIV. In Chapter 3 the model for the cold water pipe is described. Chapter 4 shows how this model can be rewritten in order to make it suitable for software implementation, and it elaborates upon the outputs and the different variables that will be analysed. The results from the analyses done with this model will be presented in Chapter 5. Finally, Chapter 6 will analyse the stability of the pipe with a time varying inflow velocity.

2

General background

This chapter serves as a general introduction of the history and knowledge that was present and available before conducting this thesis. It draws the background for this research, gives a review of the current state of the art and presents all the different subjects that this thesis will touch. It starts off with a short history of ocean thermal energy conversion in general and a summary of the current state of events, in order to make the reader more familiar with the matter and build the frame in which the results obtained in this thesis can be placed. After this, the subject of vortex-induced vibrations is introduced, explaining the theory behind it and providing an overview of the models that are currently used to imitate this natural behaviour.

2.1. Ocean thermal energy conversion

This section is dedicated to OTEC in general. At first a chronological timeline of the history of OTEC is given, eventually leading to the current state of events. This part is followed by a more thorough elaboration on the present, the technique that is available today and the future.

A short history of OTEC

The first ever documented mention of OTEC was made by French novelist Jules Verne, in his 1870 science fiction novel *Twenty Thousand Leagues Under the Sea* [7]. In the book, Captain Nemo proposes powering his submarine by plunging two wires into different depths, harnessing electricity from the temperature difference. However, it is another Frenchman, a physicist by the name of Jacques-Arsène d'Arsonvale, who is credited for coming up with an actual concept for OTEC in 1881 [8]. His idea was that of a closed-cycle system, where a working fluid, for example ammonia, is vaporised by the heat of the warm ocean surface water, creating steam that powers a turbine. The cold water pumped up from the depths of the ocean, is then used to reliquify the working fluid after which the closed-cycle starts again, assuring a continual process of vaporisation and reliquefaction. A schematic overview of this closed cycle, that is the prevailing design in current OTEC ventures, has been shown in Fig. 1.1. It took Georges Claude, one of d'Arsonvale's students, until 1930 to realise the first working OTEC plant in Matanzas, Cuba [9]. It produced up to 22 kWh after which it was destroyed in a storm. Claude opted for an open cycle design where the warm sea water was directly evaporated, expanding the vapour through a low pressure turbine and finally condensing the sea water again and discharging it back in the sea [10]. A schematic overview of this open cycle, more famously known as the Claude cycle can be found in Fig. 2.1.

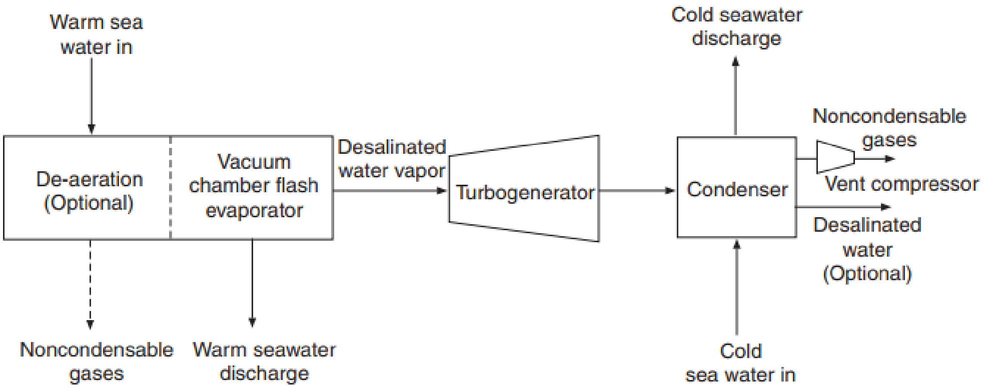

Figure 2.1: Schematic overview of Claude's open cycle [10]

Claude continued his efforts by installing a plant aboard a moored cargo vessel off the coast of Brazil in 1935, however it was destroyed before it started generating net power. After this deception Claude took up the challenge once more in 1940, when he started the development of a 3 MW plant along with a group of his students which was to be placed in front of the coast of Abidjan, in modern day Ivory Coast [11]. Once again this project did not reach completion as a large amount of oil came readily available in the region and the French government did no longer see the value of Claude's OTEC efforts, abandoning the project in 1955. Georges Claude died in 1960 at the age of 90, after dedicating most of the second part of his life to OTEC.

As one of its greatest pioneers died in Claude, the idea of OTEC however did certainly not. In the United States a doctor by the name of J. Hilbert Anderson evaluated the works of Claude and identified its problems. The main thing he found was that the cost was too high due to the use of a low pressure turbine, which needed massive amounts of gas to pass through it in order to generate feasible amounts of power. Therefore he proposed a new system with a closed cycle, as has been described before. Using a working fluid that evaporates easily under low pressure, a more powerful turbine could be used leading to larger amounts of generated energy. This Anderson cycle was patented in 1964 [11].

Although the efforts of Claude and Anderson where essential for the development of the concept, interest in the subject really surged when the Japanese picked up the idea of OTEC in the early 1970's. Universities, governmental institutions and private companies expressed great interest setting up research on a larger scale. A company called Tokyo Electric Power Services took it upon themselves to deploy a 120 kW plant on the island republic of Nauru in the Pacific Ocean [11]. Since the energy converted here was used to power schools and other services it became the first practical OTEC plant.

The next great development came in 1981, when the Russian engineer Alexander Kalina introduced a new cycle that made use of a mixture of ammonia and water, as opposed to the previous cycles which needed a pure substance as working fluid [12]. This cycle became the new standard for the, mainly Japanese, developments in the following years. A 50 kW plant was constructed in 1982 and in 1985 a larger version of this experimental setup was constructed, producing up to 75 kW. It was also in this year that Haruo Uehara and his team managed to create a hybrid cycle, which combined OTEC's main intent of energy conversion with the desalination of sea water, giving OTEC a broader purpose. Uehara proceeded his efforts and introduced his own cycle, the Uehara cycle, in a 4.5 kW test project at Saga University in Japan. The cycle was found to be able to outproduce the Kalina cycle by 1-2% [12]. Saga University became one of the most important institutes for OTEC research and signed an agreement with the National Institute of Ocean Technology of India to deploy a 1 MW floating plant. This endeavour never came to a successful conclusion as the deployment of the 1 m diameter cold water pipe failed, showing the importance of this segment of the OTEC concept [12].

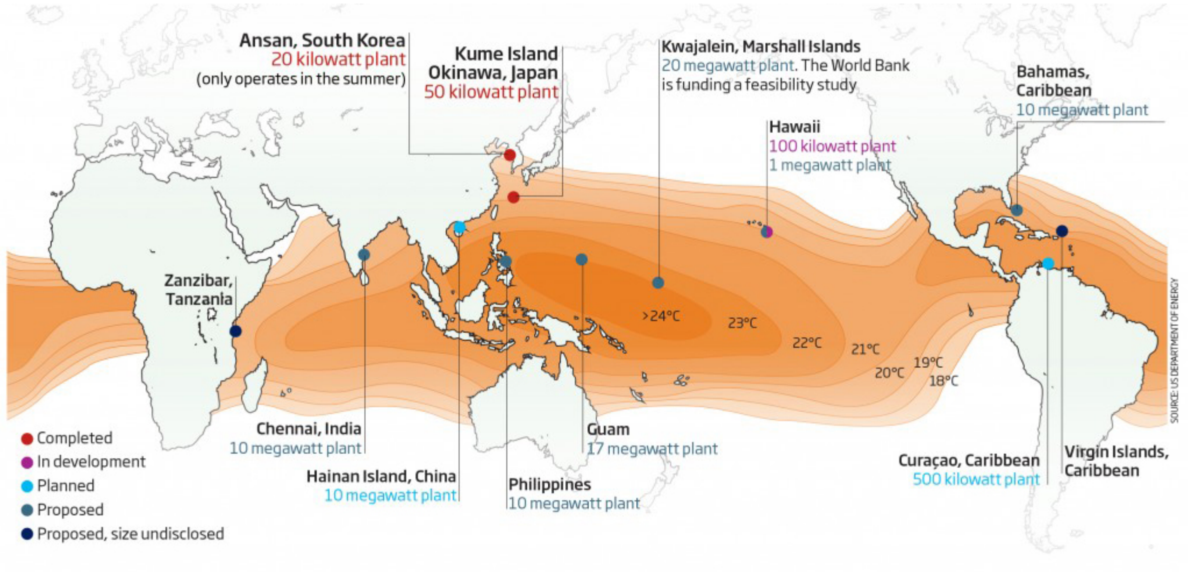

Figure 2.2: Overview of operating and planned OTEC plants [7]

Although the hotbed of research and development of OTEC in the last four decades was Japan, the technology gained a small surge of interest in the United States, after the oil prices skyrocketed in the aftermath of the Arab-Israeli war of 1973 [13]. The federal government reserved an amount of $260 million to OTEC research, but this did not continue into Reagan's presidency in the 80's. This sudden interest, albeit short-lived, still led to some major developments like the establishment of the Natural Energy Laboratory of Hawaii Authority (NELHA) in 1974. Since Hawaii is a prime location for OTEC due to it's sea temperature gradient, this became the leading research centre in the United States. Furthermore, it led to a cooperation between two major companies, Lockheed Martin and Hawaii-based Makai, an OTEC-inspired cooperation that still lasts to this day. Together, they were responsible for several small to medium scale test cases, keeping the OTEC business alive over the past decades.

Current developments and state of technology

Today, the OTEC industry is as thriving as ever. Institutes as Bluerise, NELHA, Saga University, Makai and Lockheed Martin continue to innovate, research, test and develop and as the concern of climate changes grows, renewable and sustainable energy forms gain more and more interest. Besides energy conversion, the purpose of the OTEC industry has broadened to also include desalination of sea water, as has been mentioned before, and in 2017 the first sea water air conditioning (SWAC) system is to be installed in the Bahamas' Baha Mar resort. Since 2014, two small scale plants (20 kW and 50 kW respectively) have been operating in South Korea and Japan, and multiple projects up to a larger scale of 10 MW are planned. A full overview of running, planned and proposed projects can be found in Fig. 2.2.

The technology of today reaches a thermal efficiency of around 3.5% [6]. Although this may sound low, it has to be considered that the "fuel" for OTEC is essentially free and ever present (the solar power stored in sea water). Furthermore, the conversion of energy can be combined with other goals as SWAC and desalination. Since the largest potential for OTEC is in regions that are in general not very wealthy, it proves a great opportunity for less affluent island states to harness their own energy. The incredibly large theoretical potential of OTEC has been discussed before and is pictured in Fig. 2.3.

The scale of the projects that have been successfully operating up till now is too small for commercialisation of the technology. Therefore, yet more research has to be conducted in order to prove the scalability of these smaller operations. The main challenge is the offshore equipments, or more specifically the cold water pipe. Currently offshore arrangements do not yet exist in the size that is needed in order to make OTEC a commercially viable option [6]. The cold water pipe has to be of a diameter that is large enough to pump up significant amounts of water. This means difficulties in production, installation, the weight of the pipe, the forces in the pipe as it vibrates and the stability of inflow in the pipe. If these difficulties can be overcome however, OTEC will have a bright future and will play a significant role in our shift towards a cleaner and more sustainable world.

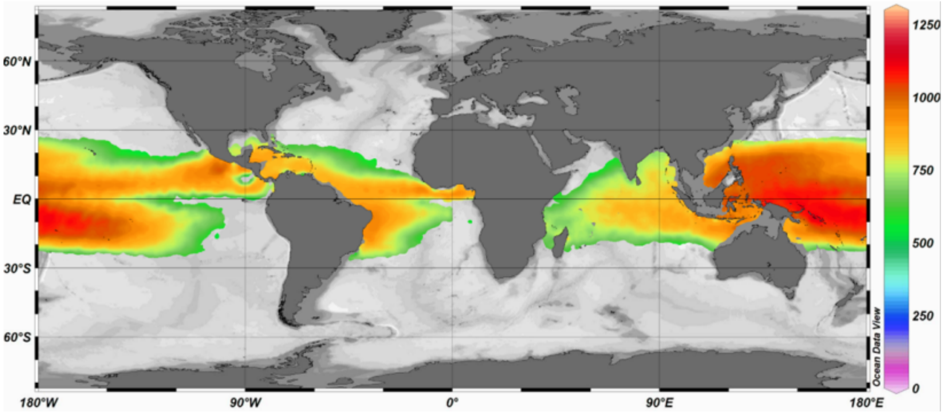

Figure 2.3: Estimated theoretical potential of OTEC worldwide in kW/m^2 [6]

2.2. Vortex-induced vibrations

This section deals with the other main aspect of this thesis, to wit vortex-induced vibrations (VIV). It explains the theory behind vortex shedding as a steady current flows along a bluff body, and behind the vortex-structure interaction that causes the so-called VIV phenomenon. Additionally, this section elaborates on why this is important for this thesis and how it can be modelled.

Vortex shedding

Vortex-induced vibrations, or flow-induced motions in general, are the motions that occur as a steady current flows along a body. As the fluid particle approaches the body, it reaches a point where all kinetic energy is converted in pressure energy and the pressure causes the particle to flow around the body, creating two boundary layers. At higher Reynolds numbers, these vortex layers will at a certain point shed from the body. Since the outermost part, which is in contact with the free moving fluid, moves significantly faster than the innermost part, which is in contact with the body, the layers will rotate into the wake. This swirling motion of the separated layer into the wake is called a vortex. As multiple vortices form at a certain frequency (the vortex shedding frequency) and trail each other in the wake, a so-called vortex street is created. Since this vortex street is asymmetrical, an irregular pressure distribution over the body is created, resulting in a lift force perpendicular to the direction of the flow. Due to the periodical nature of vortex shedding, the lift force will also vary periodically which will lead to an oscillatory motion of the body. This phenomenon is called vortex-induced vibration [14].

Reynolds number and Strouhal number

As mentioned before, whether a vortex sheds from a body or in this case a smooth cylinder depends on the Reynolds number. The Reynolds number is a dimensionless physical quantity that is used to predict flow patterns and vorticity in fluid flows, and it is defined as:

$$\mathrm{Re} = \frac{UD}{\nu} \quad , \tag{2.1}$$

where U is the velocity of the flow, D is the diameter of the cylinder and ν is the kinematic viscosity (generally $1.1 \cdot 10^{-6}$ m^2/s for seawater).

Fig. 2.4 shows the different regimes of fluid flow around a cylinder and their corresponding Reynolds numbers. For very low Reynolds numbers of $\mathrm{Re} < 5$ the flow will follow the shape of the body without separating from it. In the regime of $5 \leq \mathrm{Re} < 40$, vortices can first be seen as two fixed vortices form in the wake of the body. Then, as the Reynolds number further increases, the length of the vortices increase linearly and eventually the wake will become unstable and the vortices break away, forming a laminar vortex street. The vortices start becoming turbulent in the range of $150 \leq \mathrm{Re} < 300$, reaching full turbulence when $300 \leq \mathrm{Re} < 3 \cdot 10^5$, the so-called subcritical range. The laminar boundary layer undergoes a turbulent transition in the transitional range $\left(3 \cdot \mathrm{Re} < 3.5 \cdot 10^6\right)$, leading to a narrow and disorganised wake. For Reynolds numbers of $\mathrm{Re} \geq 3.5 \cdot 10^6$ the vortex street is re-established with a turbulent boundary layer [14]. For illustration, this means that for a riser of typical diameter (0.4 m), vortex shedding might occur for flow velocities as low as 0.0002 m/s ($\mathrm{Re} \approx 72$). For

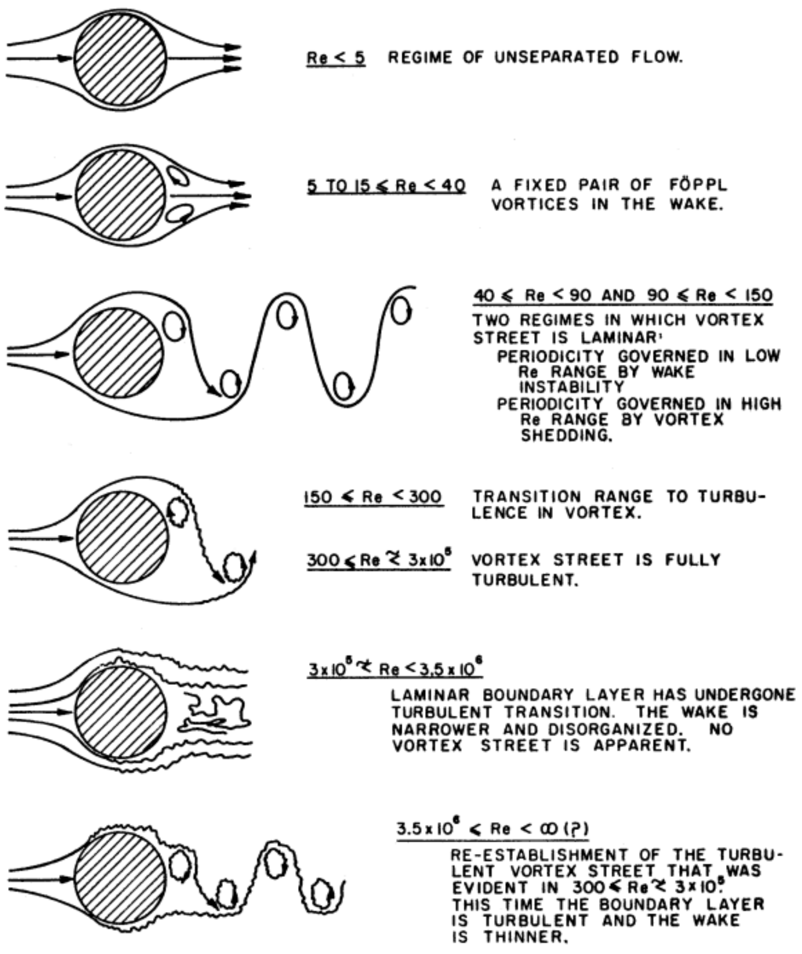

Figure 2.4: Overview of flow regimes and corresponding Reynolds numbers [14]

the case of the OTEC cold water pipe, which will typically have a diameter of 2.5-4 m, at a relatively low fluid flow velocity of 0.1 m/s, the Reynolds number will range between $2 \cdot 10^5 < \mathrm{Re} < 4 \cdot 10^5$, which means that VIV is a very real possibility.

Another very important parameter when investigating VIV, is the Strouhal number. As the Reynolds number, the Strouhal number is a dimensionless physical quantity. It relates the frequency in which the vortices shed to the fluid flow velocity and the diameter of the body:

$$f_s = \frac{\mathrm{St}\,U}{D} \quad , \tag{2.2}$$

where f_s is the vortex shedding frequency in Hertz. Lienhard [15] used empirical data to relate the Strouhal number to the Reynolds number, as depicted in Fig. 2.5. From this picture it can be seen that for a large range of Reynolds numbers (approximately $300 < \mathrm{Re} < 2 \cdot 10^5$) the Strouhal number is more or less constant at $\mathrm{St} \approx 0.2$. Since this range largely covers the regimes in which vortex shedding occurs, the Strouhal number is often assumed around $\mathrm{St} \approx 0.2$ in VIV research.

Vortex-structure interaction and lock-in

As a cylinder starts vibrating due to vortex shedding, the state of the fluid alters which induces several side effects. It might lead the vortices to increase in strength, the behaviour of the wake might change, but most importantly it might lead to lock-in. When the vortex-shedding frequency approaches one of the natural frequencies of the structure, it might cause the vortex shedding frequency to lock on to this natural frequency, leading to oscillations of large amplitudes. This phenomenon is called lock-in. It is one of the biggest problems in VIV, since even at low current velocities, the phenomenon might occur leading to large and possibly

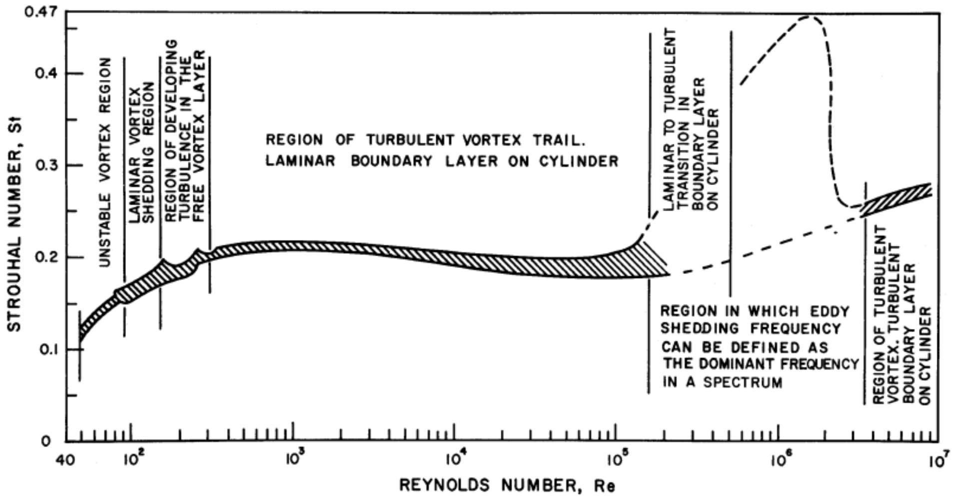

Figure 2.5: Relationship between Strouhal number and Reynolds number defined by existing data [15]

devastating vibrations. A useful tool to describe the characteristics of lock-in is the reduced velocity, which is defined as:

$$U_r = \frac{U}{f_n D} \simeq \frac{1}{\mathrm{St}} \quad , \tag{2.3}$$

where U_r is the reduced velocity and f_n is the natural frequency of the structure. Since in case of VIV the system is locked in, $f_s \simeq f_n$, which means that U_r can be expressed in terms of the Strouhal number as $U_r \simeq 1/\mathrm{St}$. From Fig. 2.5 it might be recalled that in general this means that lock-in occurs where $U_r \approx 5$. However, from large amounts of empirical data retrieved from a plethora of researches, it can be assumed that lock-in will generally occur in the range of $4 \leq U_r \leq 10$ [16]. In terms of frequency, this means that lock-in might occur at vortex shedding frequencies in the range of $f_s \approx 0.5 f_n$ up to $f_s \approx 1.25 f_n$.

VIV modelling

There are multiple approaches to modelling vortex-induced vibrations and over the course of history, a wide variety of models has been studied and proposed, of which a comprehensive overview is given by Gabbai and Benaroya [17]. The *semi-empirical models* consist of three classes; (i) the single degree-of-freedom models which use a single dynamic equation on the right-hand side of the equation (ii) the force-decomposition models which rely on the measuring of certain force components on the structure from experiments (iii) the wake-body coupled models where the body is coupled with the wake oscillations through common terms in the equation. A different approach to modelling VIV is the *numerical method.* The vortex-in-cell method is a complex method where the flow field is described by a cloud of moving vortex elements. Other options are direct numerical simulation and the finite element method. However, due to the immense difficulty and computational limitations of the numerical treatment of turbulent and high Reynolds number flows, in engineering the semi-empirical approach is preferred. Therefore, only the semi-empirical models will be further elaborated in the following sections. It is to be noted that for the sake of correspondence with the references, the notation of equations is preserved as given in said references. They will, however, be conformed with the notation of this work in a later stage.

Single degree-of-freedom models

An example of a single degree-of-freedom model is for example the general equation for a bluff body oscillating in fluid derived in the work of Bearman [18]:

$$M\ddot{y} + 4\pi N_0 \delta_s M\dot{y} + 4\pi^2 N_0^2 M y = C_y \rho U^2 D/2 \quad , \tag{2.4}$$

where M is the mass per unit length of the body, y is the displacement in transverse direction, N_0 is the undamped natural frequency of the body, δ_s the fraction of critical damping and C_y is the transverse force coefficient on a bluff body shedding vortices. In general, the force and body displacement will oscillate at the same frequency, n_v, which will be close to N_0. The fluid must lead the excitation of the body by a certain phase angle ϕ, thence leading to the representation of y and C_y:

$$\begin{aligned} y &= \bar{y}\sin 2\pi n_v t \quad , \\ C_y &= \bar{C}_y \sin\left(2\pi n_v t + \phi\right) \quad . \end{aligned} \tag{2.5}$$

Force-decomposition models

According to Gabbai and Benaroya [17], the first force-decomposition model was introduced by Sarpkaya [19] in which he decomposed the force in a fluid inertia force related to the cylinder displacement and a fluid damping force related to the velocity of the cylinder. The lift force coefficient C_L in this model is expressed as:

$$C_L = C_{ml}\pi^2 \frac{U_m T}{D}\left(\frac{D}{\bar{V}T}\right)^2 \sin\{\omega t\} - \frac{8}{3\pi}C_{dl}\left(\frac{U_m T}{D}\right)^2\left(\frac{D}{\bar{V}T}\right)^2 \cos\{\omega t\} \quad , \tag{2.6}$$

where C_{ml} is the inertia coefficient, C_{dl} is the drag coefficient, T is the period of the transverse motion of the cylinder, $U_m = 2\pi A/D$ and the reduced velocity $V_r = \bar{V}T/D$, where A is the maximum motion amplitude of the cylinder and $\bar{V}$ is the velocity of the ambient flow. Implementing Eq. (2.6) in the general equation of motion of an elastically mounted cylinder yields the model:

$$\ddot{x}_r + 2\zeta\dot{x}_r + x = \rho_r\Omega^2\left(C_{ml}\sin\{\Omega\tau\} - \frac{16}{3\pi^2}X_r C_{dl}\cos\{\Omega\tau\}\right) \quad , \tag{2.7}$$

where $x_r = x/D$, Ω is the ratio of the oscillation frequency of the cylinder to its natural frequency f_c/f_n, ρ_r is the ratio of the fluid density to the cylinder density ρ_f/ρ_c and $\tau = \omega_n t$.

A model where the fluid force is decomposed in a excitation part and a reaction part was introduced by Griffin and Koopmann [20]. The non-dimensional equation of motion for this model is defined as:

$$\ddot{y} + 2\omega_n\zeta_s\dot{y} + \omega_n^2 y = \mu\omega_s^2\left(C_L - C_R\right) \quad , \tag{2.8}$$

where C_L is the lift coefficient, C_R is the reaction coefficient, ω_s is the Strouhal vortex-shedding frequency, ζ_s the viscous damping of the structure and μ a certain mass parameter.

Wake-oscillator models

A way of modelling the fluctuating nature of the vortex street is by using a van der Pol equation as defined by Facchinetti et al. [21]:

$$\ddot{q} + \varepsilon\Omega_f\left(q^2 - 1\right)\dot{q} + \Omega_f^2 q = F \quad , \tag{2.9}$$

where q is a dimensionless wake variable used to determine the motion of the wake and ε is a dimensionless tuning parameter. Following these lines of Facchinetti et al., the following set of coupled dimensional equations was defined by Ogink and Metrikine [22] to describe both the motion of the structure and the oscillation of the wake:

$$(m + m_a)\ddot{Y} + b\dot{Y} + kY = \frac{1}{2}\rho D V^2 L C_{VY} \quad , \tag{2.10}$$

$$\ddot{q} + \varepsilon\omega_s(q^2 - 1)\dot{q} + \omega_s^2 q = \frac{A}{D}\ddot{Y} \quad , \tag{2.11}$$

where m_a is the added mass, b is a damping coefficient and k a certain restoring coefficient of the cylinder. A is a dimensionless tuning parameter, as is ε. C_{VY} is the cross-flow force and the right hand side of Eq. (2.11) is an acceleration coupling term. Further substitution and implementation of terms by Ogink and Metrikine [22] leads to the final set of coupled non-dimensional equations:

$$\ddot{y} + 2\zeta\Omega_n\dot{y} + \Omega_n^2 y = \frac{\rho D^2 L}{(m + m_a)}\frac{1}{8\pi^2\,\mathrm{St}^2}C_{VY} \quad , \tag{2.12}$$

$$\ddot{q} + \varepsilon\left(q^2 - 1\right)\dot{q} + q = A\ddot{y} \quad , \tag{2.13}$$

where the reduced damping $\zeta = b/(2\omega_n(m+m_a))$, natural frequency $\Omega_n = (k/(m+m_a))^{\frac{1}{2}}/\omega_s$ and St is the Strouhal number.

Literature

Since VIV has been a point of interest for several centuries, the literature on the phenomenon is abundant. This chapter contains the most relevant aspects of the theory for this thesis. However, a lot more than is mentioned here has been written about dependency on parameters, lift and drag coefficients, means of modelling and many other aspects. Blevins [14] wrote a work that includes all the fundamental basics of fluid flow and the motions it induces. Williamson and Roshko [23] wrote a comprehensive review of the nature of vortex shedding and its effects. Sarpkaya [24] focused his extensive overview on the intrinsic nature of VIV. Gabbai and Benaroya [17] compiled an overview of experiments and models on VIV. These works can all be consulted in case things are unclear, and they make up only a tiny part of the complete amount of available work on this subject.

Suppression measures

As the phenomenon of vibrations induced by vortex shedding has been a known problem for ages, people have been looking for measures to suppress these vibrations with great vigour. This has led to an extensive knowledge of the characteristics of VIV and a wide variety of both hydrodynamic and aerodynamic means of suppression. In an extensive overview, Zdravkovich [25] has classified them into three categories; (i) surface protrusions (ii) shrouds (iii) near-wake stabilisers.

Surface protrusions

Examples of the application of surface protrusions are helical strakes, wires, studs and fins. The surface protrusions will affect the separation lines and separated layers, denying the vortices from forming. The protrusions can either be applied omnidirectional or unidirectional. An overview of possibilities for surface protrusions can be found in Fig. 2.6. Surface protrusions are omnipresent in practice, with helical strakes being the most common solution at the moment since they are robust and relatively easy to install. However, surface protrusions have been known to increase drag [26].

Shrouds

Examples of the application of shrouds are perforated shrouds, gauze and axial rods and slats. The shrouds will meddle with the rotation of the fluid, denying the vortices from forming. An overview of possibilities for shrouds can be found in Fig. 2.7. Shrouds are not very common since they require a great amount of material and are very inconvenient, especially for structures of such great length as the structures that are prevalent in the offshore industry.

Near-wake stabilisers

Examples of the application of near-wake stabilisers are splitter plates, saw-tooth plates, guiding plates and guiding vanes. The near-wake stabilisers affect the interaction of the entrainment layers in the confluence point, denying the vortices from forming. An overview of possibilities for near-wake stabilisers can be found in Fig. 2.8. Although near-wake stabilisers are more effective in both VIV response and drag reduction than surface protrusions, they are significantly harder to install and to handle, along with being more expensive. Additionally, they tend to cause galloping at higher current velocities [26, 27].

Fairings

Another method of suppressing the vortex-induced vibrations of a pipe, is outfitting the pipe with a free-to-rotate suppression near-wake stabiliser, called a fairing. The main advantage of a fairing over other suppression devices is that, as mentioned in Section 2.2, where helical strakes increase the drag force on a cylinder [26], the fairing both suppresses the VIV and decreases the drag force [28]. Due to the typical teardrop geometry of the fairing, the flow follows a streamlined pattern, resulting in lower drag forces [27]. A typical cross-section of a fairing can be found in Fig. 2.9. An issue that has recently been found to occur with the fairing is however its tendency towards instability. [26, 29].

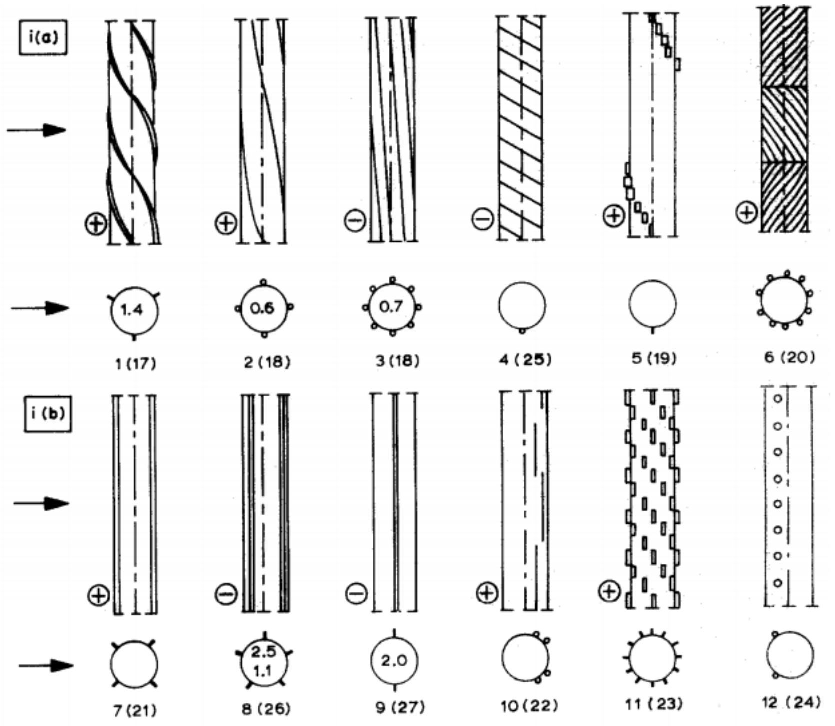

Figure 2.6: Overview of possible surface protrusions used for interfering with vortex shedding in (a) omnidirectional configuration and (b) unidirectional configuration [25]

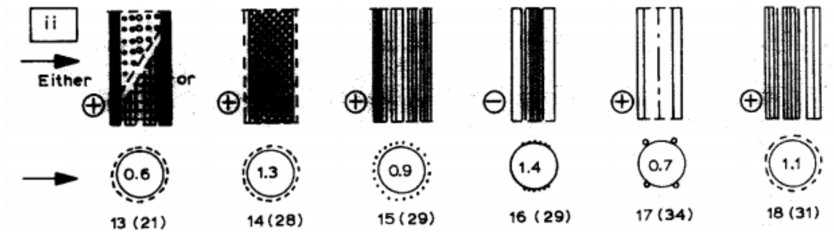

Figure 2.7: Overview of possible shrouds used for interfering with vortex shedding [25]

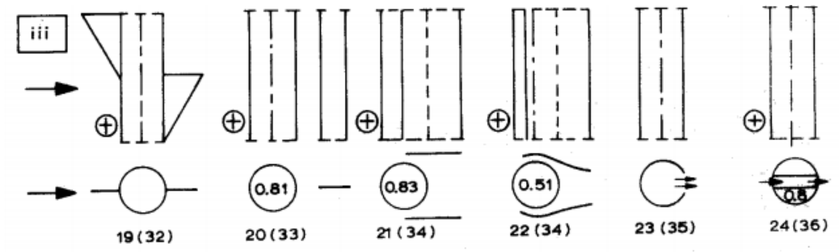

Figure 2.8: Overview of possible near-wake stabilisers used for interfering with vortex shedding [25]

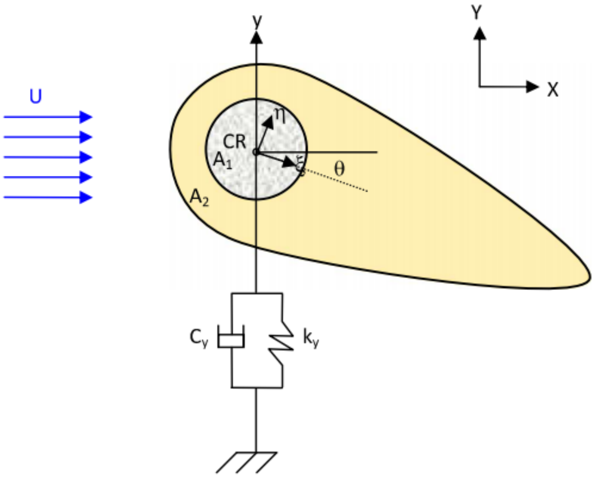

Figure 2.9: Typical cross-section of teardrop-shaped fairing, including coordinates and degrees of freedom [27]

3

Modelling of the cold water pipe

In order to achieve the main goal of this thesis, to wit giving a comprehensive overview of the possible VIV of the cold water pipe of an OTEC-plant, this pipe first has to be modelled. Creating a realistic pipe model will provide the opportunity to apply the known theory of VIV modelling to this particular case. The end goal is to create a model with multiple changeable variables and parameters so a vast amount of different scenarios can be analysed with relative ease. This chapter starts off with all the constraints and made assumptions that led to the eventual model of this pipe. Then the governing set of equations is provided in all the relevant directions. Finally, the chosen VIV model is applied and discussed.

3.1. Model basis and assumptions

In order to make a realistic yet simple and utilisable model for the cold water pipe, several assumptions have to be made. The most important of these assumptions are listed here:

- The length of pipe and the wavelength of deformation are large in comparison to the diameter of the pipe, so Euler-Bernoulli beam theory is applicable for the bending of the pipe.
- The bending motion of the pipe around its equilibrium is assumed to be small.
- The pipe wall behaves elastically and no internal is damping considered.
- The mean flow velocity along the pipe is constant.
- The pipe will always be fully submerged.

This means that the pipe can be modelled as a cantilever Euler-Bernoulli beam conveying fluid. This type of pipe model has been documented by for example Païdoussis and Li [30] and Kuiper [31], and can be assumed valid. The pipe is modelled in a Cartesian coordinate system where x- and y-direction are the directions in the horizontal plane and z-direction is the out of plane vertical direction. Further notable assumptions are that in order to make sure that only the vibrations induced by vortex shedding are evaluated the top connection of the pipe is considered static (displacement of vessel is zero in all directions), that the pipe extension and displacement in z-direction is not considered and that since this is merely a theoretical endeavour, unrealistic situations in terms of pipe diameters, velocities and other parameters might be considered as well.

3.2. Governing equations x-direction

The assumptions made in Section 3.1 are considered. The equation of motion for a pipe conveying fluid, as depicted in Fig. 3.1, is widely researched and discussed, and can thence be given as defined by for example Kuiper [31]:

$$\begin{aligned} &EI\frac{\partial^4 u(z,t)}{\partial z^4} - \frac{\partial}{\partial z}\left(T_p(z)\frac{\partial u(z,t)}{\partial z}\right) + \rho_f A_i\left(u_f^2\frac{\partial^2 u(z,t)}{\partial z^2} - 2u_f\frac{\partial^2 u(z,t)}{\partial z\partial t} + \frac{\partial^2 u(z,t)}{\partial t^2}\right) - \\ &\frac{\partial}{\partial z}\left[\left(A_e p_e(z) - A_i p_i(z)\right)\frac{\partial u(z,t)}{\partial z}\right] + \rho_p A_p\frac{\partial^2 u(z,t)}{\partial t^2} = F_x(z,t,\dot{u},\ddot{u},\ddot{v}) \quad . \end{aligned} \tag{3.1}$$

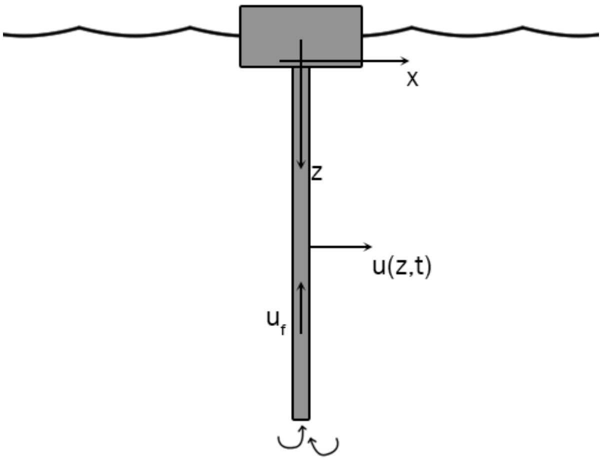

Figure 3.1: Cold water pipe for motions in horizontal direction

The first term of the equation $EI\frac{\partial^4 u(z,t)}{\partial z^4}$ is part of the standard Euler-Bernoulli beam theory and is the restoring force due to the bending stiffness of the pipe, where EI is the bending stiffness of the pipe material and $u(z,t)$ is the horizontal displacement of the system element in x-direction depending on the z-coordinate and time t.

The second term $\frac{\partial}{\partial z}\left(T_p(z)\frac{\partial u(z,t)}{\partial z}\right)$ is the restoring force due to the tension in the pipe, caused by gravity, buoyancy, the internal fluid flow and the ballast mass which is in thesis always assumed at the intake position (pipe end). When completely written out, this term equals:

$$\frac{\partial}{\partial z}\left(T_p(z)\frac{\partial u(z,t)}{\partial z}\right) = \frac{\partial}{\partial z}T_p(z)\frac{\partial u(z,t)}{\partial z} + T_p(z)\frac{\partial^2 u(z,t)}{\partial z^2} \quad , \tag{3.2}$$

where the tension $T_p(z)$ consists of the components:

$$T_p(z) = g m_{tot} - \rho_w g A_p L - \rho_f (L-z) A_i \frac{f_{DW}}{D_i}\frac{u_f^2}{2} \quad , \tag{3.3}$$

where g is the gravitational constant, the total weight of the pipe plus ballast mass is $m_{tot} = \rho_p A_p (L-z) + m_{bw}$, ρ_w is the mass density of the water, the cross-sectional area of pipe material is the difference between the external and internal cross-sectional areas, or $A_p = A_e - A_i$, L is the length of the pipe, ρ_f is the mass density of the fluid conveyed in the pipe, D_i is the internal diameter of the pipe, u_f is the velocity of the fluid conveyed in the pipe and f_{DW} is the Darcy-Weisbach resistance coefficient of the pipe material. This coefficient is dependent on the pipe material and can be found using the Colebrook-White equation. More on this can be found in the work of Acevedo et al. [6].

The third term $\rho_f A_i \left(u_f^2\frac{\partial^2 u(z,t)}{\partial z^2} - 2u_f\frac{\partial^2 u(z,t)}{\partial z \partial t} + \frac{\partial^2 u(z,t)}{\partial t^2}\right)$ is the restoring force due to the internal flow of the pipe as defined by for example Païdoussis and Li [30], consisting of a part caused by the centripetal acceleration $u_f^2\frac{\partial^2 u(z,t)}{\partial z^2}$, the Coriolis acceleration $2u_f\frac{\partial^2 u(z,t)}{\partial z \partial t}$ and the local acceleration $\frac{\partial^2 u(z,t)}{\partial t^2}$.

The fourth term $\frac{\partial}{\partial z}\left[\left(A_e p_e(z) - A_i p_i(z)\right)\frac{\partial u(z,t)}{\partial z}\right]$ is the restoring force due to the pressure difference between the inside and outside of the pipe. When completely written out, this term equals:

$$\frac{\partial}{\partial z}\left[\left(A_e p_e(z) - A_i p_i(z)\right)\frac{\partial u(z,t)}{\partial z}\right] = \frac{\partial}{\partial z}\left[A_e p_e(z) - A_i p_i(z)\right]\frac{\partial u(z,t)}{\partial z} + \left[A_e p_e(z) - A_i p_i(z)\right]\frac{\partial^2 u(z,t)}{\partial z^2} \quad , \tag{3.4}$$

where the external and internal pressure, p_e and p_i respectively, are given by:

$$
\begin{aligned}
p_e(z) &= \rho_w g z \quad , \\
p_i(z) &= \rho_f g z - 0.5\rho_f u_f^2 - \rho_f (L-z)\frac{f_{DW}}{D_i}\frac{u_f^2}{2} \quad .
\end{aligned} \tag{3.5}
$$

The fifth and final term of the left hand of the equation $\rho_p A_p \frac{\partial^2 u(z,t)}{\partial t^2}$ is the inertia force of the pipe and also part of the Euler-Bernoulli beam theory.

The right hand side of the equation $F_x(z,t,\dot{u},\ddot{u},\dot{v})$ is the dynamic reaction force in x-direction of the water surrounding the pipe, which is in general defined as:

$$
\begin{aligned}
F_x(z,t,\dot{u},\ddot{u},\dot{v}) &= \frac{1}{4}\pi D_e^2 \rho_w \ddot{u}_{water}(z,t) + \frac{1}{4}\pi D_e^2 \rho_w C_{a,p,x}\big(\ddot{u}_{water}(z,t) - \ddot{u}(z,t)\big) \\
+\frac{1}{2}\rho_w D_e C_{d,p,x} & \left(\big(\dot{u}_{water}(z,t) - \dot{u}(z,t)\big)\sqrt{\big(\dot{u}_{water}(z,t) - \dot{u}(z,t)\big)^2 + \big(\dot{v}_{water}(z,t) - \dot{v}(z,t)\big)^2}\right) \quad ,
\end{aligned} \tag{3.6}
$$

where overdots denote derivatives relative to time, D_e is the external pipe diameter, $C_{a,p,x}$ is the added mass coefficient of the pipe in x-direction, $u_{water}(z,t)$ is the displacement of the water surrounding the pipe in x-direction depending on the z-coordinate and time t (thus, two overdots denote acceleration), $C_{d,p,x}$ is the drag coefficient of the pipe in x-direction, $v_{water}(z,t)$ is the displacement of the water surrounding the pipe in y-direction depending on the z-coordinate and time t and $v(z,t)$ is the horizontal displacement of the system element in y-direction depending on the z-coordinate and time t. It has to be noted that this force will later be replaced by a different forcing term that includes vortex-induced vibrations and that this is just a general forcing term. Therefore the pipe will not be evaluated with this forcing term in this thesis, since it has been done before by for example Acevedo et al. [6].

3.3. Governing equations y-direction

Due to the shape of the cylinder, the force equilibrium in y-direction will be in the exact same form as the equations defined in Section 3.2. The equation of motion in this direction is thus given by:

$$
\begin{aligned}
EI\frac{\partial^4 v(z,t)}{\partial z^4} - \frac{\partial}{\partial z}\left(T_p(z)\frac{\partial u}{\partial z}\right) + \rho_f A_i\left(u_f^2\frac{\partial^2 v(z,t)}{\partial z^2} - 2u_f\frac{\partial^2 v(z,t)}{\partial z \partial t} + \frac{\partial^2 v(z,t)}{\partial t^2}\right) - \\
\frac{\partial}{\partial z}\left[\big(A_e p_e(z) - A_i p_i(z)\big)\frac{\partial v(z,t)}{\partial z}\right] + \rho_p A_p \frac{\partial^2 v(z,t)}{\partial t^2} = F_y(z,t,v(\dot{z},t),v(\ddot{z},t),\dot{u}) \quad ,
\end{aligned} \tag{3.7}
$$

where all the terms have been defined. The system only differs from the system explained in Section 3.2 in the right hand side of the equation where the dynamic reaction force in y-direction of the water surrounding the pipe is defined as:

$$
\begin{aligned}
F_y(z,t,\dot{v},\ddot{v},\dot{u}) &= \frac{1}{4}\pi D_e^2 \rho_w \ddot{v}_{water}(z,t) + \frac{1}{4}\pi D_e^2 \rho_w C_{a,p,y}\big(\ddot{v}_{water}(z,t) - \ddot{v}(z,t)\big) \\
+\frac{1}{2}\rho_w D_e C_{d,p,y} & \left(\big(\dot{v}_{water}(z,t) - \dot{v}(z,t)\big)\sqrt{\big(\dot{v}_{water}(z,t) - \dot{v}(z,t)\big)^2 + \big(\dot{u}_{water}(z,t) - \dot{u}(z,t)\big)^2}\right) \quad ,
\end{aligned} \tag{3.8}
$$

where $C_{a,p,y}$ is the added mass coefficient of the pipe in y-direction and $C_{d,p,y}$ is the drag coefficient of the pipe in y-direction.

3.4. Definitions of water velocity and acceleration

The velocity and acceleration of the water in x-direction and y-direction are determined based on the waves and currents present. The velocities are defined as:

$$
\begin{aligned}
\dot{u}_{water}(z,t) &= \cos(\theta_{cur})\, V_c(z,t) + \cos(\theta_{wave})\, V_w(z,t) \quad , \\
\dot{v}_{water}(z,t) &= \sin(\theta_{cur})\, V_c(z,t) + \sin(\theta_{wave})\, V_w(z,t) \quad ,
\end{aligned} \tag{3.9}
$$

and the accelerations are defined as:

$$
\begin{aligned}
\ddot{u}_{water}(z,t) &= \cos(\theta_{wave})\, a_w(z,t) \quad , \\
\ddot{v}_{water}(z,t) &= \sin(\theta_{wave})\, a_w(z,t) \quad ,
\end{aligned} \tag{3.10}
$$

where θ_{cur} is the angle of attack of the current, θ_{wave} is the angle of attack of the wave, $V_c(z,t)$ is the velocity of the current dependent on the z-coordinate and time t, $V_w(z,t)$ is the velocity of the wave dependent on the z-coordinate and time t and $a_w(z,t)$ is the acceleration of the wave dependent on the z-coordinate and time t. The equations correspond to the directions of the system given in Fig. 3.2.

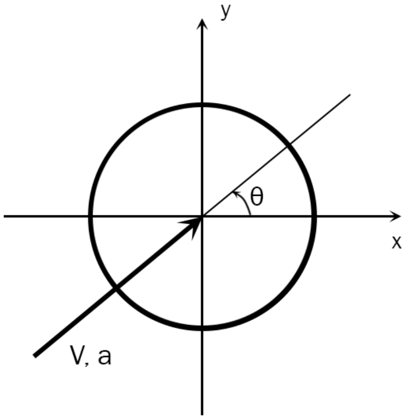

Figure 3.2: Angle of attack of velocity or acceleration, applicable for both current and waves

3.5. Wake oscillator model application

In general, recent researches and projects have been using the wake-oscillator model as defined in Section 2.2 since it's value has been proven. For this thesis, the system will be evaluated with the vortex-induced vibration forcing term. That means that in order to evaluate the system under influence of VIV, the right hand side of Eq. (3.1) and Eq. (3.7) can be replaced with a different expression for the hydrodynamic loading. In x-direction the hydrodynamic loading becomes:

$$F_x(z,t,\ddot{u}) = \frac{1}{2}\rho_w D_e V_c(z,t)^2 C_{VX}(z,t) - \frac{1}{4}\pi D_e^2 \rho_w C_{a,p,x}\ddot{u}(z,t) \quad , \tag{3.11}$$

and in y-direction the hydrodynamic loading becomes:

$$F_y(z,t,\ddot{v}) = \frac{1}{2}\rho_w D_e V_c(z,t)^2 C_{VY}(z,t) - \frac{1}{4}\pi D_e^2 \rho_w C_{a,p,y}\ddot{v}(z,t) \quad , \tag{3.12}$$

and finally for the wake the degree of freedom q is introduced, following the model of Ogink and Metrikine [22]:

$$\frac{\partial^2 q}{\partial t^2} + \varepsilon\omega_s(z,t)(q^2-1)\frac{\partial q}{\partial t} + \omega_s(z,t)^2 q = \frac{A}{D_e}\left(\frac{\partial^2 v}{\partial t^2}\cos(\theta_{cur}) - \frac{\partial^2 u}{\partial t^2}\sin(\theta_{cur})\right) \quad . \tag{3.13}$$

The fluid forces defined in Eq. (3.11) and Eq. (3.12) consist of a part caused by vortex shedding and a part caused by the added mass. The parameters used to calculate are all defined except for $C_{VX}(z,t)$ and $C_{VY}(z,t)$, which are the cross-flow vortex force coefficients in x-direction and y-direction respectively, dependent on the z-coordinate and time t. The equation of motion for degree of freedom q is defined using the dimensionless tuning parameters ε and A, the Strouhal frequency is $\omega_s(z,t) = 2\pi \,\mathrm{St}\, V_c(z,t)/D_e$ where $V_c(z,t)$ is the current velocity as defined in Section 3.4 and St is the Strouhal coefficient.

The coefficients $C_{VY}(z,t)$ and $C_{VX}(z,t)$ can be decomposed in a drag and lift part as done by Blevins [14] for galloping. Dependency on time t and z-coordinate will from here on out be omitted in notation for sake of readability. The coefficients can thence be obtained by:

$$\begin{aligned} C_{VX} &= \left(C_{VD}\cos\beta - C_{VL}\sin\beta\right)\frac{U^2}{V_c^2} \quad , \\ C_{VY} &= \left(C_{VD}\sin\beta + C_{VL}\cos\beta\right)\frac{U^2}{V_c^2} \quad , \end{aligned} \tag{3.14}$$

where U is the stream velocity relative to the motion of the pipe. The current flow V_c can be decomposed and is a resultant of a component in x-direction and a component in y-direction, or:

$$\begin{aligned} V_x &= \cos(\theta_{cur})\, V_c \quad , \\ V_y &= \sin(\theta_{cur})\, V_c \quad . \end{aligned} \tag{3.15}$$

Therefore, U_x is the current velocity minus the movement of the pipe in x-direction, and U_y is the current velocity minus the movement of the pipe in y-direction, of which U is the resultant relative velocity:

$$\begin{aligned} U_x &= V_x - \frac{\mathrm{d}u}{\mathrm{d}t} \quad , \\ U_y &= V_y - \frac{\mathrm{d}v}{\mathrm{d}t} \quad , \\ U &= \sqrt{U_x^2 + U_y^2} \quad . \end{aligned} \tag{3.16}$$

The angle of this relative velocity, β, is thence described as:

$$\begin{aligned} \cos\beta &= \frac{U_x}{U} \quad , \\ \sin\beta &= \frac{U_y}{U} \quad . \end{aligned} \tag{3.17}$$

For a better overview of this angle β, refer to Fig. 3.3. Finally, implementing all the obtained variables in Eq. (3.14), leads to the expressions for C_{VY} and C_{VX} where coefficients C_{VD} and C_{VL} are, following the lines of Ogink and Metrikine [22], given as:

$$\begin{aligned} C_{VD} &= \hat{C}_{x0}^{0} \quad , \\ C_{VL} &= \frac{\hat{C}_{y1}^{0}}{\hat{q}_1} q \quad , \end{aligned} \tag{3.18}$$

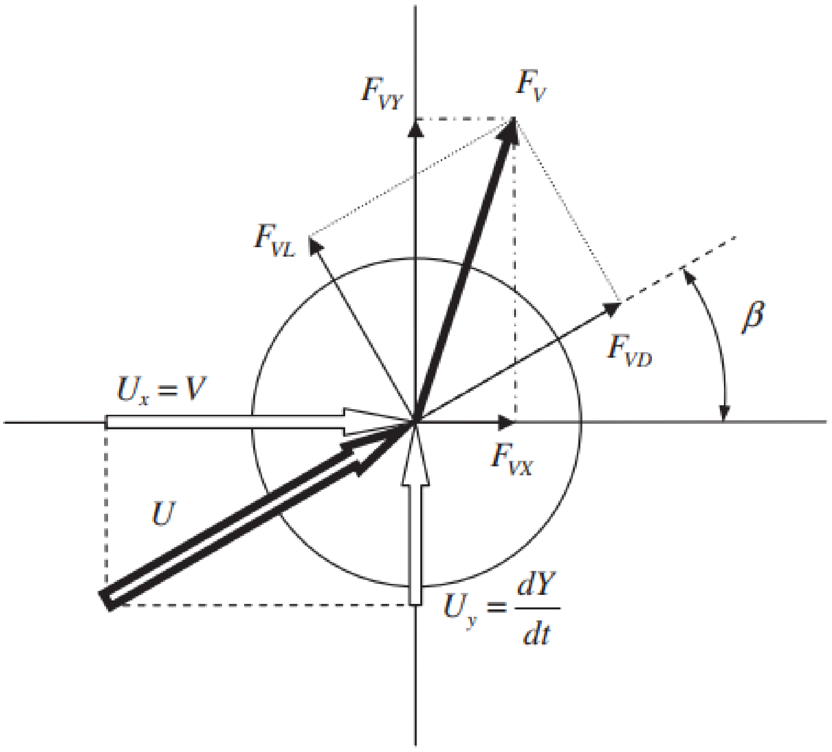

Figure 3.3: Overview of definition of variables and directions in the wake oscillator model by Ogink and Metrikine [22]

coupling the pipe motion to the wake oscillator. The undefined parameters and tuning parameters are given by the lower branch approximations of Ogink and Metrikine [22]:

$\hat{C}^0_{x0} = 1.1856$
$\hat{C}^0_{y1} = 0.3842$
$\mathrm{St} = 0.1932$
$A = 12.0$
$\varepsilon = 0.7$
$\hat{q}_1 = 2$

4

Software implementation pipe model

The model defined in Chapter 3 consists of multiple higher order partial differential equations. In theory, this system could be analytically solved for each time step. It is however preferred to implement the model in a software package that will solve the system numerically. This way the system will automatically be solved and it can be used with a large array of different parameters and variables. To make this large set of equations suitable for a software program, it has to be rewritten to a set of first order ordinary differential equations. To achieve this, the system will be discretised in one direction and this process will be discussed here. Then, the boundary conditions will be given and it will be explained how they are implemented in the model. An overview of the matrices of the system will be given and finally the possible outputs of the model are elaborated upon.

4.1. Finite differences and discretisation

To discretise a set of differential equations, one has to choose between the finite element method and the finite differences method. In general, the finite element method will yield a higher accuracy, but it will also be very demanding in terms of computational power. In this thesis axial extension is omitted and therefore the finite differences method is used, assuming sufficient accuracy. In order to turn this system of higher order partial differential equations into a system of second order ordinary differential equations, the system will be discretised in z-direction using Taylor's expansion, as explained by for example Rao [32]:

$$
\begin{aligned}
\frac{\partial u_{j,i}}{\partial z} &= \frac{1}{2\Delta z}\left(u_{j+1,i}-u_{j-1,i}\right) \quad ,\\
\frac{\partial^2 u_{j,i}}{\partial z^2} &= \frac{1}{(\Delta z)^2}\left(u_{j+1,i}-2u_{j,i}+u_{j-1,i}\right) \quad ,\\
\frac{\partial^3 u_{j,i}}{\partial z^3} &= \frac{1}{2(\Delta z)^3}\left(u_{j+2,i}-2u_{j+1,i}+2u_{j-1,i}-u_{j-2,i}\right) \quad ,\\
\frac{\partial^4 u_{j,i}}{\partial z^4} &= \frac{1}{(\Delta z)^4}\left(u_{j+2,i}-4u_{j+1,i}+6u_{j,i}-4u_{j-1,i}+u_{j-2,i}\right) \quad ,\\
\frac{\partial^2 u_{j,i}}{\partial z \partial t} &= \frac{1}{2\Delta z}\left(\frac{\partial}{\partial t}u_{j+1,i}-\frac{\partial}{\partial t}u_{j-1,i}\right) \quad ,
\end{aligned}
\tag{4.1}
$$

where u is the displacement in x-direction, j is the nth node ranging from $1,2,3...n$, i is the time step number and Δz is the length of the element, not to be confused with ∂z, the derivative of z.

For the sake of facilitating the discretisation process, the equation of motion from Eq. (3.1) can be rewritten as, following the lines of Acevedo et al. [6]:

$$
K_1^* \frac{\partial^4 u}{\partial z^4} + K_2^*(z)\frac{\partial^2 u}{\partial z^2} + C_1^* \frac{\partial^2 u}{\partial z \partial t} + K_3^*(z)\frac{\partial u}{\partial z} + M_1 \frac{\partial^2 u}{\partial t^2} = F_x(z,t,\dot{u},\ddot{u},\dot{v}) \quad , \tag{4.2}
$$

where

$$\begin{aligned}
K_1^* &= EI \quad , \\
K_2^*(z) &= -T_p(z) + \rho_f A_i u_f^2 - \left(A_e p_e(z) - A_i p_i(z)\right) \quad , \\
C_1^* &= -2\rho_f A_i u_f \quad , \\
K_3^*(z) &= -T_p(z)\frac{\partial}{\partial z} - \left(A_e p_e(z)\frac{\partial}{\partial z} - A_i p_i(z)\frac{\partial}{\partial z}\right) \quad , \\
M_1 &= \rho_f A_i + \rho_p A_p \quad .
\end{aligned} \tag{4.3}$$

Note that $\frac{\partial T_p(z)}{\partial z}$, $\frac{\partial p_e(z)}{\partial z}$ and $\frac{\partial p_i(z)}{\partial z}$ have to be discretised as well, leading to:

$$\begin{aligned}
\frac{\partial T_{p,j}(z)}{\partial z} &= \frac{1}{2\Delta z}\left(T_{p,j+1} - T_{p,j-1}\right) \quad , \\
\frac{\partial p_{e,j}(z)}{\partial z} &= \frac{1}{2\Delta z}\left(p_{e,j+1} - p_{e,j-1}\right) \quad , \\
\frac{\partial p_{i,j}(z)}{\partial z} &= \frac{1}{2\Delta z}\left(p_{i,j+1} - p_{i,j-1}\right) \quad .
\end{aligned} \tag{4.4}$$

Implementing the system of Eq. (4.1) into Eq. (4.2) will yield the discretised equation of motion:

$$\begin{aligned}
&M_1 \ddot{u}_{j,i} + K_1\left(u_{j+2,i} - 4u_{j+1,i} + 6u_{j,i} - 4u_{j-1,i} + u_{j-2,i}\right) + K_2(z)\left(u_{j+1,i} - 2u_{j,i} + u_{j-1,i}\right) \\
&+ C_1\left(\dot{u}_{j+1,i} - \dot{u}_{j-1,i}\right) + K_3(z)\left(u_{j+1,i} - u_{j-1,i}\right) = F_{x,j,i} \quad ,
\end{aligned} \tag{4.5}$$

where

$$\begin{aligned}
K_1 &= \frac{K_1^*}{(\Delta z)^4} \quad , \\
K_2(z) &= \frac{K_2^*}{(\Delta z)^2} \quad , \\
C_1 &= \frac{C_1^*}{2\Delta z} \quad , \\
K_3(z) &= \frac{K_3^*}{2\Delta z} \quad ,
\end{aligned} \tag{4.6}$$

and $F_{x,j,i}$ is defined as the force which can be defined as the inertia and drag force defined in Section 3.2, or as the vortex-induced vibration force defined in Section 3.5. Due to the symmetry of the system, the equation of motion in y-direction can be rewritten following the same lines, as:

$$\begin{aligned}
&M_1 \ddot{v}_{j,i} + K_1\left(v_{j+2,i} - 4v_{j+1,i} + 6v_{j,i} - 4v_{j-1,i} + v_{j-2,i}\right) + K_2(z)\left(v_{j+1,i} - 2v_{j,i} + v_{j-1,i}\right) \\
&+ C_1\left(\dot{v}_{j+1,i} - \dot{v}_{j-1,i}\right) + K_3(z)\left(v_{j+1,i} - v_{j-1,i}\right) = F_{y,j,i} \quad .
\end{aligned} \tag{4.7}$$

4.2. Discretisation of boundary conditions

Depending on the boundary conditions, the system takes a different form at the ends of the pipe. In order to implement this, the boundary conditions have to be defined and discretised. Since the nodes $j = -1$, $j = 0$, $j = n+1$ and $j = n+2$ are fictitious, some boundary conditions will have to be rewritten. The pipe will be modelled as fixed-fixed at the top and free hanging with a ballast mass attached to it at the end. This leads to the following boundary conditions, for each time step.

Top (fixed-fixed)

At the top, the displacement is zero and the rotation is zero:

$$\begin{aligned}
u_j &= 0 \quad , \\
\frac{\partial u_j}{\partial z} &= 0 \quad ,
\end{aligned} \tag{4.8}$$

or in discretised form:

$$\begin{aligned} u_j &= 0 \quad , \\ \frac{u_{j+1}-u_{j-1}}{2\Delta z} &= 0 \Rightarrow u_{j-1} = u_{j+1} \quad . \end{aligned} \tag{4.9}$$

Applying this for the fictitious node $j = 0$ yields:

$$\begin{aligned} u_0 &= 0 \quad , \\ u_{-1} &= u_1 \quad . \end{aligned} \tag{4.10}$$

Therefore at the top two nodes ($j = 1$ and $j = 2$) the system will take the following form (z-dependency of terms defined in Eq. (4.6) has been omitted for the sake of readability). For $j = 1$:

$$M_1 \ddot{u}_1 + K_1 (7u_1 - 4u_2 + u_3) + K_2 (-2u_1 + u_2) + C_1 (\dot{u}_2) + K_3 (u_2) = F_{x,1} \quad . \tag{4.11}$$

For $j = 2$:

$$M_1 \ddot{u}_2 + K_1 (-4u_1 + 6u_2 - 4u_3 + u_4) + K_2 (u_1 - 2u_2 + u_3) + C_1 (\dot{u}_3 - \dot{u}_1) + K_3 (u_3 - u_1) = F_{x,2} \quad . \tag{4.12}$$

Bottom (free-hanging end with attached ballast mass)

The bottom is not fixed, which means that the moment at the end is zero. However, as opposed to a normal free-hanging end, the shear force is not zero but caused by a dynamic inertia force on the mass due to the movement of the pipe end [6]:

$$\begin{aligned} \frac{\partial^2 u_j}{\partial z^2} &= 0 \quad , \\ \frac{\partial^3 u_j}{\partial z^3} &= \frac{m_{bw}}{EI} \frac{\partial^2 u_j}{\partial t^2} \quad , \end{aligned} \tag{4.13}$$

or in discretised form:

$$\begin{aligned} \frac{u_{j+1} - 2u_j + u_{j-1}}{(\Delta z)^2} &= 0 \Rightarrow u_{j+1} = 2u_j - u_{j-1} \quad , \\ \frac{u_{j+2} - 2u_{j+1} + 2u_{j-1} - u_{j-2}}{2(\Delta z)^3} &= \frac{m_{bw}}{EI} \frac{\partial^2 u_j}{\partial t^2} \\ \Rightarrow u_{j+2} &= \frac{m_{bw} \cdot 2(\Delta z)^3}{EI} \frac{\partial^2 u_j}{\partial t^2} + u_{j-2} - 2u_{j-1} + 2u_{j+1} \\ &= \frac{m_{bw} \cdot 2(\Delta z)^3}{EI} \frac{\partial^2 u_j}{\partial t^2} + u_{j-2} - 4u_{j-1} + 4u_j \quad . \end{aligned} \tag{4.14}$$

Applying this for the end node $j = n$ yields:

$$\begin{aligned} u_{n+1} &= 2u_n - u_{n-1} \quad , \\ u_{n+2} &= \frac{m_{bw} \cdot 2(\Delta z)^3}{EI} \frac{\partial^2 u_n}{\partial t^2} + u_{n-2} - 2u_{n-1} + 2u_{n+1} \\ &= \frac{m_{bw} \cdot 2(\Delta z)^3}{EI} \frac{\partial^2 u_n}{\partial t^2} + u_{n-2} - 4u_{n-1} + 4u_n \quad . \end{aligned} \tag{4.15}$$

Note that in the case that $m_{bw} = 0$, the equations change to the exact equations for a free hanging end. This means that this system can also be used to model a free end by setting the ballast mass at zero. Therefore at the bottom two nodes ($j = n-1$ and $j = n$) the system will take the following form. For $j = n-1$:

$$\begin{aligned} &M_1 \ddot{u}_{n-1} + K_1 \left(u_{n-3} - 4u_{n-2} + 5u_{n-1} - 2u_n + \frac{m_{bw} \cdot 2(\Delta z)^3}{EI} \ddot{u}_{n-1} \right) \\ &+ K_2 (u_{n-2} - 2u_{n-1} + u_n) + C_1 (\dot{u}_{n-2} - \dot{u}_n) + K_3 (u_{n-2} - u_n) = F_{x,n-1} \quad . \end{aligned} \tag{4.16}$$

For $j = n$:

$$M_1\ddot{u}_n + K_1\left(u_{n-2} - 4u_{n-1} + 2u_n + \frac{m_{bw}\cdot 2(\Delta z)^3}{EI}\ddot{u}_n\right) + C_1\left(2\dot{u}_n - 2\dot{u}_{n-1}\right) + K_3\left(2u_n - 2u_{n-1}\right) = F_{x,n} \quad . \tag{4.17}$$

Once again, due to the symmetrical nature of the system, everything stated above applies for the v-direction as well and shall therefore not be further defined for this direction.

4.3. Matrix notation

The equations of motion can now be written in matrix-form and solved for each time step:

$$\begin{aligned} \mathbf{M}\underline{\ddot{u}} + \mathbf{C}\underline{\dot{u}} + \mathbf{K}\underline{u} &= \underline{F} \quad , \\ \mathbf{M}\underline{\ddot{v}} + \mathbf{C}\underline{\dot{v}} + \mathbf{K}\underline{v} &= \underline{F} \quad , \end{aligned} \tag{4.18}$$

where

$$\underline{u} = \begin{bmatrix} u_1 \\ u_2 \\ \vdots \\ u_n \end{bmatrix} \quad , \underline{v} = \begin{bmatrix} v_1 \\ v_2 \\ \vdots \\ v_n \end{bmatrix} \quad , \tag{4.19}$$

and the mass, damping and stiffness can be divided in three parts. The top nodes (with top boundary conditions), any intermediate node, and the bottom nodes (with bottom boundary conditions).

Top nodes

The entries for the mass, damping and stiffness matrix for the top nodes can be defined as follows:

$$\mathbf{M}^{top} = \begin{bmatrix} m_p + m_f & 0 & 0 & \cdots \\ 0 & m_p + m_f & 0 & \cdots \\ 0 & 0 & m_p + m_f & \cdots \\ \vdots & \vdots & \vdots & \ddots \end{bmatrix} \quad , \tag{4.20}$$

$$\mathbf{C}^{top} = \begin{bmatrix} 0 & C_1 & 0 & 0 & 0 & \cdots \\ -C_1 & 0 & C_1 & 0 & 0 & \cdots \\ 0 & -C_1 & 0 & C_1 & 0 & \cdots \\ \vdots & \vdots & \vdots & \vdots & \vdots & \ddots \end{bmatrix} \quad , \tag{4.21}$$

$$\mathbf{K}^{top} = \begin{bmatrix} 7K_1 - 2K_2 & -4K_1 + K_2 + K_3 & K_1 & 0 & 0 & \cdots \\ -4K_1 + K_2 - K_3 & 6K_1 - 2K_2 & -4K_1 + K_2 + K_3 & K_1 & 0 & \cdots \\ K_1 & -4K_1 + K_2 + K_3 & 6K_1 - 2K_2 & -4K_1 + K_2 + K_3 & K1 & \cdots \\ \vdots & \vdots & \vdots & \vdots & \vdots & \ddots \end{bmatrix} \quad . \tag{4.22}$$

Intermediate nodes

The entries for the mass, damping and stiffness matrix for the intermediate nodes can be defined as follows:

$$\mathbf{M}^{int} = \begin{bmatrix} \ddots & \vdots & \vdots & \\ \cdots & m_p + m_f & 0 & \cdots \\ \cdots & 0 & m_p + m_f & \cdots \\ & \vdots & \vdots & \ddots \end{bmatrix} \quad , \tag{4.23}$$

$$\mathbf{C}^{int} = \begin{bmatrix} \ddots & \vdots & \vdots & \vdots & \vdots & \vdots & \vdots & \\ \cdots & 0 & -C_1 & 0 & C_1 & 0 & 0 & \cdots \\ \cdots & 0 & 0 & -C_1 & 0 & C_1 & 0 & \cdots \\ & \vdots & \vdots & \vdots & \vdots & \vdots & \vdots & \ddots \end{bmatrix} \quad , \tag{4.24}$$

$$\mathbf{K}^{int} = \begin{bmatrix} \ddots & \vdots & \vdots & \vdots & \vdots & \vdots & \vdots & \\ \cdots & K_1 & -4K_1+K_2+K_3 & 6K_1-2K_2 & -4K_1+K_2+K_3 & K1 & 0 & \cdots \\ \cdots & 0 & K_1 & -4K_1+K_2+K_3 & 6K_1-2K_2 & -4K_1+K_2+K_3 & K1 & \cdots \\ & \vdots & \vdots & \vdots & \vdots & \vdots & \vdots & \ddots \end{bmatrix} \quad . \tag{4.25}$$

Bottom nodes

The entries for the mass, damping and stiffness matrix for the bottom nodes can be defined as follows:

$$\mathbf{M}^{bot} = \begin{bmatrix} \ddots & \vdots & \vdots & \vdots \\ \cdots & m_p + m_f & 0 & 0 \\ \cdots & 0 & m_p + m_f + \frac{2m_{bw}}{(\Delta z)^2} & 0 \\ \cdots & 0 & 0 & m_p + m_f + \frac{2m_{bw}}{(\Delta z)^2} \end{bmatrix} \quad , \tag{4.26}$$

$$\mathbf{C}^{bot} = \begin{bmatrix} \ddots & \vdots & \vdots & \vdots & \vdots & \vdots \\ \cdots & 0 & -C_1 & 0 & C_1 & 0 \\ \cdots & 0 & 0 & -C_1 & 0 & C_1 \\ \cdots & 0 & 0 & 0 & -2C_1 & 2C_1 \end{bmatrix} \quad , \tag{4.27}$$

$$\mathbf{K}^{bot} = \begin{bmatrix} \ddots & \vdots & \vdots & \vdots & \vdots & \vdots \\ \cdots & K_1 & -4K_1+K_2+K_3 & 6K_1-2K_2 & -4K_1+K_2+K_3 & K_1 \\ \cdots & 0 & K_1 & -4K_1+K_2-K_3 & 5K_1-2K_2 & -2K_1+K_2+K_3 \\ \cdots & 0 & 0 & 2K_1 & -4K_1-2K_3 & 2K_1+2K_3 \end{bmatrix} \quad . \tag{4.28}$$

4.4. Model outputs

The eventual goal of this model is to evaluate the occurrence of VIV in the cold water pipe and determining the impact of several different parameters on the vibrations. Therefore, the model needs to produce multiple relevant outputs that can be used for discussing and analysing the behaviour of the pipe. The outputs that this model will provide are listed in this section.

Natural frequencies

The system of equations in matrix-form defined in Section 4.3 can easily be used to find the undamped natural frequencies, by solving the following system:

$$\left| -\omega^2 \mathbf{M} + \mathbf{K} \right| = 0 \quad . \tag{4.29}$$

The natural frequency can be used to determine the expected pipe behaviour, gives information about resonance possibilities and is in general a useful tool to analyse mode shapes. In this model the natural frequency will mainly be used to check if VIV occurs and if so in what mode.

Pipe displacement

The most valuable outputs of this model are the displacement of the pipe in x-direction (or displacement u) and y-direction (or displacement v). All the other valuable outputs, for example forces, stresses and fatigue checks, are dependent on the displacements. The displacements of the pipe at every node are obtained by using software to solve the entire system of equations defined in Section 4.3 with an ordinary differential equations integrator (in this case *odeint* from Python's *scipy.integrate*-package). More on this can be found in Appendix A. With the displacements at every node and the length of the elements known, the shape of the pipe at every time step can be determined.

Forces and moments

With the displacements at all nodes known, other relevant outputs as forces and moments can be calculated. The moment in a beam is related to the second derivative (curvature) with respect to the length of the beam as follows:

$$\begin{aligned} M_x &= EI\frac{\partial^2 u}{\partial z^2} \quad , \\ M_y &= EI\frac{\partial^2 v}{\partial z^2} \quad , \end{aligned} \tag{4.30}$$

where from Eq. (4.1) can be recalled that:

$$\begin{aligned} \frac{\partial^2 u_j}{\partial z^2} &= \frac{1}{(\Delta z)^2}\left(u_{j+1} - 2u_j + u_{j-1}\right) \quad , \\ \frac{\partial^2 v_j}{\partial z^2} &= \frac{1}{(\Delta z)^2}\left(v_{j+1} - 2v_j + v_{j-1}\right) \quad . \end{aligned} \tag{4.31}$$

The shear force in a beam is related to the third derivative with respect to the length of the beam:

$$\begin{aligned} F_{shear,x} &= EI\frac{\partial^3 u}{\partial z^3} \quad , \\ F_{shear,y} &= EI\frac{\partial^3 v}{\partial z^3} \quad , \end{aligned} \tag{4.32}$$

where from Eq. (4.1) can be recalled that:

$$\begin{aligned} \frac{\partial^3 u_j}{\partial z^3} &= \frac{1}{2(\Delta z)^3}\left(u_{j+2} - 2u_{j+1} + 2u_{j-1} - u_{j-2}\right) \quad , \\ \frac{\partial^3 v_j}{\partial z^3} &= \frac{1}{2(\Delta z)^3}\left(v_{j+2} - 2v_{j+1} + 2v_{j-1} - v_{j-2}\right) \quad . \end{aligned} \tag{4.33}$$

Finally, the normal force in the pipe has been defined before as the tension in the pipe and can be recalled from Section 3.2 as:

$$T_p(z) = gm_{tot} - \rho_w g A_p L - \rho_f (L-z) A_i \frac{f_{DW}}{D_i}\frac{u_f^2}{2} \quad . \tag{4.34}$$

Stresses

The forces from the previous subsection can be used to determine the stresses in the pipe. The normal stress in longitudinal direction of the pipe is given as [33]:

$$\sigma_{z,tot}(x,y) = \frac{T_p}{A_p} + \frac{xM_x}{I} + \frac{yM_y}{I} \quad , \tag{4.35}$$

where M_x and M_y are the bending moments about the x- and y-axis respectively, x is the position in the x-direction and y is the position in the y-direction and I is the moment of inertia, which in this symmetrical case is the same in x- and y-direction, defined for a hollow cylindrical cross-section as:

$$I = \frac{\pi}{64}\left(D_e^4 - D_i^4\right) \quad . \tag{4.36}$$

Since for the fatigue analysis of the pipe the maximum stress is of most importance, the stress will usually be considered at the extremes, which means either in cross-flow or in-line direction. This means that for the in-line fatigue $x = D_e/2$ and $y = 0$, and for the cross-flow fatigue $x = 0$ and $y = D_e/2$, so the bending stresses that are to be considered become:

$$\begin{aligned} \sigma_{z,IL} &= \frac{M_x D_e}{2I} \quad , \\ \sigma_{z,CF} &= \frac{M_y D_e}{2I} \quad , \end{aligned} \tag{4.37}$$

where $\sigma_{z,IL}$ is the bending stress to be considered when analysing in-line VIV and $\sigma_{z,CF}$ is the bending stress to be considered when analysing cross-flow VIV. The maximum longitudinal stress at a point in the pipe is a combination of the resultant bending stress in x- and y-direction and the normal stress. For extra safety considerations, the maximum normal stress scenario considered in this thesis will be a sum of the normal stress due to axial tension, the in-line bending stress at $x = D_e/2$ and the cross-flow bending stress at $y = D_e/2$. Note that in general the resultant the in-line and cross-flow stress is considered. The maximum normal stress scenario is therefore defined as:

$$\sigma_{z,tot}(x,y) = \frac{T_p}{A_p} + \frac{M_x D_e}{2I} + \frac{M_y D_e}{2I} \quad . \tag{4.38}$$

Finally, the shear force can be used to calculate the shear stress of the pipe. The shear stress for a pipe with relatively thick walls can be defined as [34]:

$$\begin{aligned} \tau_{x,max} &= \left(2 + \frac{t}{r}\right)\frac{F_{shear,x}}{A_p} \quad , \\ \tau_{y,max} &= \left(2 + \frac{t}{r}\right)\frac{F_{shear,y}}{A_p} \quad , \end{aligned} \tag{4.39}$$

where $\tau_{x,max}$ and $\tau_{y,max}$ are the maximum shear stress in x- and y-direction respectively, $F_{shear,x}$ and $F_{shear,y}$ are the shear force in x- and y-direction respectively as defined in Eq. (4.32), t is the wall thickness and r is the radius of the pipe, in this case $r = D_e/2$.

Fatigue

The final important output from this model is a fatigue analysis of the vibrations in the pipe, since analysing the fatigue caused by VIV after a certain period of time is one of the main goals of this model. In order to do this, the stress cycle defined in Eq. (4.38) is considered. This stress cycle will most probably have a sort of oscillatory shape due to the nature of the pipe vibrations. From this stress cycle the fatigue damage D is determined with the Miner-Palmgren summation [33]:

$$D = \sum_{i=1}^{N_{bin}} \frac{n_i}{N_i} \quad , \tag{4.40}$$

where N_i is the number of cycles to failure and n_i is the number of stress cycles at a certain stress range $\Delta\sigma_i$, and N_{bin} is the number of different stress ranges that occur in the complete stress cycle. The values for $\Delta\sigma_i$ and N_{bin} follow from the stress cycle defined in Eq. (4.38). As mentioned before, this cycle will have a certain oscillatory motion and therefore the magnitude and the amount of cycles at a certain stress range can be determined by the rainflow-counting method. A Python package called *rainflow* is used, which automatises the rainflow-counting process according to the rules of ASTM E1049-85 [35]. N_i can be determined from a standard SN-curve. However, the form of this SN-curve differs for every material, since for every different material a separate fatigue model has been developed. For example for steel, from N-004 [36] N_i can be obtained from:

$$\log N_i = \log a - m \log \Delta\sigma_i \quad , \tag{4.41}$$

where a and m are both material specific and are the scale parameter and the slope parameter respectively. For an FRP pipe, a hybrid model can be obtained from Hwang and Han [37] as:

$$N_i = [B(1-r)]^{1/c} \quad , \tag{4.42}$$

where r is the stress-ratio of applied stress range compared to the maximum stress or $\Delta\sigma_i/\sigma_y$, and B and c are material dependent parameters. For a HDPE pipe, the damage per cycle can be obtained from Basquin's equation as per Bourchak and Aid [38]:

$$\log \Delta\sigma_i = b \log N_i + \log A \quad , \tag{4.43}$$

where A and b are material dependent parameters. Using these SN-curves for the different materials, for each stress range the amount of cycles until failure can be determined. Therefore, if the amount of cycles at a certain stress range is known, the damages can be summed up per Miner's rule, and the total damage of a certain period of stress cycle can be determined.

4.5. Analysis of variables

The main interest and purpose of this report lies in analysing the influence of different variables on the response of the system. Different parameters lead to differences in vibration amplitudes, periods and mode shapes. Therefore, several variables that are of interest are identified and listed. It is argued why and how all of these variables will change the response of the system. The different possibilities of the variables considered are discussed as well, but quantitative verdicts will be kept for a later stadium.

Materials

One of the most fundamental variables that can change in a pipe structure is its material. The material in which a pipe is made is highly influential on several aspects like its cost, the production process, its applicability in different environments and its installation process. Other than that, and of more importance for this report, it changes the behaviour of the pipe subjected to flows and forces. A different material means a different density, which changes the mass or inertia of the pipe and the tension in the pipe. It also changes the stiffness, which might lead to lower amplitudes or faster vibration frequencies. The materials that will be evaluated in this research are [6] (i) steel, the most obvious and omnipresent material for a long pipe or riser due to its strength and availability ($\rho = 7800$ kg/m^3, $E = 211$ GPa, $\sigma_y = 240$ MPa) (ii) composite pipe, either fibre reinforced plastic (FRP) or epoxy material, light and strong material with high fatigue resistance ($\rho = 1800$ kg/m^3, $E = 26$ GPa, $\sigma_y = 125$ MPa) (iii) high density poly-ethylene (HDPE), an easily manufacturable and deployable material, readily available in large diameters. ($\rho = 950$ kg/m^3, $E = 0.7$ GPa, $\sigma_y = 25$ MPa)

Diameter and wall thickness

The diameter and wall thickness are, as is the material, often a debatable item when pipes are constructed and depend of the purpose of the pipe. Pipes that have to convey a lot of fluid usually have a bigger diameter than pipes that are just used for small transportations. Although the pipe diameter will mostly have influence on the drag force on the pipe (a large diameter means a large surface and thus a high drag force), it changes certain aspects of the pipe as the stiffness too and will therefore influence the VIV response. The same goes for the wall thickness, which is usually related to the diameter. Since an OTEC plant needs an enormous cold water intake, the pipes deployed for this purpose will be of unusual high diameters, and will therefore experience a high amount of drag. The pipe will be evaluated with (i) a diameter ranging between 2.0 and 6.0 m, with various diameters in between (ii) a diameter to wall thickness ratio ranging between $D_e/t = 12$ and $D_e/t = 26$, covering the full range of standards for HDPE. It has to be noted here that not all the evaluated scenarios will be available or realistic, but since this is merely a theoretical exploration of the possibilities, they will be evaluated regardless.

Ballast mass

From earlier studies as performed by Acevedo et al. [6] it can be concluded that a ballast mass to tension the pipe is unavoidable for the lighter and more flexible materials as HDPE or FRP, since otherwise the pipe would reach unreasonably high deflections due to the drag, or simply buckle because of its buoyancy. It is however interesting to evaluate the influence the presence of the ballast mass (and its magnitude) on the VIV. The scenarios that will be looked at will depend on the material, but will include (i) no ballast mass present (ii) ballast mass of magnitude defined by Acevedo et al. [6] (iii) empirically determined ballast mass ranging from a low ballast that just ensures stability of the model mass to roughly double the above defined ballast mass.

Inflow velocity

Another variable that might impact the response of the system is the velocity of the inflow of cold water in the pipe. The velocity of the inflow will change the tension and pressure in the pipe and will change the response of the system. The scenarios that will be evaluated are (i) a pipe without inflow (ii) an inflow velocity between 1.0 and 6.0 m/s in several steps.

Current velocity

The current velocity that the pipe is subjected to, is the factor that determines the magnitude of the forces. A high flow velocity means a high drag force, but the VIV response depends on the current velocity as well. As is known, VIV will mainly occur at flow velocities where the vortex shedding frequency ($f_s = \mathrm{St}\, V_c/D_e$) is close to a natural frequency of the system, since lock-in will occur. Because in the range of Reynolds numbers where vortex shedding will occur the Strouhal number is always around 0.2 (as can be found in Fig. 2.5) the natural frequency can be used to determine a flow velocity where VIV will almost certainly appear, which is useful to check the system for VIV-related movements. This might not always be a realistic current velocity and therefore a more realistic scenario has to be evaluated too, since the system will respond to those current velocities and might show VIV-like movements. The flow scenarios that will be evaluated are (i) hand-picked constant current velocities that will correspond with the system's natural modes to check the VIV response (ii) a range of low to high current velocities to evaluate a large range of possible pipe responses (iii) a realistic current flow scenario with a sheared profile as determined in earlier studies [6] to determine if the occurrence of VIV is a realistic possibility. A visualisation of the different current profiles can be found in Fig. 4.1

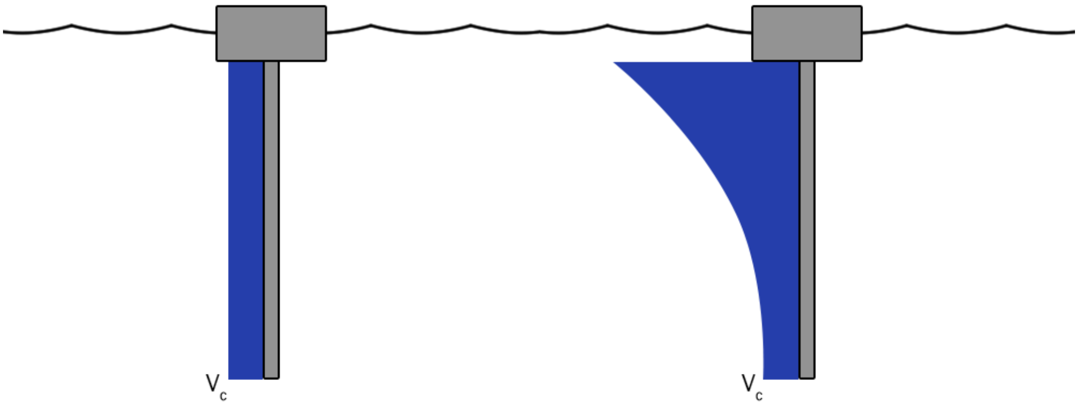

Figure 4.1: The possible current profiles that are evaluated in this thesis: uniform (left) and sheared (right)

5

Cold water pipe analysis

This chapter is dedicated to the analysis of the occurrence of VIV in the cold water pipe, using the software model defined in Chapter 4. To start off, the model is run with a typical size steel riser to establish a benchmark, and a typical size HDPE cold water pipe. Then, the different variables listed in Section 4.5 are systematically evaluated. A short summary of the results is provided, and a conclusion is drawn. For the full set of results, one might refer to Appendix B.

5.1. Typical riser model test

Since the cold water pipe of an OTEC plant is of an unusual size, the model used to analyse this pipe might yield unusual results. In order to create some sort of benchmark with which the model results of the cold water pipe can be compared, the model will first be used for the analysis of a typical sized steel riser. Since the subject of VIV in marine steel risers has been researched innumerable times before (for example experimentally by Trim et al. [39] or numerically by Wanderley and Levi [40]), the results of this benchmark can be used as an intuitive validation of the model. For more on model validation, refer to Appendix C.

The riser that will be evaluated will be of a diameter of 0.25 m (approximately 10 inch) with a wall thickness of 0.015 m and of 1000 m length. The riser will be subdued to a current velocity of 0.2 m uniform over its depth, in order to check its response in a single mode. Since the riser will be expected to shed at a high mode, the pipe will be discretised in 80 elements, where bigger pipes which will be expected to shed at lower modes will be discretised in less elements. It can be assumed that the model run is long enough for the pipe to establish an equilibrium and all the VIV characteristics will be captured. The model parameters can be found in Tab. 5.1.

Table 5.1: Pipe parameters and model parameters for typical riser

Pipe parameters			
Material		Steel	
Length	L	1000	m
Outer diameter	D_e	0.25	m
Wall thickness	t	0.015	m
Pipe material density	ρ_p	7800	kg/m^3
Young's modulus	E	$211 \cdot 10^9$	N/m^2
Gravitational constant	g	9.81	m/s^2
Ballast mass	m_{bw}	0	kg
Seawater and fluid parameters			
Sea water density	ρ_w	1026.6	kg/m^3
Fluid intake density	ρ_f	1027.6	kg/m^3
Fluid intake velocity	U_f	2.3	m/s

Model parameters			
Added mass coefficient	C_a	1	-
Element length	Δz	12.5	m
Drag coefficient	$C_{x0}^{\hat{0}}$	1.1856	-
Lift coefficient	$C_{y1}^{\hat{0}}$	0.3842	-
Strouhal number	St	0.1932	-
Tuning parameter	ε	0.7	-
Tuning parameter	A	12	-
Wake oscillator amplitude	q_1	2	-
Current parameters			
Type		Uniform	
Magnitude	V_c	0.2	m/s

The natural frequencies of this pipe as calculated by Eq. (4.29) can be found in Appendix B.1. Since it is expected that VIV will occur at natural frequencies that are close to the natural frequency, it can be predicted at which velocity the pipe will vibrate in a certain mode from Eq. (2.2). These velocities are listed along with their corresponding natural frequencies. From Tab. B.1 it can be found that the shedding will most likely occur in one of the modes summarised in Tab. 5.2.

Table 5.2: Natural frequencies and corresponding current velocities

Mode number	**Nat. freq. in rad/s**	**Nat. freq. in Hz**	**Current velocity in m/s**
8	0.885	0.141	0.182
9	1.013	0.161	0.209
10	1.142	0.182	0.235

Fig. 5.1 shows snapshots of several states of the cross-flow displacement in the pipe, as well as the displacement in the u,v-plane at the point of maximum displacement which in this case is the free-hanging riser end. It can immediately be observed that the riser sheds at a high mode. Furthermore, it can be seen that the cross-flow vibration amplitude is in the order of $1D_e$.

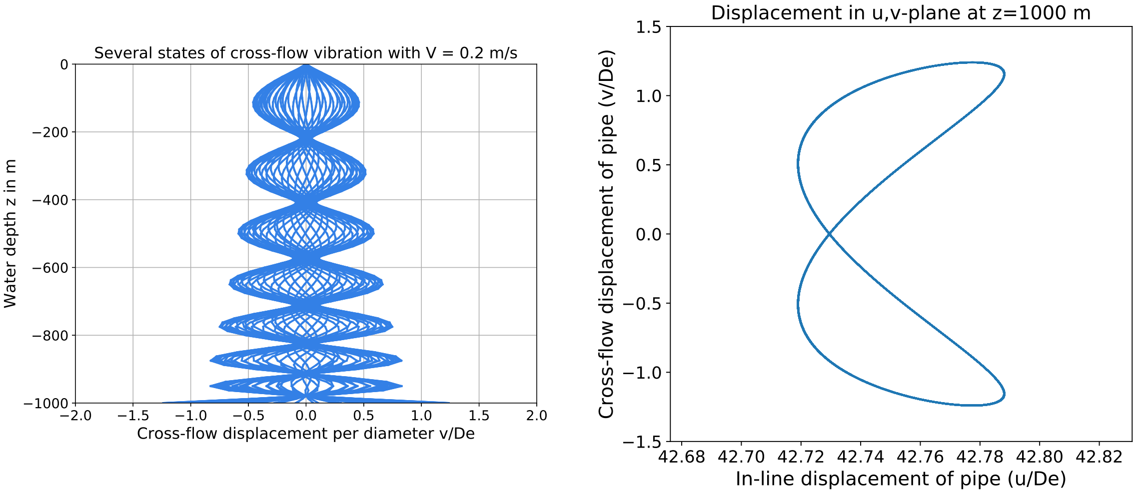

Figure 5.1: Several snapshots of the state of the cross-flow vibration of the pipe divided by the diameter(left) and the displacement in the u,v-plane at the point of maximum displacement (right)

Fig. 5.2 shows the frequency density spectrum of the pipe subjected to a uniform 0.2 m/s current. The natural frequencies are depicted as red dots. It can be seen that the system vibrates close to the eighth mode, which accords to the image of Fig. 5.1.

A summary of all the calculated outputs was given in Appendix B. The results of the model run are summed up in Tab. 5.3. For the properties and strengths of the materials that are used, consult the work of Acevedo et al. [6]. The maximum allowable shear stress k is defined by the Von Mises-criterium:

$$k = \frac{\sigma_y}{\sqrt{3}} \quad , \tag{5.1}$$

where σ_y is the maximum yield stress of a material.

Conclusion

The main purpose of this section was to test the model on a steel pipe with the properties of a typical riser. As can be seen from all the figures and outputs, the model behaves as can be expected from the simulation of VIV on a marine steel riser. The displacement amplitudes are in the order of $1.0D_e$ and the fatigue damage is in the same order as experiments by for example Trim et al. [39]. From this, it can therefore be concluded that the model works as expected and that it can be used to evaluate other scenarios, as the different setups for a cold water pipe of an OTEC plant.

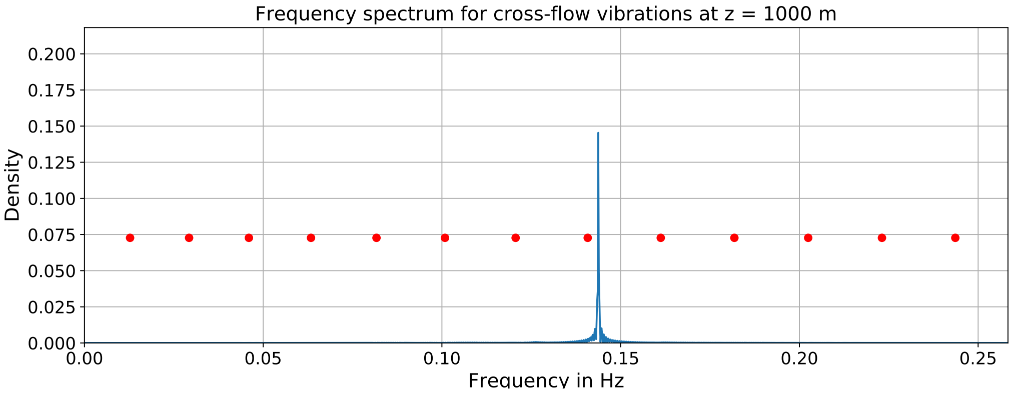

Figure 5.2: Frequency density spectrum for the given model run (natural frequencies depicted with red dots)

Table 5.3: Summary of outputs

Displacements	
Maximum in-flow displacement (u/D_e)	42.79
Maximum cross-flow displacement(v/D_e)	1.260
Stresses	
Maximum normal stress (N/m^2)	$84.44 \cdot 10^6$
Percentage of yield stress	35.2%
Maximum absolute shear stress (N/m^2)	$47.20 \cdot 10^3$
Percentage of maximum allowable shear stress	0.034%
Fatigue	
Fatigue damage per year	0.0192

5.2. Typical cold water pipe

In order to get a clear overview of what VIV might look like in a typical cold water pipe of an OTEC plant, the model is run with a pipe of a larger diameter in the same circumstances as the riser from before. The goal of this is to simulate a scenario that is realistic for the current state of the art of the cold water pipe. A HDPE pipe with a diameter of 2.5 m and wall thickness 0.15 m ($D_e/t \approx 16$), tensioned with a 350 tonnes ballast mass is subjected to a uniform flow velocity of 0.2 m/s. The ballast mass is added because of the lightness of the HDPE material. The model parameters can be found in Tab. 5.4. Since the pipe is expected to shed at a low frequency, the pipe is discretised in 40 elements setting the element length at 25 m.

The natural frequencies of this system are listed in Appendix B.2. From Tab. B.3 it can be found that the shedding will most likely occur in one of the nodes summarised in Tab. 5.5.

Table 5.5: Natural frequencies and corresponding current velocities

Mode number	**Nat. freq. in rad/s**	**Nat. freq. in Hz**	**Current velocity in m/s**
1	0.024	0.004	0.049
2	0.076	0.012	0.156
3	0.130	0.021	0.267
4	0.186	0.030	0.384

Fig. 5.3 shows snapshots of several states of the cross-flow displacement in the pipe, as well as the displacement in the u,v-plane at the point of maximum displacement which in this case is the free-hanging riser end. It can immediately be observed that the riser sheds close to the second mode. Furthermore, it can be seen that the cross-flow vibration amplitude is in the order of $1.0D_e$.

Fig. 5.4 shows the frequency density spectrum of the pipe subjected to a uniform 0.2 m/s current. The natural frequencies are depicted as red dots. It can be seen that the system vibrates close to the second mode.

Table 5.4: Pipe parameters and model parameters for typical cold water pipe

Pipe parameters			
Material		HDPE	
Length	L	1000	m
Outer diameter	D_e	2.5	m
Wall thickness	t	0.15	m
Pipe material density	ρ_p	950	kg/m^3
Young's modulus	E	$0.7056 \cdot 10^9$	N/m^2
Gravitational constant	g	9.81	m/s^2
Ballast mass	m_{bw}	$350 \cdot 10^3$	kg
Seawater and fluid parameters			
Sea water density	ρ_w	1026.6	kg/m^3
Fluid intake density	ρ_f	1027.6	kg/m^3
Fluid intake velocity	U_f	2.3	m/s

Model parameters			
Added mass coefficient	C_a	1	-
Element length	Δz	25	m
Drag coefficient	$C_{x0}^{\hat{0}}$	1.1856	-
Lift coefficient	$C_{y1}^{\hat{0}}$	0.3842	-
Strouhal number	St	0.1932	-
Tuning parameter	ε	0.7	-
Tuning parameter	A	12	-
Wake oscillator amplitude	q_1	2	-
Current parameters			
Type		Uniform	
Magnitude	V_c	0.2	m/s

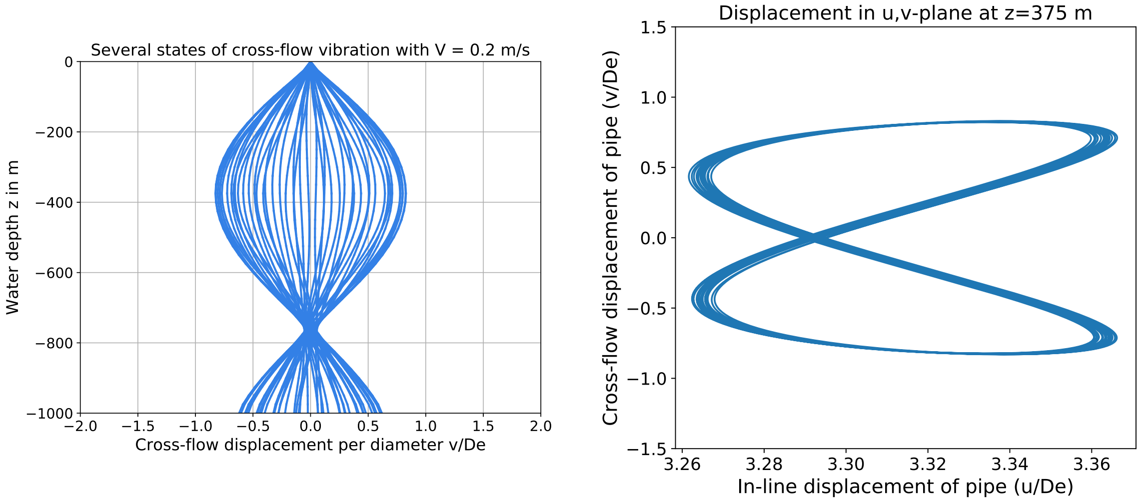

Figure 5.3: Several snapshots of the state of the cross-flow vibration of the pipe divided by the diameter(left) and the displacement in the u,v-plane at the point of maximum displacement (right)

A summary of all the calculated outputs was given in Appendix B.2. The results of the model run are summed up in Tab. 5.6.

Conclusion

The immediate conclusion that can be drawn from this simulation of a typical cold water pipe, is that the occurrence of VIV is very likely. The large diameter of the pipe leads to shedding in a very low mode, which in turn leads to low stresses and low fatigue damage due to VIV. Another observation that can be made is that the drag is reduced greatly due to the high tension in the pipe. The relative oscillation amplitude is slightly smaller than the one of the steel riser, and this might be caused by the extra mass at the end or the bigger wall thickness. Although the values are hard to compare to a typical riser system, the characteristics are very similar to regular vortex-induced vibration occurrences.

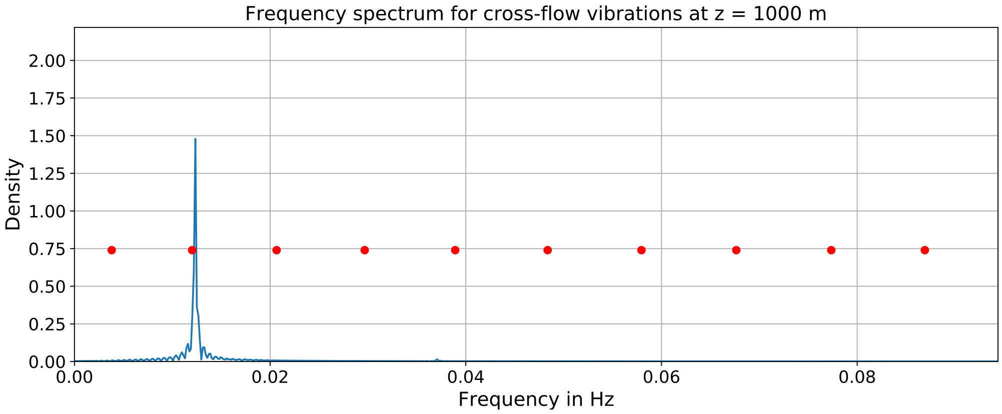

Figure 5.4: Frequency density spectrum for typical cold water pipe (natural frequencies depicted with red dots)

Table 5.6: Summary of outputs for typical cold water pipe

Displacements	
Maximum in-flow displacement (u/D_e)	5.239
Maximum cross-flow displacement(v/D_e)	0.831
Stresses	
Maximum normal stress (N/m^2)	$3.532 \cdot 10^6$
Percentage of yield stress	14.1%
Maximum absolute shear stress (N/m^2)	$2.239 \cdot 10^3$
Percentage of maximum allowable shear stress	0.015%
Fatigue	
Fatigue damage per year	$1.360 \cdot 10^{-30}$

5.3. Material

Now that a clear image has been established of what VIV in a cold water pipe might look like, the model can be used to check for the dependency on the material used for the structure. The materials that will be evaluated are listed in Chapter 4, to wit steel, FRP and HDPE. Steel is the material that is most often used since it's strong, reliable and cheap. However, for pipes of the size investigated here, it might prove impractical to use steel due to the lack of possibilities to produce and install a pipe of this size, as well as the weight of the pipe. FRP could prove a good alternative since it's lighter and more resistant to fatigue. HDPE is the material that is most often considered in OTEC, due to the ability to produce it at large diameters and it's lightness. The lack of mass however also means that the pipe has to be tensioned with a ballast mass, to prevent the buoyancy from making the system unstable.

The pipe setup that is considered here is the same as that of the typical cold water pipe setup considered previously, which means a length of 1000 m, diameter of 2.5 m and a wall thickness of 0.15 m. The only variable that will change per run is the material, which means the density, the stiffness and the friction will differ. In order to ensure that all the differences occurring between model runs are caused by material properties, all the pipes will be fitted with a ballast mass of 350 tonnes at the bottom, even though the steel pipe and the FRP would not necessarily need it. The pipe will be subjected to a uniform current velocity of 0.4 m/s. This way the pipe will shed in a higher mode than previously considered and the differences between model runs will be more clearly visible.

The material specific pipe parameters are listed in Tab. 5.8. All the parameters that are not listed are assumed the same as defined in Tab. 5.4. The natural frequencies for the given pipe in each separate material are listed in Appendix B.3. For all the different materials, the shedding will most likely occur in one of the nodes listed in Tab. 5.7. Figs. 5.5, 5.6 and 5.7 shows snapshots of the state of cross-flow vibration for all three different materials subjected to the same uniform current, as well as their displacement in the u,v-plane at the point of maximum cross-flow displacement.

Table 5.7: Natural frequencies and corresponding current velocities

	Steel			**FRP**			**HDPE**		
Mode number	**Nat. freq. in rad/s**	**Nat. freq. in Hz**	**Current velocity in m/s**	**Nat. freq. in rad/s**	**Nat. freq. in Hz**	**Current velocity in m/s**	**Nat. freq. in rad/s**	**Nat. freq. in Hz**	**Current velocity in m/s**
1	0.076	0.012	0.156	0.038	0.006	0.079	0.024	0.004	0.049
2	0.192	0.031	0.396	0.110	0.018	0.227	0.076	0.012	0.156
3	0.364	0.058	0.751	0.159	0.025	0.327	0.130	0.021	0.267
4	0.551	0.088	1.135	0.203	0.032	0.418	0.186	0.030	0.384
5	0.556	0.089	1.146	0.314	0.050	0.646	0.245	0.039	0.504

Table 5.8: Pipe parameters and model parameters for pipe in different materials

Steel			
Length	L	1000	m
Outer diameter	D_e	2.5	m
Wall thickness	t	0.15	m
Pipe material density	ρ_p	7800	kg/m^3
Young's modulus	E	$211 \cdot 10^9$	N/m^2
Current type		Uniform	
Magnitude	V_c	0.4	m/s
FRP			
Length	L	1000	m
Outer diameter	D_e	2.5	m
Wall thickness	t	0.15	m
Pipe material density	ρ_p	1800	kg/m^3
Young's modulus	E	$26 \cdot 10^9$	N/m^2
Current type		Uniform	
Magnitude	V_c	0.4	m/s
HDPE			
Length	L	1000	m
Outer diameter	D_e	2.5	m
Wall thickness	t	0.15	m
Pipe material density	ρ_p	950	kg/m^3
Young's modulus	E	$0.7056 \cdot 10^9$	N/m^2
Current type		Uniform	
Magnitude	V_c	0.4	m/s

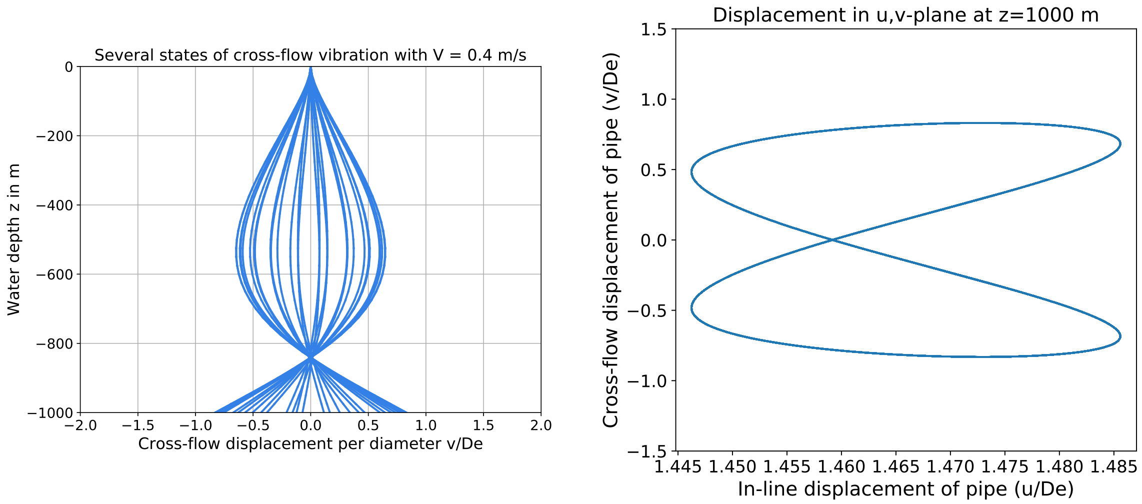

Figure 5.5: Several snapshots of the state of the cross-flow vibration of the pipe divided by the diameter for the pipe in steel (left), and the displacement in the u,v-plane for the pipe at the point of maximum cross-flow displacement (right)

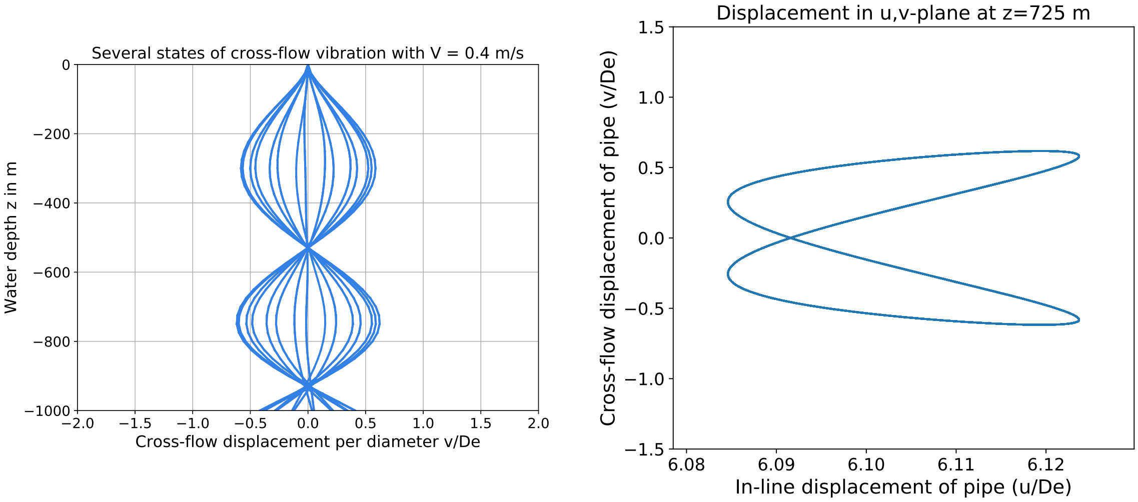

Figure 5.6: Several snapshots of the state of the cross-flow vibration of the pipe divided by the diameter for the pipe in FRP (left), and the displacement in the u,v-plane for the pipe at the point of maximum cross-flow displacement (right)

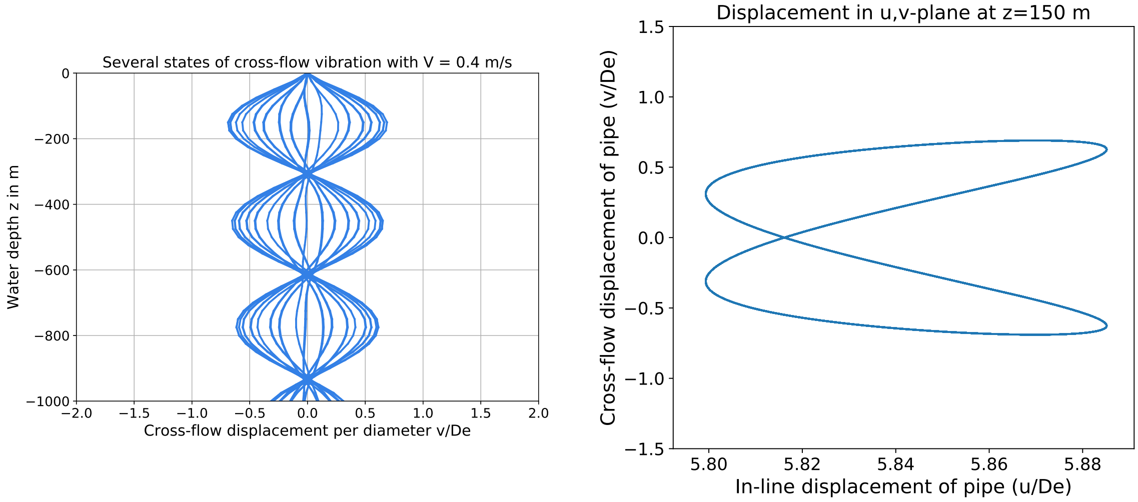

Figure 5.7: Several snapshots of the state of the cross-flow vibration of the pipe divided by the diameter for the pipe in HDPE (left), and the displacement in the u,v-plane for the pipe at the point of maximum cross-flow displacement (right)

It can immediately be observed that the shapes of the cross-flow vibrations differ per material. The steel pipe has the largest maximum amplitude oscillation and it sheds at the second mode. The FRP pipe, although the velocity seems closer to the fourth mode, appears to shed at the third mode. The HDPE pipe sheds at the highest mode, to wit the fourth. It can also be seen that the ballast mass has more influence on the lighter materials, where the pipe end of the HDPE pipe is clearly being held back by the mass. The displacements in the u,v-plane are all of the typical shape and in the same order of magnitude.

Fig. 5.8 shows the frequency density spectrum of all the materials. For steel and HDPE, the spectra are according to the expectations raised by the snapshots of the pipe displacements. For FRP however, the spectrum shows some peculiarities that might explain the discrepancy between the image of the pipe shedding in the third mode and the velocity being close to that corresponding to the fourth mode. It can be seen that the largest amount of energy is close to the fourth mode, however there is also a smaller amount of energy between the second and third mode.

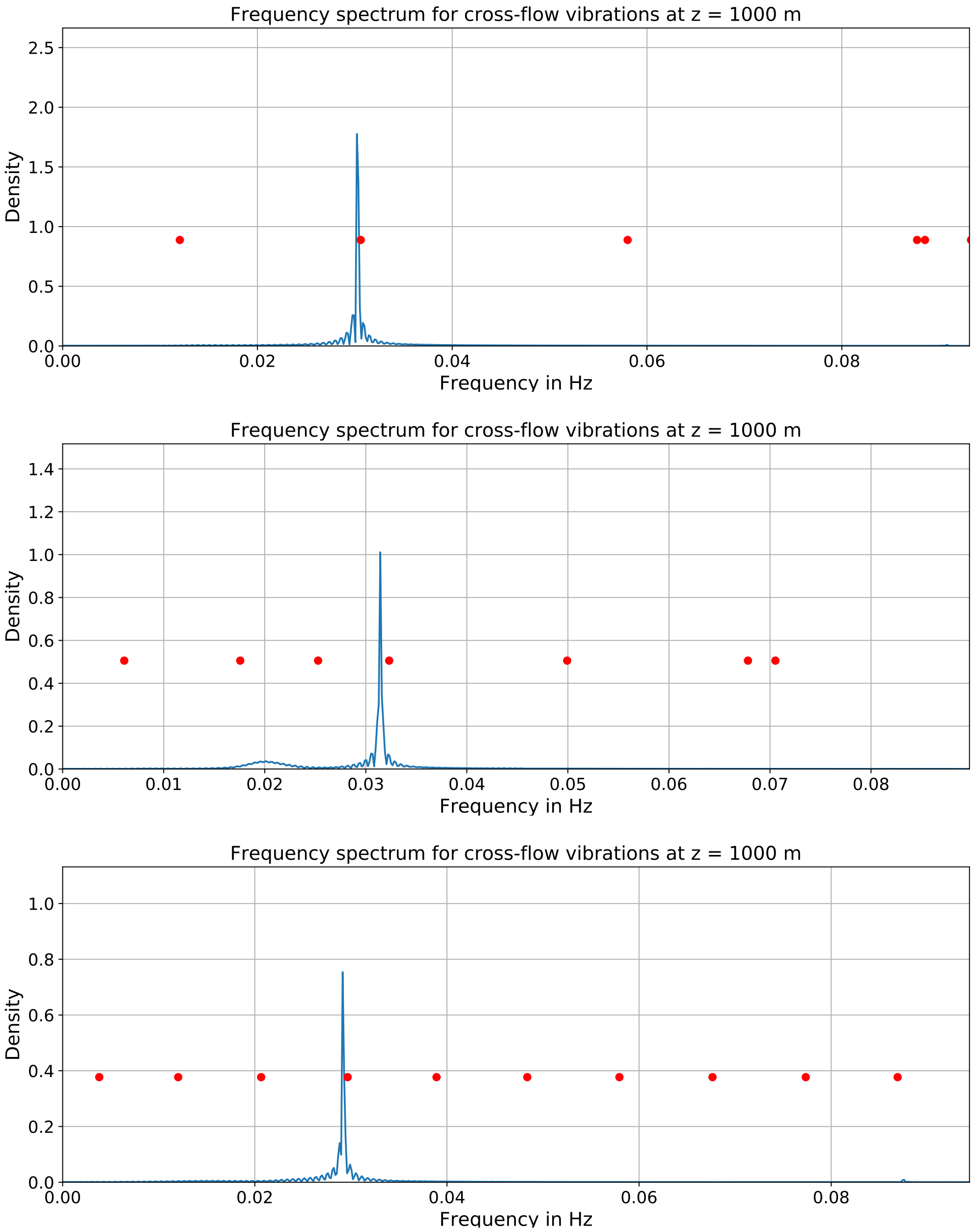

Figure 5.8: Frequency density spectra for the pipe in different materials: steel (top), FRP (centre) and HDPE (bottom) (natural frequencies depicted with red dots)

Tab. 5.9 gives a summary of the most important outputs of the model runs for different materials. For the full outputs, one might refer to Appendix B.3. It is found that steel has the largest amplitude cross-flow vibration, followed by FRP. HDPE has the smallest cross-flow vibration amplitude, however it sheds at the highest mode. For the in-line displacement, it becomes clear that the steel pipe will stay more or less in its starting position. This can be accredited to the enormous self-weight of this pipe, as the FRP and HDPE pipes do displace a significant amount in the in-line direction. It is found that the maximum normal stress compared to yield stress is the most critical for steel. This can be accredited to the immense mass of a steel pipe in this size, however it is still well within an acceptable range. For both FRP and HDPE the maximum normal stress is not close to the yield stress. As in the previous model runs, the shear stress is insignificant compared to the other stresses and forces. Finally, the fatigue per material shows some interesting characteristics. Although FRP is supposed to be more resistant to fatigue than steel, the fact that it sheds at a higher frequency than steel at the same uniform velocity, leads to a larger amount of stress-cycles in the same time frame, finally leading to a lower long-term fatigue level for steel. HDPE however is in another order in terms of long term fatigue level. It seems that due to the comparatively low stiffness in HDPE, the stress-cycle is at such a low level that it has barely any influence on the fatigue level of the structure. It seems therefore, along with the advantages in terms of production, installation and costs, the preferable material for an OTEC cold water pipe.

Table 5.9: Summary of outputs for cold water pipe in different materials

	Steel	**FRP**	**HDPE**
Displacements			
Maximum in-flow displacement (u/D_e)	1.486	7.385	20.74
Maximum cross-flow displacement(v/D_e)	0.831	0.713	0.690
Stresses			
Maximum normal stress (N/m^2)	$120.1 \cdot 10^6$	$38.53 \cdot 10^6$	$6.551 \cdot 10^6$
Percentage of yield stress	50.0%	30.8%	26.2%
Maximum absolute shear stress (N/m^2)	$208.6 \cdot 10^3$	$177.4 \cdot 10^3$	$25.75 \cdot 10^3$
Percentage of maximum allowable shear stress	0.103%	0.25%	0.18%
Fatigue			
Fatigue damage per year	0.005	0.060	$4.37 \cdot 10^{-30}$

Conclusion

The conclusion that can be drawn from the model runs of the same cold water pipe in different materials, is that the choice of material makes a significant impact on the VIV. Due to the difference in stiffness and pipe density the pipe will shed in different modes at the same current velocity. This means different cross-flow displacement amplitudes, as well as different shedding frequencies. It seems that HDPE is the most viable option in terms of resistance to VIV. It shows the smallest cross-flow vibration amplitude as well as excellent fatigue resistance.

5.4. Diameters

From Section 5.3 it can be concluded that HDPE is the most suitable material for the construction of an OTEC cold water pipe. Another interesting aspect to evaluate is the influence of the diameter of the pipe. The diameter of the pipe will most probably be decided by the power that the plant will produce, since a higher amount of theoretical power requires more cold water to be pumped up, ergo a larger diameter. The diameter can however have a significant effect on the occurrence of VIV, since it alters the system in for example the area of the pipe leading to different stresses, the moment of inertia and the drag force (which is coupled to the lift force). In conclusion, a change in diameter might result in a very different situation in terms of VIV.

Table 5.10: Pipe parameters and model parameters for HDPE pipe in different diameters

Pipe parameters			
Material		HDPE	
Length	L	1000	m
Outer diameter	D_e	2.0-6.0	m
Wall thickness	t	$D_e/20$	m
Pipe material density	ρ_p	950	kg/m^3
Young's modulus	E	$0.7056 \cdot 10^9$	N/m^2
Gravitational constant	g	9.81	m/s^2
Ballast mass	m_{bw}	$500 \cdot 10^3$	kg
Seawater and fluid parameters			
Sea water density	ρ_w	1026.6	kg/m^3
Fluid intake density	ρ_f	1027.6	kg/m^3
Fluid intake velocity	U_f	2.3	m/s

Model parameters			
Added mass coefficient	C_a	1	-
Element length	Δz	25	m
Drag coefficient	$C^{\hat{0}}_{x0}$	1.1856	-
Lift coefficient	C^{0}_{y1}	0.3842	-
Strouhal number	St	0.1932	-
Tuning parameter	ε	0.7	-
Tuning parameter	A	12	-
Wake oscillator amplitude	q_1	2	-
Current parameters			
Type		Uniform	
Magnitude	V_c	0.4	m/s

In order to investigate this effect of the diameter on the nature of VIV, the pipe model is run with a pipe in HDPE of 1000 m length subjected to a uniform current of 0.4 m/s. The diameter of the pipe will be varied between 2 and 6 m (a range of diameters that is realistic for potential OTEC plants) in steps of 0.5 m. In order to make sure that the differences that occur between the different runs are caused by the change in diameter, the wall thickness to diameter ratio is kept constant at $t/D_e = 1/20$. For the smaller diameters this might be interpreted as a thin wall, but it ensures that for the larger diameters the wall thickness is still somewhat reasonable. The effect of the wall thickness ratio is evaluated at a later stage. Another consideration that needs to be discussed is the presence of the ballast mass. Since the 350 tonnes that has been used before is not sufficient to suppress the buoyancy of the larger pipes and will cause instability, every single pipe is tensioned with a ballast mass of 500 tonnes, to confirm once again that no other variables differ between the model runs except for the diameter. The pipe and model parameters can be found in Tab. 5.10.

Summary of results

Since it's impossible to visualise the complete results of all the model runs, this short intermezzo is dedicated to a summary of all the notable results that are not presented in this thesis. The pipes with diameters ranging from 2.0-3.0 m will shed close to the third mode, the pipes with a diameter in the range of 3.0-5.5 m will shed mainly in the third mode but a lot of energy will also be found in the fourth mode, and the pipes in a range of 5.5-6.0 m will shed in the fourth mode. The u,v-displacement planes of the pipes look as expected, however there are some unregularities due to the pipe shedding at multiple modes at some diameters. This effect can most likely be ascribed to the use of a heavy ballast mass, giving the pipe an unusual high stiffness.

Fig. 5.9 gives an overview of the maximum in-line and cross-flow displacement per diameter, for each diameter that has been evaluated. It can be seen that the in-line displacement increases more or less exponentially with the increase of the diameter. This can be accredited to the increase of drag force. More interesting in terms of VIV however is the cross-flow vibration per diameter. It can be seen that for the smaller diameters the cross-flow displacement per diameter rapidly increases, but for the diameters ranging between 3.0 and 6.0 m it remains between 0.8 and 0.9. This might be caused by the fact that the lower diameters shed in the

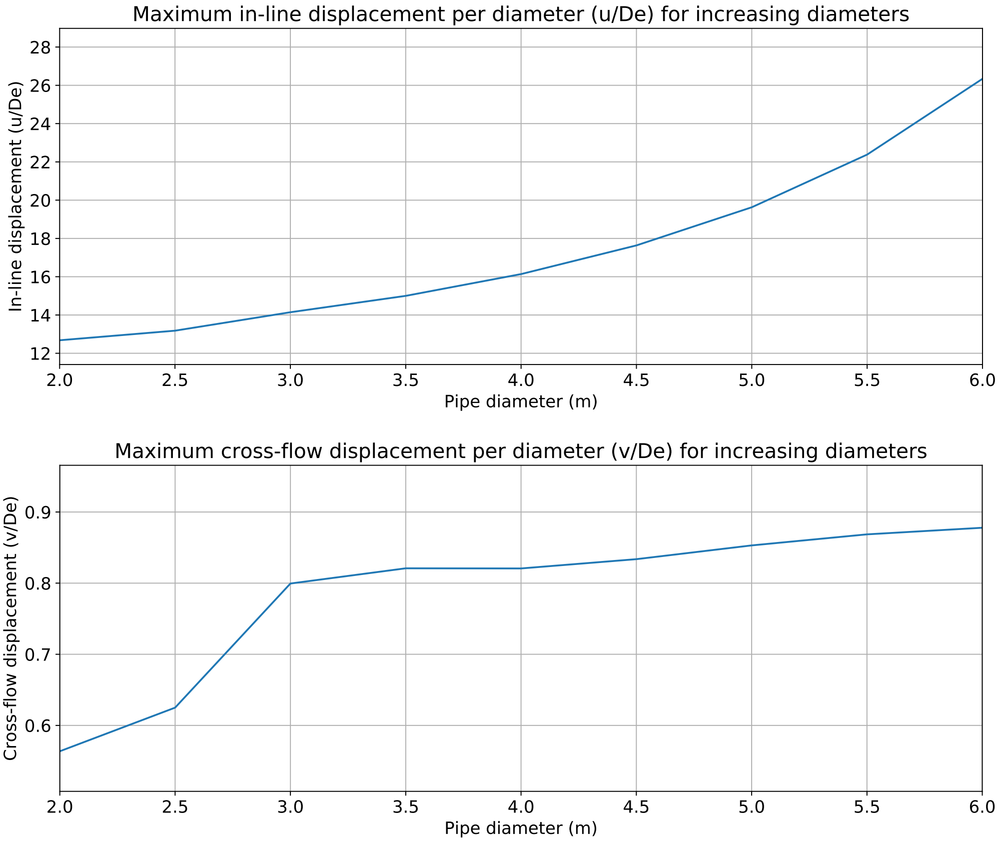
Maximum in-line displacement per diameter (u/De) for increasing diameters

Maximum cross-flow displacement per diameter (v/De) for increasing diameters

Figure 5.9: Overview of maximum in-line displacement per diameter (top) and the maximum cross-flow displacement per diameter (bottom) for increasing diameters

fourth mode and for diameters larger than 3.0 m the shift is made to the third mode, causing them to stay more or less in the same range. Fig. 5.10 shows the maximum normal stress as percentage of the yield stress for the pipe in each diameter that has been evaluated.

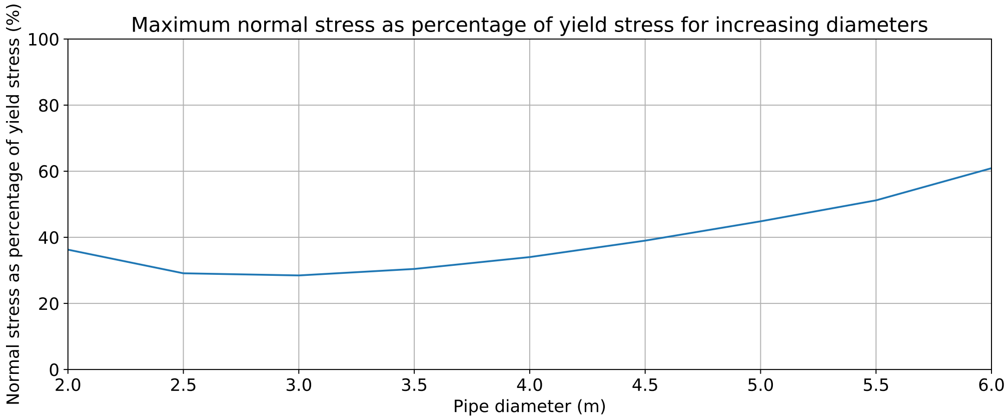

Figure 5.10: Overview of maximum normal stress as compared to yield stress of HDPE for increasing diameters

In terms of normal stress, the optimum seems to be at a diameter of 3.0 m. Smaller diameters will have a higher shedding mode, leading to more bending stress, while larger diameters will suffer from as a higher bending stress due to a larger moment of inertia. It has to be noted however that even for pipes with a diameter of 6.0 m the normal stress will remain well within an acceptable range relative to the yield stress. Fig. 5.11 shows the fatigue level per year for the pipe in each diameter that has been evaluated.

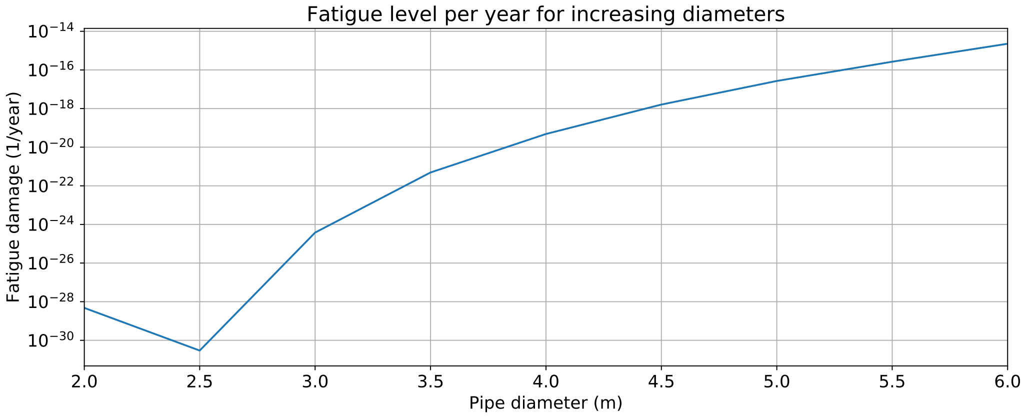

Figure 5.11: Overview of fatigue damage per year for increasing diameters

The main conclusion that can be drawn from evaluating the fatigue damage levels per year, is that HDPE has sufficient fatigue resistance at each diameter. The optimum in terms of fatigue seems to be around a diameter of 2.5 m. For the other diameters, the fatigue damage per year is insignificant too, so if needed a large diameter pipe can be used without fatigue being the limiting factor. A summary of the results that are discussed is given in Tab. 5.11. The full table of outputs can be found in Appendix B.4.

Table 5.11: Summary of outputs for cold water pipe in different diameters

Diameter (m)	**2.0**	**2.5**	**3.0**	**3.5**	**4.0**	**4.5**	**5.0**	**5.5**	**6.0**
Max. u/D_e	12.68	13.18	14.14	15.00	16.14	17.64	19.63	22.38	26.34
Max. v/D_e	0.564	0.625	0.799	0.821	0.821	0.834	0.853	0.869	0.878
Max. σ as % of σ_y	36.3	29.1	28.5	30.4	34.0	39.0	44.8	51.2	60.9
D per year	4.78E-29	2.95E-31	3.79E-25	4.91E-22	4.82E-20	1.61E-18	2.68E-17	2.66E-16	2.27E-15

Conclusion

The conclusion that can be drawn from this section is that it in terms of VIV resistance, it is possible to create a pipe up to very large diameters. HDPE seems to have enough fatigue resistance for a pipe of 6.0 m diameter to still remain well within the fatigue limits when subjected to a uniform flow velocity of 0.4 m/s. The normal stress of the pipe at large diameters seems to become a problem before the fatigue due to vortex shedding will be come a problem.

5.5. Wall thickness

As well as the diameter, the wall thickness of the pipe may have a certain influence on vortex shedding. Most probably in a realistic situation the wall thickness will be determined by the choice of diameter, as pipes are being made in specific diameter-to-wall thickness ratios. Typical standard dimension ratios for HDPE are for example $D_e/t = 14$, 17 or 21. As the diameter, the main way in which the wall thickness influences the pipe material is that a change in wall thickness means a change in amount of material, and therefore different forces, stresses and response. To evaluate the influence of the wall thickness the typical cold water pipe of Section 5.2 is evaluated again, but this time in different runs each time with a different wall thickness, as the diameter is kept constant. The pipe is once again subjected to a uniform current flow of 0.4 m/s over its length. The range of wall thicknesses that has been evaluated is $D_e/t = 26$ (96 mm) through $D_e/t = 12$ (208 mm) with steps of $D_e/t = 2$. This means that not all the standard dimension ratios have been checked but it covers a large range of the possibilities. Furthermore, it has to be noted once again that not all the evaluated situations are to be considered realistic, since this is merely a theoretical exercise to evaluate the influence of variables. The pipe and model parameters can be found in Tab. 5.12.

Table 5.12: Pipe parameters and model parameters for HDPE pipe with varying wall thickness

Pipe parameters			
Material		HDPE	
Length	L	1000	m
Outer diameter	D_e	2.5	m
Wall thickness	t	$D_e/26 - D_e/12$	m
Pipe material density	ρ_p	950	kg/m^3
Young's modulus	E	$0.7056 \cdot 10^9$	N/m^2
Gravitational constant	g	9.81	m/s^2
Ballast mass	m_{bw}	$350 \cdot 10^3$	kg
Seawater and fluid parameters			
Sea water density	ρ_w	1026.6	kg/m^3
Fluid intake density	ρ_f	1027.6	kg/m^3
Fluid intake velocity	U_f	2.3	m/s

Model parameters			
Added mass coefficient	C_a	1	-
Element length	Δz	25	m
Drag coefficient	$\hat{C}_{x0}^{0}$	1.1856	-
Lift coefficient	$\hat{C}_{y1}^{0}$	0.3842	-
Strouhal number	St	0.1932	-
Tuning parameter	ε	0.7	-
Tuning parameter	A	12	-
Wake oscillator amplitude	q_1	2	-
Current parameters			
Type		Uniform	
Magnitude	V_c	0.4	m/s

Summary of results

As in the previous section concerning diameters, the amount of runs done in this evaluation is too much to completely visualise in this thesis, therefore this short interlude will describe the main takeaways from the analysis. For each wall thickness the pipe will shed at the fourth mode, since the natural frequencies do not vary much. The u,v-plane displacement plots look as expected, and therefore there are no peculiarities that need further elaboration.

Fig. 5.12 gives an overview of the maximum in-line and cross-flow displacement per diameter, for each diameter to wall thickness ratio that has been evaluated. The first thing that immediately jumps to the eye is that for standard dimension ratio (and thus decreasing wall thickness), the displacement in both in-line and cross-flow direction is decreasing. This seems counter-intuitive, as it would be more logical that a thicker pipe had more resistance and would therefore not displace as far as a thin walled pipe. This behaviour can be ascribed however to the material properties of HDPE. Since HDPE has a lower mass density than the cold seawater that is being conveyed through the pipe ($\rho_{HDPE} = 950$ kg/m^3 versus $\rho_f = 1027.6$ kg/m^3) the net mass per unit length of the pipe is lower as the wall thickness gets bigger. This leads to smaller displacements for pipes with thinner walls in the case of HDPE. A simple check for this statement is varying the wall thickness

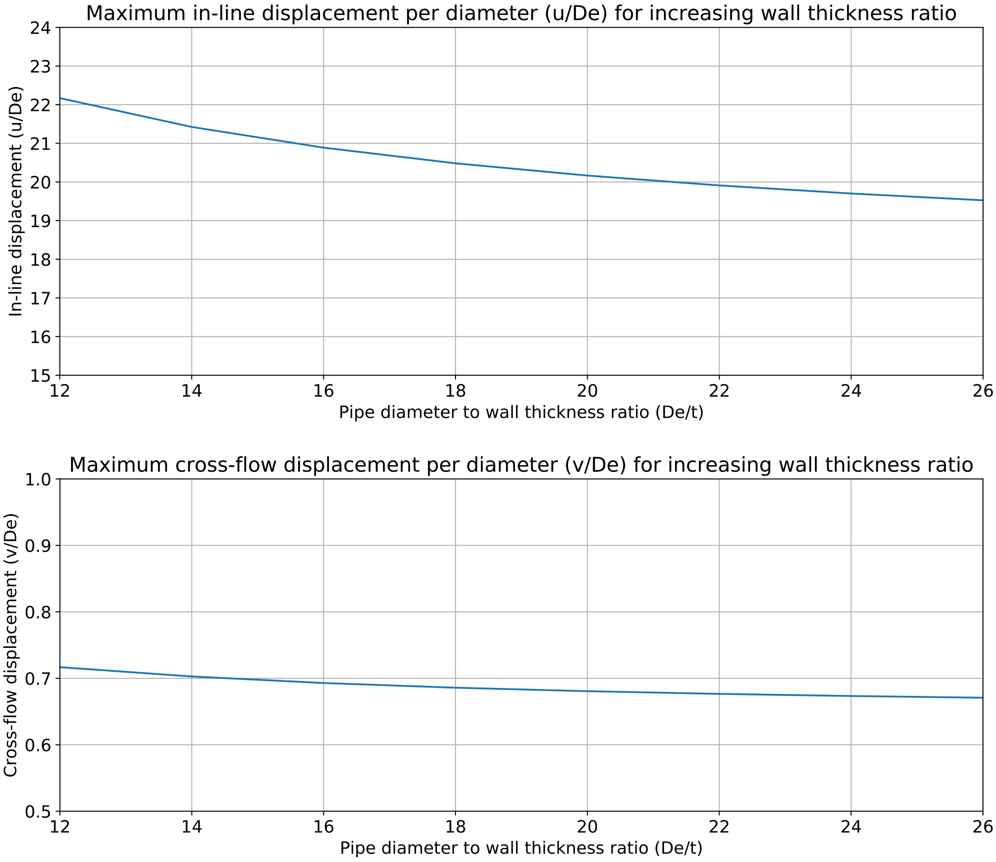

Figure 5.12: Overview of maximum in-line displacement per diameter (top) and the maximum cross-flow displacement per diameter (bottom) for increasing diameter to wall thickness ratio

for a pipe in heavier material, for example steel, and it can be found that the displacements decrease with increasing wall thickness. From the figures it can also be derived however that the effect of wall thickness is not exceptionally large, since the pipe will stay in the range of a cross-flow vibration per diameter of 0.67 to 0.73.

From Fig. 5.13 it can be seen that the maximum normal stress as compared to the yield stress of the pipe increases as the wall thickness becomes smaller. Apparently the bending moments and forces do not vary too much between the different pipes (they all shed in the fourth mode at more or less the same amplitude). However, as the pipe with smaller wall thicknesses have a smaller cross-sectional pipe area, the stresses become slightly larger than for the pipes with bigger wall thickness. Still, for every evaluated wall thickness the stress remains well within the acceptable range.

Table 5.13: Summary of outputs for cold water pipe in different diameter to wall thickness ratios

Diameter to wall thickness ratio (D_e/t)	**12**	**14**	**16**	**18**	**20**	**22**	**24**	**26**
Max. u/D_e	22.17	21.42	20.89	20.48	20.17	19.91	19.70	19.53
Max. v/D_e	0.717	0.703	0.693	0.686	0.681	0.677	0.673	0.671
Max. σ as % of σ_y	24.2	25.0	25.9	26.9	28.0	29.1	30.3	31.5
D per year	9.08E-26	2.25E-26	6.41E-27	1.98E-27	6.57E-28	2.35E-28	8.73E-29	3.40E-29

From the fatigue levels depicted in Fig. 5.14 it can be concluded that for the evaluated range of wall thickness the pipe will not be in danger of succumbing to fatigue when subjected to a current velocity of 0.4 m/s. Since the fatigue is mainly depending on difference between the maximum and minimum of the stress cycle (in this case the bending stress due to VIV), the pipes with a bigger wall thickness will suffer slightly more to fatigue, because of their larger displacement amplitude and their larger moment of inertia, leading

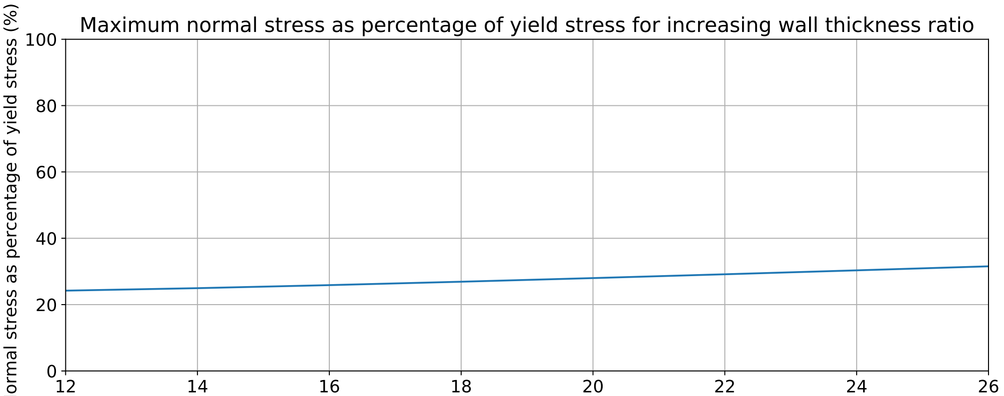

Figure 5.13: Overview of maximum normal stress as compared to yield stress of HDPE for increasing diameter to wall thickness ratio

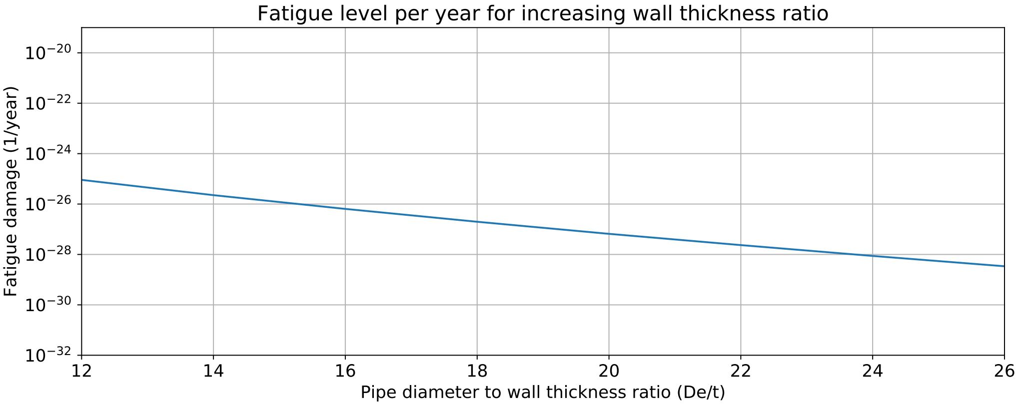

Figure 5.14: Overview of fatigue damage per year for increasing diameter to wall thickness ratio

to higher bending stresses. A summary of the discussed results is given in Tab. 5.13. The full table of outputs can be found in Appendix B.5.

Conclusion

The conclusion that can be drawn from this section is that it in terms of VIV resistance, the wall thickness has a certain influence but not as much as for example the diameter. A HDPE pipe of 2.5 m diameter subjected to a uniform flow velocity of 0.4 m/s will be able to sustain VIV for all the diameter to wall thickness ratios that were evaluated. This means that wall thickness will most probably not be a problem.

5.6. Ballast mass

As has been discussed before, pipe in lighter materials are deployed with a ballast mass at the pipe end. The main reason for applying a ballast mass to a pipe is keeping it tensioned to prevent buckling. For a more in-depth analysis of the magnitude of the ballast mass used in combination with different pipe materials, the work of Acevedo et al. [6] might be consulted. The goal of this section is evaluating how the magnitude of the ballast mass influences the VIV response. Intuitively, it seems logical to use a ballast mass as small as possible to reduce weight and therefore stresses. However, a larger ballast mass might lead to the pipe becoming stiffer, shedding in a lower mode, and therefore performing better in terms of fatigue. In order to evaluate this behaviour, the typical cold water pipe of HDPE with a diameter of 2.5 m and 1000 m length is once again investigated, this time with a varying range of ballast masses. The pipe is once again subjected to a uniform current flow of 0.4 m/s. The ballast mass will be varied in a range between 200 tonnes and 1000 tonnes in steps of 200 tonnes, as these values to be a more or less realistic possibility. A pipe without ballast mass causes instability in the model (due to buckling) and therefore the outputs for this possibility are not shown. The pipe and model parameters can be found in Tab. 5.14.

Table 5.14: Pipe parameters and model parameters for HDPE pipe with varying ballast mass

Pipe parameters			
Material		HDPE	
Length	L	1000	m
Outer diameter	D_e	2.5	m
Wall thickness	t	0.15	m
Pipe material density	ρ_p	950	kg/m^3
Young's modulus	E	$0.7056 \cdot 10^9$	N/m^2
Gravitational constant	g	9.81	m/s^2
Ballast mass	m_{bw}	$200 - 1000 \cdot 10^3$	kg
Seawater and fluid parameters			
Sea water density	ρ_w	1026.6	kg/m^3
Fluid intake density	ρ_f	1027.6	kg/m^3
Fluid intake velocity	U_f	2.3	m/s

Model parameters			
Added mass coefficient	C_a	1	-
Element length	Δz	25	m
Drag coefficient	$C_{x0}^{\hat{0}}$	1.1856	-
Lift coefficient	$C_{y1}^{\hat{0}}$	0.3842	-
Strouhal number	St	0.1932	-
Tuning parameter	ε	0.7	-
Tuning parameter	A	12	-
Wake oscillator amplitude	q_1	2	-
Current parameters			
Type		Uniform	
Magnitude	V_c	0.4	m/s

Summary of results

The main thing that immediately shows from the pipe cross-flow displacement states in Appendix B.6, is that the magnitude of the ballast mass is of great influence to the VIV response of the pipe. For the smallest ballast mass the pipe will shed in the sixth mode at a high frequency. For the pipe with a medium ballast mass of 400 tonnes, the pipe will shed in the fourth mode, which is more or less comparable to the response found in Section 5.2. For the larger ballast masses of 600 and 800 tonnes, the pipe will shed in the third mode, but there is still some energy to be found at the higher modes as well. This effect was seen before by the evaluation of higher diameter pipes with ballast mass. At the highest ballast mass the pipe sheds close to the second mode with some energy in the third mode as well. The conclusion that can be drawn from this first impression is that a larger ballast mass will lead to the pipe shedding in lower modes. In general, lower modes lead to higher displacement amplitudes but lower bending stresses due to smaller curvature in the pipe.

Fig. 5.15 gives an overview of the maximum in-line and cross-flow displacement per diameter for each ballast mass that has been evaluated. In terms of in-line displacement the graph shows no peculiarities, as a smaller ballast mass leads to a very large in-line displacement and a larger ballast mass leads to the pipe remaining in near-vertical position. It can be assumed that for ballast masses lower than the evaluated range, the pipe will displace even further until reaching a point where the pipe tension is not enough to make up for the upwards buoyancy force and the pipe will start to buckle. The cross-flow displacement seems to vary mostly with the mode in which the pipe will shed. This can be seen as for the 200 tonnes mass the pipe sheds at the lowest amplitude, at 600 and 800 tonnes the pipe displacement amplitude remains more or less at the same magnitude due to these pipes shedding in the same mode and finally in the lowest mode the pipe sheds at the highest amplitude. This does however not say too much about forces, stresses and fatigue, since these are mainly determined by the pipe's rotation angle and curvature.

In terms of maximum normal stress, it clearly shows that the pipe does not suffer too much from the magnitude of the ballast mass. A small note that has to be made here, is that, as can be seen in Fig. B.6, for the ballast mass of the smallest magnitude, the discretisation in 40 elements might not be enough to fully capture the shape of the sixth shedding mode. What this means is that the curvature from the pipe (since it follows from the discretisation as per Eq. (4.30)) might not be accurate enough, and therefore the resulting bending stress might be slightly off from the real value. It is therefore important that these values are used with caution. The shape of the graph however seems to be compliant with intuition, as a pipe shedding at a higher mode will have a higher bending stress. It can be seen that as the bending stress goes lower at lower shedding modes, the ballast slightly takes over in terms of influence. At a ballast mass of 1000 tonnes however the pipe will still only be at around 40% of the yield stress in the case of HDPE. It can be found that for a yield stress of $\sigma_y = 25$ MPa the ballast mass can be up to 2500 tonnes before the yield stress is reached.

Fig. 5.17 shows the fatigue damage per year of the pipe for different ballast masses. The conclusion from this is pretty clear, to wit that a lower ballast mass leads to a higher fatigue level and vice versa. This can easily be explained by the fact that the fatigue is mainly determined by the VIV-induced bending stress. From this

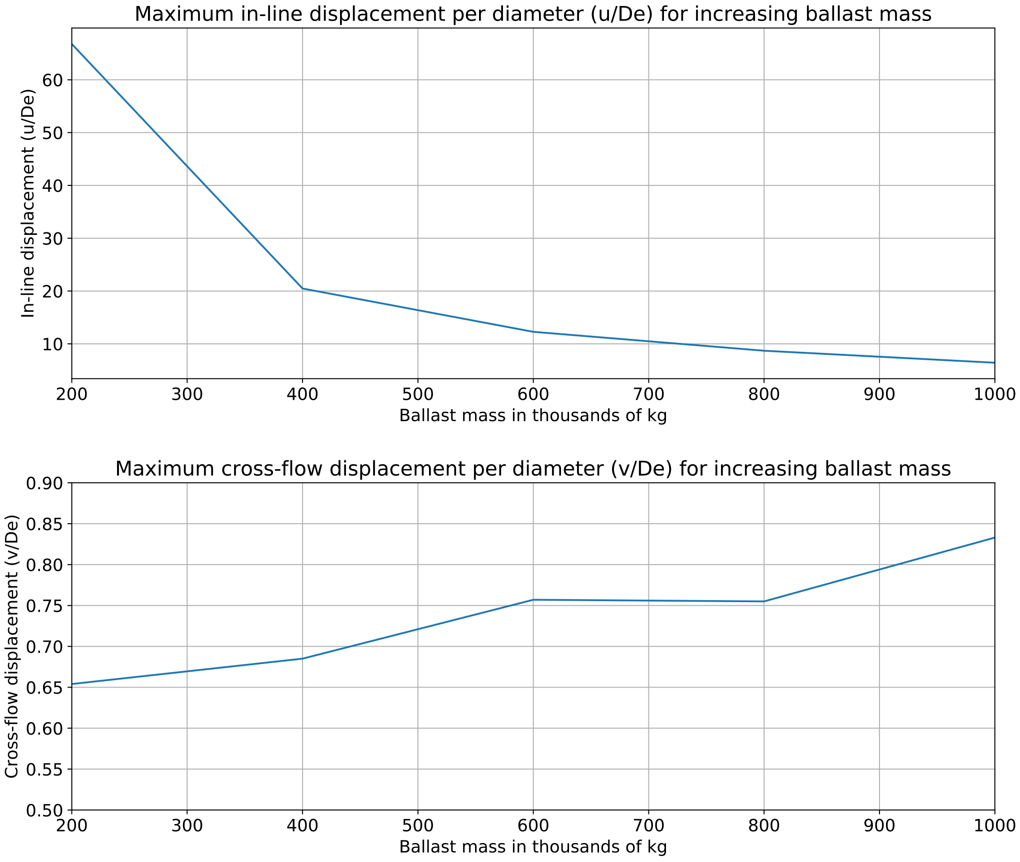

Figure 5.15: Overview of maximum in-line displacement per diameter (top) and the maximum cross-flow displacement per diameter (bottom) for increasing ballast mass

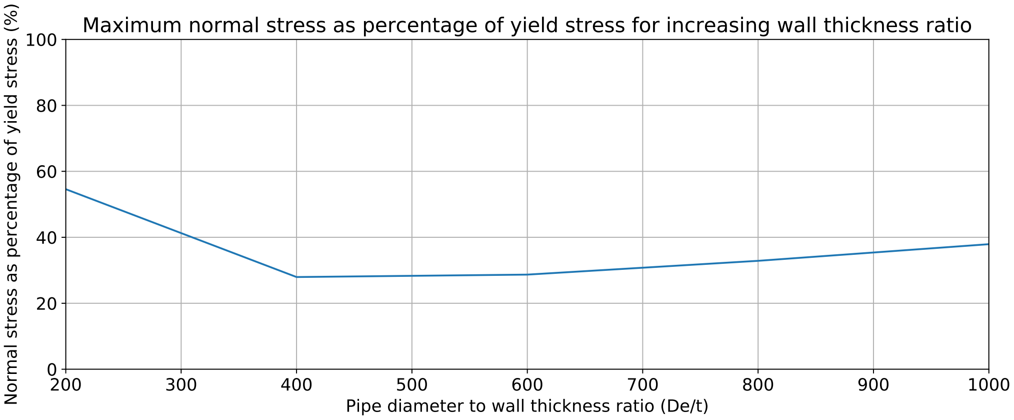

Figure 5.16: Overview of maximum normal stress as compared to yield stress of HDPE for increasing ballast mass

section it was concluded that the pipes with a lower ballast mass shed at a higher mode and therefore have more bending stress. The maximum stress cycle will thus be higher at lower ballast masses and the fatigue damage per year will be higher. A summary of the discussed results is given in Tab. 5.15. The full table of outputs can be found in Appendix B.6.

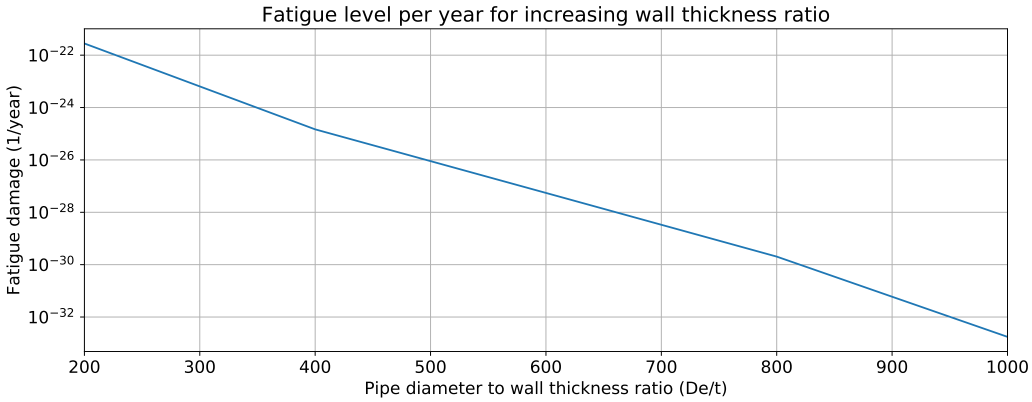

Figure 5.17: Overview of fatigue damage per year for increasing ballast mass

Table 5.15: Summary of outputs for cold water pipe in different diameter to wall thickness ratios

Ballast mass (10^3 kg) Compared to pipe mass	**200** 0.19	**400** 0.38	**600** 0.57	**800** 0.76	**1000** 0.95
Max. u/D_e	66.78	20.48	12.28	8.70	6.43
Max. v/D_e	0.654	0.685	0.757	0.755	0.833
Max. σ as % of σ_y	54.6	28.0	28.7	32.9	37.9
D per year	2.80E-22	1.47E-25	5.49E-28	2.03E-30	1.75E-33

Conclusion

The conclusion that can be drawn from the results in this section, is that the ballast mass can have a big influence on the VIV response of a HDPE cold water pipe. It seems to be a wise choice to make the ballast mass as large as possible, as it suppresses VIV greatly and it does not seem to have too much influence on the normal stress as compared to the yield stress. If it is preferred to use a small ballast mass for for example installation purposes, this will not be too much of a problem either, as the fatigue damage will not reach critical levels.

5.7. Inflow velocity

The entire purpose of the cold water pipe is pumping up the cold seawater from the bottom layer of the ocean's depth. The inflow velocity of the fluid in the pipe has a certain influence on the pipe behaviour as can be gathered from the equation of motion. This inflow velocity will be determined by the amount of water that is needed for the rated power of the plant, by the diameter of the pipe, and various other factors. In this thesis and in previous studies the inflow velocity is in general kept constant, although this seems to be a rather unrealistic situation. This section is dedicated to evaluating the influence of the velocity of the inflow through the pipe on the VIV response. A more in depth analysis of this and an evaluation of the response in the case of a varying inflow velocity can be found in Chapter 6. In this section the typical cold water pipe setup will be evaluated, first with an inflow velocity of 0 m/s to see in which way the pipe will respond when there is no moving fluid, and then with an inflow velocity ranging from 1.0 m/s to 6.0 m/s. For a complete validation of the range the pipe would have to be checked on stability for the given inflow velocities, but in this thesis these checks will not be performed. The pipe and model parameters can be found in Tab. 5.16.

No inflow velocity

The situation where there is no inflow velocity will not occur often, but it might occur as for example the pump stops working due to whatever reason and the pipe is still full of cold sea water. Appendix B.7 might be consulted for an overview of the states of cross-flow vibration and the displacement of the pipe in the u,v-plane. All the outputs can be found in this Appendix as well. As can be seen here, the pipe will vibrate in the fourth mode when there is no inflow velocity. All the results are more or less comparable to the results found for the analysis of the typical cold water pipe in Section 5.2.

Table 5.16: Pipe parameters and model parameters for HDPE pipe with varying inflow velocity

Pipe parameters			
Material		HDPE	
Length	L	1000	m
Outer diameter	D_e	2.5	m
Wall thickness	t	0.15	m
Pipe material density	ρ_p	950	kg/m^3
Young's modulus	E	$0.7056 \cdot 10^9$	N/m^2
Gravitational constant	g	9.81	m/s^2
Ballast mass	m_{bw}	$350 \cdot 10^3$	kg
Seawater and fluid parameters			
Sea water density	ρ_w	1026.6	kg/m^3
Fluid intake density	ρ_f	1027.6	kg/m^3
Fluid intake velocity	U_f	1.0-6.0	m/s

Model parameters			
Added mass coefficient	C_a	1	-
Element length	Δz	25	m
Drag coefficient	$\hat{C}_{x0}^{0}$	1.1856	-
Lift coefficient	$\hat{C}_{y1}^{0}$	0.3842	-
Strouhal number	St	0.1932	-
Tuning parameter	ε	0.7	-
Tuning parameter	A	12	-
Wake oscillator amplitude	q_1	2	-
Current parameters			
Type		Uniform	
Magnitude	V_c	0.4	m/s

Summary of results

From the results in Appendix B.7, the main conclusion that can be drawn is that the inflow velocity does not pose a great influence on the pipe's VIV response. For each inflow velocity that was evaluated the pipe sheds in the fourth mode, which means that the natural frequencies of the system do not shift much as the inflow velocity increases. Furthermore, all the values for the other outputs remain in more or less the same range.

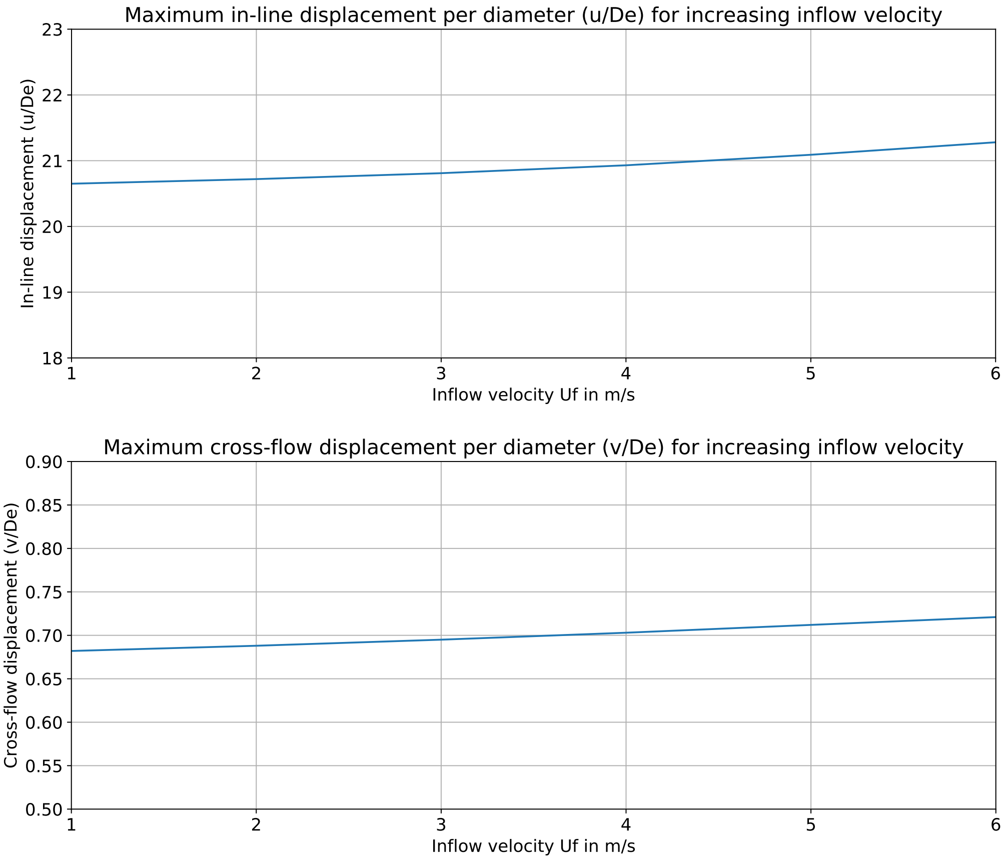

Figure 5.18: Overview of maximum in-line displacement per diameter (top) and the maximum cross-flow displacement per diameter (bottom) for increasing inflow velocity

Fig. 5.18 shows the maximum in-line and cross-flow displacement per diameter for the pipe with each different inflow velocity that has been evaluated. It can be seen from these graphs that the maximum displacements grow slightly with an increasing inflow velocity. This can be accredited to the stiffness and damping terms, as will be elaborated upon in Chapter 6. However, it seems that the pipe tension is in this case the dominant term, as the displacements only increase a tiny amount, whereas the inflow velocity increases rapidly. Since the pipe will shed in the same mode in all the evaluated instances there are no big jumps in displacement amplitude.

The maximum normal stress as percentage of yield stress can be found in Fig. 5.19. As can be seen, the maximum normal stress remains more or less the same for each inflow velocity. As the displacement amplitudes increase slightly, the bending stress will increase as well, but the axial tension will decrease due to the friction term, making the principal stress around 26% for each inflow velocity. This means the pipe will always remain safe in terms of normal stress.

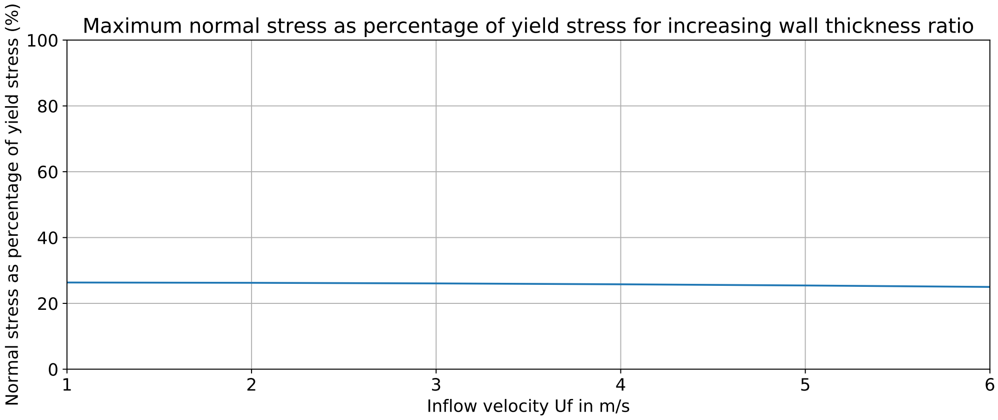

Figure 5.19: Overview of maximum normal stress as compared to yield stress of HDPE for increasing inflow velocity

In terms of fatigue damage per year, the level will increase with the inflow velocity due to the increase in bending stress amplitude due to the larger displacements. This effect is not dramatic though, and the fatigue damage does not seem to be a problem as it will remain very low. A summary of the discussed results is given in Tab. 5.17. The full table of outputs can be found in Appendix B.7.

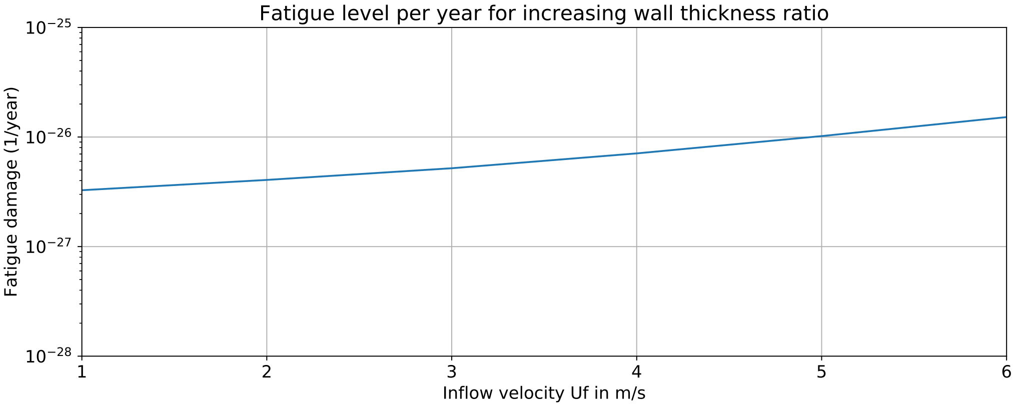

Figure 5.20: Overview of fatigue damage per year for increasing inflow velocity

Conclusion

The conclusion that can be drawn from this section is that the inflow velocity of the cold sea water through the pipe does not have a very significant influence on the VIV response of the pipe. A high inflow velocity does lead to a small increase in displacement amplitudes, but it is found that the principal stress doesn't increase as compared to the yield stress. It can therefore be assumed that high inflow velocities will lead to other problems that are outside the scope of this thesis, such as flow instability, pipe instability or pump capacity restrictions, before it becomes a problem in terms of VIV response.

Table 5.17: Summary of outputs for cold water pipe with different inflow velocities

Inflow velocity (m/s)	**1.0**	**2.0**	**3.0**	**4.0**	**5.0**	**6.0**
Max. u/D_e	20.65	20.72	20.81	20.93	21.09	21.28
Max. v/D_e	0.682	0.688	0.695	0.703	0.712	0.721
Max. σ as % of σ_y	26.3	26.3	26.1	25.8	25.4	25.0
D per year	3.27E-27	4.06E-27	5.19E-27	7.09E-27	1.02E-26	1.52E-26

5.8. Current velocity

In the analyses performed up to this point, the current velocity was always kept at a certain set velocity (0.2 m/s to simulate a more or less realistic situation or 0.4 m/s to invoke a larger VIV response in order to evaluate characteristics). Current velocity is however the most significant variable in VIV as it is directly related to vortex shedding through for example the Reynolds number and the Strouhal number. In general, a higher current velocity leads to a higher shedding frequency and it might even lead to lock-in with a higher mode if the current grows enough. In this section, the typical HDPE cold water pipe of 2.5 m diameter, 1000 m of length with a ballast mass of 350 tonnes, is once again subjected to a uniform current velocity, ranging from 0.1 m/s to 0.8 m/s. This range has been chosen because for lower velocities VIV will barely show in a pipe this size, and for higher velocities the drag will become a problem before VIV will, as can be concluded later from the values presented in this section. Finally, the pipe response will be evaluated when subjected to a sheared current flow ranging from 0.7 m/s (top) to 0.2 m/s (bottom) to simulate a realistic current profile at the possible location of an OTEC plant in Curaçao [6].

Uniform

This first is dedicated to the pipe subjected to several uniform flow velocities. The pipe and model parameters can be found in Tab. 5.18.

Table 5.18: Pipe parameters and model parameters for HDPE pipe with uniform current velocity

Pipe parameters			
Material		HDPE	
Length	L	1000	m
Outer diameter	D_e	2.5	m
Wall thickness	t	0.15	m
Pipe material density	ρ_p	950	kg/m^3
Young's modulus	E	$0.7056 \cdot 10^9$	N/m^2
Gravitational constant	g	9.81	m/s^2
Ballast mass	m_{bw}	$350 \cdot 10^3$	kg
Seawater and fluid parameters			
Sea water density	ρ_w	1026.6	kg/m^3
Fluid intake density	ρ_f	1027.6	kg/m^3
Fluid intake velocity	U_f	2.3	m/s

Model parameters			
Added mass coefficient	C_a	1	-
Element length	Δz	25	m
Drag coefficient	$\hat{C}^0_{x0}$	1.1856	-
Lift coefficient	$\hat{C}^0_{y1}$	0.3842	-
Strouhal number	St	0.1932	-
Tuning parameter	ε	0.7	-
Tuning parameter	A	12	-
Wake oscillator amplitude	q_1	2	-
Current parameters			
Type		Uniform	
Magnitude	V_c	0.1-0.8	m/s

Summary of results

From the results in Appendix B.8, the main conclusion that can be drawn is that the current velocity has a very significant impact on the VIV response of the pipe, as was predicted. The states of cross-flow displacement for the pipe in every evaluated current velocity are shown in order to illustrate the difference in shedding modes and displacement amplitudes.

The maximum in-line and cross-flow displacement of the pipe per diameter are shown in Fig. 5.21. The graphs show no real peculiarities. The in-line displacement will increase exponentially as the current velocity increases, due to the drag force being quadratically related to the current velocity. The in-line displacement

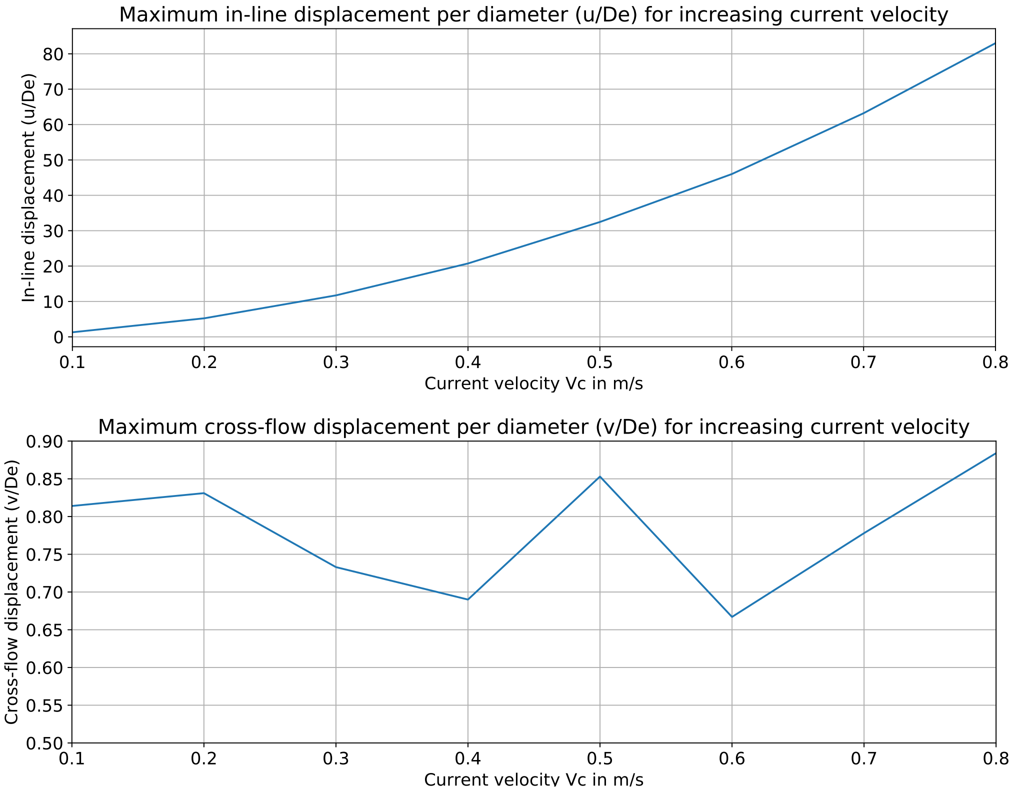

Figure 5.21: Overview of maximum in-line displacement per diameter (top) and the maximum cross-flow displacement per diameter (bottom) for increasing current velocity

per diameter varies, which is caused by the pipe shedding in different modes for every velocity. It can however be seen that for the pipe shedding in the same mode (mode six for $0.6 \leq V_c \leq 0.8$ m/s) the displacement amplitude increases for a higher current velocity.

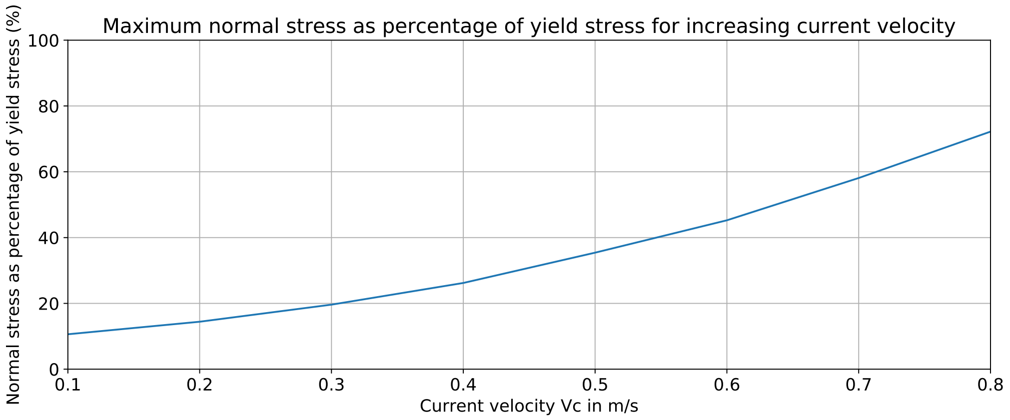

Figure 5.22: Overview of maximum normal stress as compared to yield stress of HDPE for increasing current velocity

The maximum normal stress as compared to the yield stress for the pipe evaluated with each current velocity can be found in Fig. 5.22. As can be seen, this graph has the same shape as the graph for the in-line displacement. This is no coincidence, since from the complete tables of outputs it can be found that the in-line bending displacement is the main contribution to the total principal stress, meaning that the large drag displacement will lead to the yielding of the material before the cross-flow bending stress caused by VIV. This is the main reason that current velocities greater than 0.8 m/s have not been evaluated, since the drag force

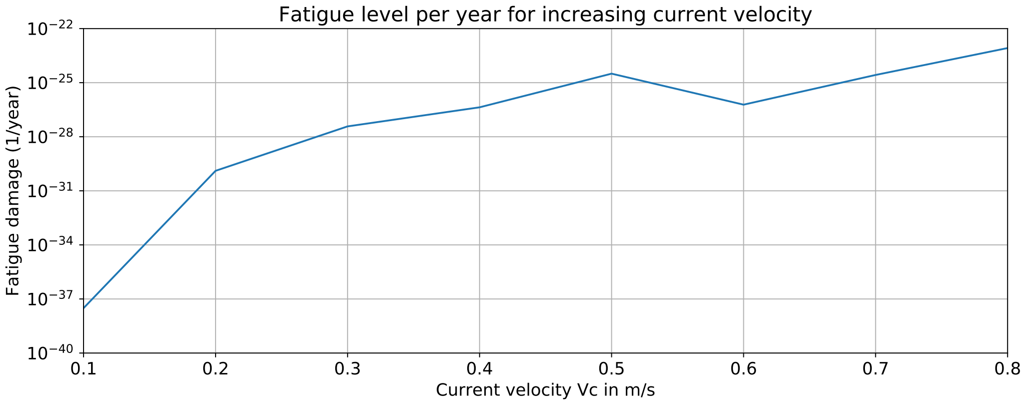

Figure 5.23: Overview of fatigue damage per year for increasing current velocity

has to be considered here before VIV, and thus this is without the scope of this thesis. For more on the drag in the cold water pipe, the work of Acevedo et al. [6] might be consulted. If the current velocity stays at a medium to low magnitude, the pipe will suffer no problems in terms of normal stress.

Fig. 5.23 shows the fatigue damage per year for the pipe with each evaluated current velocity. It can be concluded that in general the fatigue will increase as the current velocity increases, due to higher shedding frequencies and larger displacement amplitudes. A small dip in the curve can be found around $V_c = 0.6$ m/s which can be attributed to the fact that the pipe switches to a different mode here, leading to a drop in displacement amplitude. The most important conclusion is however that even for a relatively high current velocity of 0.8 m/s the fatigue is still not at a critical level. Therefore the claim made before might be considered valid, and the in-line bending stress will show problematic before cross-flow bending stress due to VIV does. A summary of the discussed results is given in Tab. 5.19.

Table 5.19: Summary of outputs for cold water pipe with different current velocities

Current velocity (m/s)	**0.1**	**0.2**	**0.3**	**0.4**	**0.5**	**0.6**	**0.7**	**0.8**
Max. u/D_e	1.29	5.24	11.73	20.74	32.46	46.00	63.21	83.01
Max. v/D_e	0.814	0.831	0.733	0.690	0.853	0.667	0.778	0.884
Max. σ as % of σ_y	10.6	14.4	19.6	26.2	35.4	45.3	58.1	72.2
D per year	3.11E-38	1.29E-30	3.76E-28	4.30E-27	3.17E-25	6.03E-27	2.68E-25	8.33E-24

Sheared

A visualisation of the sheared current profile can be recalled from Fig. 4.1. The current profile over the depth is derived from ocean data, and is defined as:

$$V_c(z) = 0.5 * e^{-0.003z} + 0.2 \quad , \tag{5.2}$$

which means that at the top of the pipe the current will have a magnitude of 0.7 m/s to then exponentially decline towards around 0.2 m/s. The pipe and model parameters stay the same. Fig. 5.24 shows the states of the cross-flow displacement of the pipe when subjected to the sheared current profile. It can be concluded that the vortex shedding will lock-in at fourth mode. However, there is also a lot of energy in other modes, as can be found from the frequency density spectrum in Fig. 5.25.

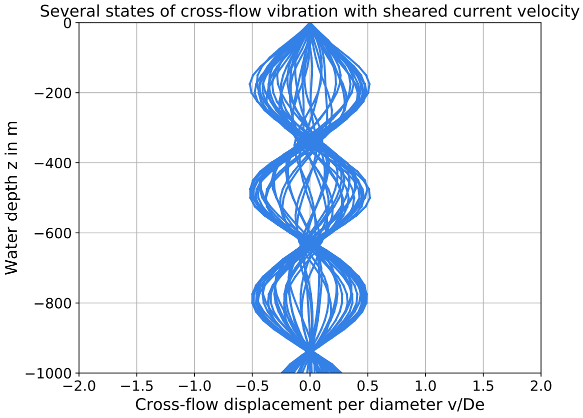

Figure 5.24: Several snapshots of the state of the cross-flow vibration of the pipe divided by the diameter when subjected to a sheared velocity profile

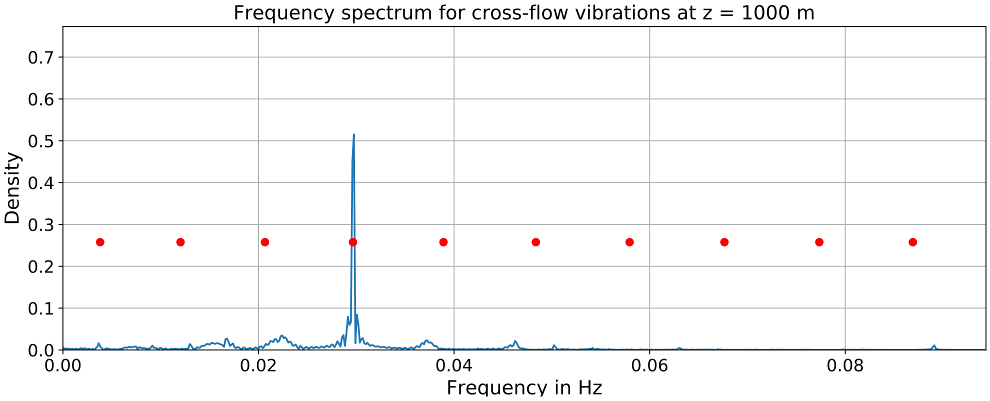

Figure 5.25: Frequency density spectrum for the given model run (natural frequencies depicted with red dots)

Summary of results

What can be concluded from the figures given here and the outputs in Appendix B.8, is that with a realistic current profile, the occurrence of VIV is very probable. The pipe in the given set-up will lock-in in the fourth mode with this current profile and the pipe will show a more or less regular VIV response. A summary of the outputs can be found in Tab. 5.20.

Table 5.20: Summary of outputs for cold water pipe with sheared current velocity profile

Current velocity (m/s)	**0.7 (top) - 0.2 (bottom)**
Max. u/D_e	11.35
Max. v/D_e	0.620
Max. σ as % of σ_y	21.8
D per year	1.41E-28

Conclusion

The conclusion of this subsection is that the current velocity has a very large influence on the VIV response of the cold water pipe. The shedding mode will change as will the displacement amplitudes, and thus the forces and stresses when the current velocity increases or decreases. However, it seems that HDPE has sufficient fatigue resistance to withstand the impact by VIV. A larger concern seems to be the yielding of the material due to drag at higher current velocities. In case of a realistic current profile that is based on locational ocean data, VIV will occur as well. The displacements and stresses will not grow to critical magnitudes and the fatigue damage will remain well in the acceptable range.

6

Analysis of stability in pipe conveying fluid with varying inflow velocity

Many different solutions have been proposed in order to suppress VIV in offshore marine structures of which several have been listed in Chapter 2. These measures all come with their own advantages and disadvantages, and literature is widely available. This chapter is dedicated to a measure that might be worth investigating, but has not been researched intensively yet. This research consists of checking whether the VIV can be suppressed by varying the inflow velocity of the fluid that is conveyed in the pipe. To do this, the equation of motion of a cantilever beam will be defined with a varying inflow velocity. This system will then be evaluated through modal analysis, in order to see whether there is a frequency that will give this system a stable nature. This is done using Floquet theory for periodic differential equations. If a certain inflow frequency can be found that makes this a stable system, it means that this frequency can be used to damp the vibrations and therefore might be of use for suppressing VIV.

6.1. Governing equations

The pipe model that will be analysed here is a result of the same assumptions made in Chapter 3. The figures presented in that chapter are representative for this model as well. It is decided to omit the terms for wall pressure difference and longitudinal tension, since varying the inflow velocity will have a minimal effect on these terms. This means that the terms that remain form essentially the equation for a cantilever beam conveying fluid. Since the aim of this research is contributing to an idea for suppressing cross-flow vibration, and as well to avoid confusion with inflow velocity U_f, the cross-flow displacement v is used in this chapter, however due to the symmetrical nature of this pipe it can be rewritten for in-line displacements by just changing v to u. Furthermore, free vibration is considered for now. For the sake of readability, derivatives with respect to location z are denoted by primes ($'$) and derivatives with respect to time t are denoted by dots ($\dot{}$). The equation of motion of transverse vibrations in a pipe conveying fluid with time-dependent velocity is given by for example Öz and Boyaci [41] as (with direction for U_f as defined in Chapter 3):

$$EIv'''' + m_{tot}\ddot{v} + m_f\left(U_f^2 v'' - 2U_f\dot{v}' - \dot{U}_f v'\right) = 0 \quad , \tag{6.1}$$

where $v = v(z,t)$ is the cross-flow displacement of the pipe, $U_f = U_f(t)$ is the time dependent inflow velocity, E is the Young's modulus of the pipe material, I is the moment of inertia of the pipe, and $m_{tot} = m_p + m_f + m_a = \rho_p A_p + \rho_f A_i + C_a\rho_w A_e$ is the total mass per unit length of the pipe. As can be seen, this equation is the standard equation for an Euler-Bernoulli beam with an extra term for the fluid that is being conveyed through the pipe.

6.2. Modal analysis

The idea of the modal analysis is to represent the displacement of the system as a superposition of the normal modes, multiplied by unknown functions of time. The normal mode shapes $\phi(z)$ for a cantilever beam without time dependent part are used as trial functions. Therefore, a solution of Eq. (6.1) can be found in the form:

$$v(z,t)=\sum_{n=1}^{\infty}\phi_n(z)q_n(t) \quad , \tag{6.2}$$

where $\phi_n(z)$ is the displacement amplitude for the nth normal mode and $q_n(t)$ is an unknown function of time. Substituting this into the equation of motion of Eq. (6.1) gives:

$$EI\sum_{n=1}^{\infty}\phi_n''''q_n+m_{tot}\sum_{n=1}^{\infty}\phi_n\ddot{q}_n+m_f\left(U_f^2\sum_{n=1}^{\infty}\phi_n''q_n-2U_f\sum_{n=1}^{\infty}\phi_n'\dot{q}_n-\dot{U}_f\sum_{n=1}^{\infty}\phi_n'q_n\right)=0 \quad , \tag{6.3}$$

where $\phi_n=\phi_n(z)$ and $q_n=q_n(t)$. The equation for a cantilever beam can be rewritten to:

$$EIv''''-m_{tot}\omega_n^2v=0 \quad , \tag{6.4}$$

and thus:

$$EIv''''=m_{tot}\omega_n^2v \quad . \tag{6.5}$$

It is assumed that this is also valid for this system, which means substituting Eq. (6.4) into Eq. (6.3) yields:

$$m_{tot}\sum_{n=1}^{\infty}\phi_n\left(\ddot{q}_n+\omega_n^2q_n\right)+m_f\left(U_f^2\sum_{n=1}^{\infty}\phi_n''q_n-2U_f\sum_{n=1}^{\infty}\phi_n'\dot{q}_n-\dot{U}_f\sum_{n=1}^{\infty}\phi_n'q_n\right)=0 \quad . \tag{6.6}$$

The normal mode displacements $\phi_n(z)$ have the property that they are orthogonal, which means that:

$$\int_0^L\phi_m\phi_n dz=0 \quad \text{for} \quad m\neq n \quad . \tag{6.7}$$

Eq. (6.6) is multiplied by $\phi_m(z)$ and integrated over the length from z=0 to z=L. With the orthogonality property defined in Eq. (6.7), the equation becomes:

$$\begin{gathered}Q_m m_{tot}\left(\ddot{q}_m+\omega_m^2q_m\right)+m_fU_f^2\sum_{n=1}^{\infty}q_n\int_0^L\phi_m\phi_n''dz-2m_fUf\sum_{n=1}^{\infty}\dot{q}_n\int_0^L\phi_m\phi_n'dz\\-m_f\dot{U}_f\sum_{n=1}^{\infty}q_n\int_0^L\phi_m\phi_n'dz=0 \quad ,\end{gathered} \tag{6.8}$$

where $Q_m=\int_0^L\phi_m^2dz$.

6.3. One-mode approximation

In order to model the dynamic behaviour of the pipe conveying a fluid with time varying inflow velocity, multiple modes will have to be considered. Since this is a large and computationally heavy process, it is decided to go for a simplified method due to time constraints. Therefore, the one-mode approximation will be used in order to evaluate the system. If low inflow velocities are considered, Eq. (6.1) can be simplified to:

$$EIv''''+m_{tot}\ddot{v}+m_fU_f^2v''=0 \quad , \tag{6.9}$$

which means two terms are omitted. This is reasonable to assume and necessary to obtain meaningful results from the one-mode approximation. Only the first mode is considered, and with $m=1$ Eq. (6.8) reduces to:

$$Q_1m_{tot}\left(\ddot{q}_1+\omega_1^2q_1\right)+m_fU_f^2q_1\int_0^L\phi_1\phi_1''dz=0 \quad , \tag{6.10}$$

This equation can be rewritten to a SDOF-system now:

$$M_{11}^*\ddot{q}_1+K_{11}^*(t)q=0 \quad . \tag{6.11}$$

It can be recalled that $U_f=U_f(t)$ is the time dependent inflow velocity. Therefore the first mode mass coefficient M_{11}^* and the time dependent first mode stiffness coefficient $K_{11}^*(t)$ are defined as:

$$\begin{cases}M_{11}^*=Q_1m_{tot}\\ \\ K_{11}^*(t)=Q_1m_{tot}\omega_1^2+m_fU_f(t)^2\int_0^L\phi_1\phi_1''dz\end{cases} \quad . \tag{6.12}$$

The first normal mode shape of a cantilever beam can be used here to approximate the values for $\phi_1(z)$, and it is defined in the form of [42]:

$$\phi_1(z) = \frac{\cosh\beta_1 z - \cos\beta_1 z}{\cosh\beta_1 L + \cos\beta_1 L} - \frac{\sinh\beta_1 z - \sin\beta_1 z}{\sinh\beta_1 L + \sin\beta_1 L} \quad , \tag{6.13}$$

where β_1 is dependent on the properties of the system and its natural frequency. For the first mode of a cantilever beam $\beta_1 L \approx 1.875$. Using this, the values for the integral of ϕ_1, ϕ_1' and ϕ_1'' can be determined by using a program as for example Maple. This means that all the values in Eq. (6.12) are known and the system can be evaluated for a certain function $U_f(t)$. The function $U_f(t)$ can for example be defined as:

$$U_f(t) = U_{f0}\left(1 + \sin(\omega_f t)\right) \quad , \tag{6.14}$$

where U_{f0} is the amplitude of inflow velocity and ω_f is the frequency of change of the inflow velocity. In words, this means that the inflow velocity will vary sinusoidally from 0 m/s to $2U_{f0}$ m/s (since this means that the pipe will at all times keep pumping up the water) at a frequency of ω_f rad/s. Therefore, the coefficient $K_{11}^*(t)$ as defined in Eq. (6.12) is periodic with a time period $T = \frac{2\pi}{\omega_f}$. Therefore, the stability of the system can be analysed using Floquet theory.

6.4. Floquet theory

Floquet theory can be applied as a method for dealing with the stability of a system of first order ODEs with periodic coefficients. It is applicable on any system that can be written in the form:

$$\underline{\dot{x}}(t) = \underline{\underline{A}}(t) \cdot \underline{x}(t) \quad , \tag{6.15}$$

where $\underline{\underline{A}}(t)$ is an $(n \times n)$-matrix. For the sake of analysing this system a new quantity is introduced. The state transition matrix $\underline{\underline{\Phi}}(t, t_0)$ is defined as:

$$\underline{\underline{\Phi}}(t, t_0) = \underline{\underline{U}}(t) \cdot \underline{\underline{U}}^{-1}(t_0) \quad , \tag{6.16}$$

where $\underline{\underline{U}}(t)$ is the fundamental solution matrix, which contains n linearly independent solutions to the ODE defined in Eq. (6.15). It is defined as $\underline{\underline{U}}(t) = \left[\underline{x}_1(t), \underline{x}_2(t), ..., \underline{x}_n(t)\right]$ where $\underline{x}_i(t)$ is a vector containing the ith solution to Eq. (6.15). The initial condition for the state transition matrix is defined as:

$$\underline{\underline{\Phi}}(0,0) = \mathrm{I}_n \quad , \tag{6.17}$$

where I_n is the $n \times n$ identity matrix. The definition of the fundamental matrix $\underline{\underline{U}}$ means that:

$$\underline{\underline{\dot{U}}}(t) = A(t) \cdot \underline{\underline{U}}(t) \quad , \tag{6.18}$$

which leads to the definition for the state transition matrix:

$$\underline{\underline{\dot{\Phi}}}(t,0) = A(t) \cdot \underline{\underline{\Phi}}(t,0) \quad \text{for} \quad t_0 = 0 \quad . \tag{6.19}$$

Using the Floquet Theorem and the Lyapunov Reducibility Theorem, it can be shown that the stability criterion for this system is reached if the eigenvalues of the transition matrix at the end of one period are lower than 1. This is explained extensively in, for example, the work of Brugmans [43], and will not completely be written out here. Therefore:

$$(\mathrm{Re}\,\lambda_i)^2 + (\mathrm{Im}\,\lambda_i)^2 < 1 \quad , \tag{6.20}$$

where λ_i are the eigenvalues of $\underline{\underline{\Phi}}(T,0)$, the state transition matrix at the end of time period T. The stability of the system with a certain inflow frequency ω_f is found by numerically integrating Eq. (6.19) over a time period $T = 2\pi/\omega_f$ with initial condition $\underline{\underline{\Phi}}(0,0) = \mathrm{I}_n$, using for example Python's *odeint* as has been done before. If one of the eigenvalues of $\underline{\underline{\Phi}}(T,0)$ is above 1, per Eq. 6.20 the system is unstable. If a combination of U_{f0} and ω_f is found for which the system is stable, it means that the displacement v following from Eq. (6.9) approaches zero as time approaches infinity and a suppression of the displacement is achieved.

6.5. Results of one-mode approximation

To apply Floquet theory on this system, the second order ODE of Eq. (6.11) has to be rewritten into the form of Eq. (6.15). This is done by defining:

$$\begin{aligned} x_1(t) &= q_1(t) \quad , \\ x_2(t) &= \dot{q}_1(t) \quad , \end{aligned} \tag{6.21}$$

and Eq. (6.15) will become:

$$\begin{bmatrix} \dot{x}_1(t) \\ \dot{x}_2(t) \end{bmatrix} = \begin{bmatrix} 0 & 1 \\ -\frac{K_{11}^*(t)}{M_{11}*} & 0 \end{bmatrix} \cdot \begin{bmatrix} x_1(t) \\ x_2(t) \quad , \end{bmatrix} \tag{6.22}$$

so the time dependent matrix $A(t)$ is:

$$A(t) = \begin{bmatrix} 0 & 1 \\ -\frac{K_{11}^*(t)}{M_{11}*} & 0 \end{bmatrix} \quad , \tag{6.23}$$

where all the coefficients have been determined in the previous sections. Choosing a large array of values for U_{f0} and ω_f, the system that has to be evaluated is defined as:

$$\dot{\underline{\underline{\Phi}}}(t,0) = A(t) \cdot \underline{\underline{\Phi}}(t,0) \quad . \tag{6.24}$$

Time dependent matrix $A(t)$ is defined in Eq. (6.23) and the initial condition is $\underline{\underline{\Phi}}(0,0) = \mathrm{I}_2$. Python's *odeint* is used to integrate the system numerically over $t = 0$ to $t = T = 2\pi/\omega_f$ in order to obtain $\underline{\underline{\Phi}}(T,0)$. After this, the eigenvalues of $\underline{\underline{\Phi}}(T,0)$ are computed and checked whether or not they exceed 1. If one of the eigenvalues exceeds 1 (which means the system is unstable), a red dot is plotted. If none of the eigenvalues exceeds 1 (which means the system is stable), a green dot is plotted. This is done in order to quickly establish the combination of U_{f0} and ω_f that will lead to a stable system. The pipe that will be considered here is a steel pipe of 1000 m length with a diameter of 2.5 m, in order to remain in the order of magnitudes of OTEC. The complete overview of the used parameters and some numerically determined values can be found in Appendix D. Since this assumptions that were made are only valid for relatively low inflow velocities, the considered inflow velocity amplitudes U_{f0} range from 0 to 0.5 m/s, and since the natural frequency of the mode that is considered is low at $\omega_1 = 0.011$ rad/s, the considered inflow velocity frequency ω_f ranges from 0 to 2.0 rad/s. The results of this analysis can be found in Fig. 6.1.

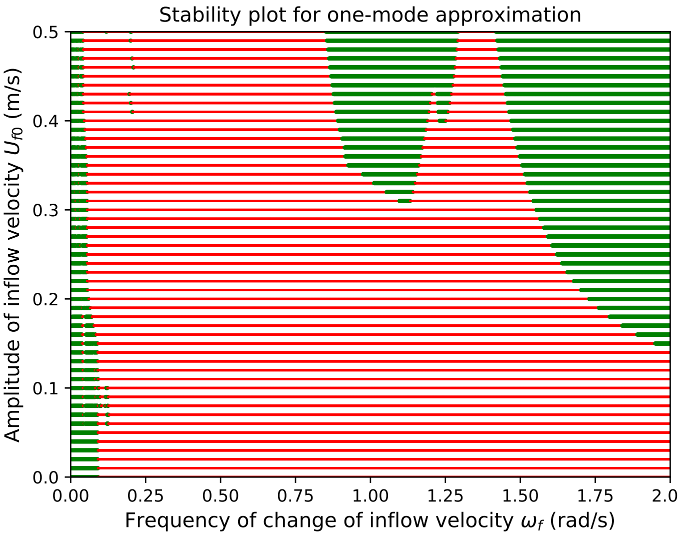

Figure 6.1: Stability plot for the pipe using the one-mode approximation for different combinations of U_{f0} and ω_f. Combinations that yield a stable value plotted in green, combinations that yield an unstable value plotted in red.

The figure does show some peculiarities. For very low frequencies, the pipe model always seems to be stable. This is very unlikely since a very low frequency means a nearly constant flow velocity.This might have to do with numerical inaccuracies such as truncation of values, the solver not being able to converge properly, etcetera. Therefore, the left part of the figure should be treated with care. The right part of the chart shows a more typical stability plot, and it can be seen that there are certain regions for which the system will remain stable. The first range can be approximately described as the range where $1.00 < \omega_f < 1.10$ rad/s and $U_{f0} > 0.35$, and the second range where $\omega_f > 1.60$ and $U_{f0} > 0.25$. This means that for values in this range, the displacement defined in Eq. (6.15) will approach zero as time approaches infinity. Once agan however, note that this is only a very rough approximation. Furthermore, the ranges seem to extend far beyond the evaluated array of values, but since the inflow frequency is already very large compared to the natural frequency at $\omega_f = 2.0$ and the assumptions that were made are only valid for low inflow velocities, it has to be questioned how relevant extending this plot into a larger range of input values is.

6.6. Conclusion and further study

In this chapter, a general idea was given of how Floquet theory can be used to evaluate the stability of a pipe conveying fluid with a time varying inflow velocity. Unfortunately, due to time constraints, this was only done in a simplified way using just one mode to approximate the behaviour of the pipe, and therefore the results are highly questionable. In order to perform this analysis properly, the system defined in Eq. (6.8) should be evaluated for multiple modes. This means that there will be coupling terms between all the modes and the matrix $A(t)$ will have a size of $(2m \times 2m)$, where m is the amount of modes that are considered, and the rest of the procedure will remain the same. If enough modes are considered, the dynamical behaviour of the pipe as defined in Eq. (6.1) should be simulated sufficiently accurate, and a frequency and amplitude should be found for which the system is stable. Theoretically, the same procedure can be used to find a frequency and amplitude that would grant stability to a pipe subject to vortex-induced vibrations. This would be done by instead of applying free vibration conditions, applying the VIV forcing terms as defined in Section 3.5 (possibly linearisation of some terms is necessary). Furthermore, there would be three degrees of freedom instead of one, to wit $u(t)$, $v(t)$ and $q(t)$, which would lead to a set of six first order coupled ODEs if rewritten properly, for each mode that is considered. Therefore, the total amount of coupled equations that would have to be solved would be $6m$, where m is the amount of modes considered, making $A(t)$ a $(6m \times 6m)$ matrix. Once again, the rest of the procedure will remain the same and theoretically a combination of values could be found that makes the system stable.

7

Conclusion and recommendations

This chapter contains the final conclusions of this research and provides some recommendations. The recommendations contain advise on how to handle VIV in OTEC, which follows directly from the conclusions, and advise on how to proceed from this study and improve the research to gain a more complete knowledge of VIV in OTEC.

7.1. Conclusions

Since the procedure of modelling this pipe was quite straightforward and has been performed many times, the most interesting conclusions from this thesis come from the numerical simulations of the cold water pipe subjected to a current flow. A list of the most significant conclusions is given below:

- The best material for an OTEC cold water pipe in terms of VIV resistance is HDPE. Due to its lightness and lack of stiffness the forces and stresses will always remain at a very low level compared to pipes in other materials like steel and FRP. What this means is that the pipe will not have problems with yielding, will barely suffer from fatigue and can be assumed to have a long life expectancy.

- Pipes with diameters as large as up to 6.0 m do not seem to suffer too much from VIV. Although a larger diameter does lead to higher fatigue damage per year, the fatigue damage will always remain rather insignificant. Therefore it can be assumed that as long as a pipe in a certain diameter can be realised, it can also be used for OTEC in terms of VIV resistance.

- It is worthwhile to tension the pipe with a ballast mass as heavy as realistically possible. A large ballast mass at the bottom of the pipe will severely suppress VIV, and the positive effect of VIV suppression is relatively large compared to the negative effect a large ballast mass has on the normal stress. Since HDPE is relatively strong compared to its lightness, the fatigue damage per year decreases more rapidly than the normal stress increases.

- The magnitude of the inflow velocity does not have a significant impact on the VIV. Keeping the inflow stable at high velocities in a large diameter will prove more of a challenge than the impact on VIV.

- A higher current velocity has a severe impact on the magnitude and frequency of the response of the pipe. As the current gets very high however, VIV does not seem to be the largest problem any more. The bending stress in the top of the pipe will become critically large due to the in-line displacement of the pipe caused by the increased drag force. It might therefore be wise to consider prioritising this over VIV.

- It is very likely that VIV will occur in real life OTEC plants, based on the location specific current profile that was used to check the influence of a sheared current profile. However, it does not seem likely that VIV will be problematic, if the right combination of material and pipe properties is used.

The conclusion of the final chapter concerning the stability of a pipe conveying fluid at a variable velocity is that there most likely is a frequency at which the system is stable, which might mean that the research can be extended in order to apply this knowledge on a pipe model with VIV response.

7.2. Recommendations

This section will contain the recommendations that follow from this research and its conclusions. It will start of with the recommendations regarding how to handle VIV in the cold water pipe of an OTEC plant, and after that the recommendations on how to improve this research are given.

Recommendations regarding VIV in a cold water pipe

As follows from the conclusions, the most important attribute of a pipe is its material. Since HDPE seems to be the only reasonable choice for a pipe of this length and size, it can be assumed that this will be the material of choice. This means that the other variables do not matter too much, as this research has shown that the fatigue damage per year will always remain relatively insignificant assuming that the researched variables stay within reasonable range. Several things can be done however to make the resistance of the pipe to VIV even better and they are listed here:

- As mentioned before, the ideal cold water pipe would be made out of HDPE, since it has by far the best fatigue resistance, along with its other perks concerning installation and production.
- The pipe would benefit greatly from a large ballast mass at its end, since it suppresses the VIV response significantly without increasing the normal stress to a critical range.
- The pipe showed to have a significant in-line bending stress when subjected to high current flows. This can be attributed to the fact that the pipe in this research was a clamped cantilever beam, which leads to a very high rotation angle and curvature in the top of the pipe. Therefore, other boundary conditions could be considered, like for example a joint in the top, which would mean the pipe could rotate freely, relieving the bending stress. Furthermore, the pipe could be fixed to the bottom to make sure the in-line vibration remains small.

Recommendations regarding this research

Although one always strives for perfection, this research is far from perfect. This is due to time constraints, computational limits and inadequate knowledge of all the specifics concerning the theory behind this research. It should therefore never be used as a defining document and always be treated with utmost care. It might however serve as a base for whoever wants to continue this research. Below, several recommendations are listed that might be used to improve this research. Note that this is only a fraction of the possible improvements, as a model can never be accurate enough.

- As the OTEC cold water pipe has unusual large diameter, the fluid will flow at unusual high Reynolds numbers. As the Strouhal number for vortex-shedding in the usual Reynolds regimes is defined at roughly 0.2, which has been used all throughout this research, it is less strictly defined at higher Reynolds numbers. Therefore, the model might become more accurate if the Strouhal number is considered more carefully with regards to the higher Reynolds flow regimes.
- Throughout this research, the lower branch approximation for the wake oscillator parameters have been used, since this is done in most of the studied literature. For extra accuracy however, it might also be of interest to model the pipe with the upper branch parameters.
- For a more complete overview, the pipe could be modelled with multiple different boundary conditions, in order to quantify their influence on the VIV response. Furthermore, the bottom boundary condition might be expanded to include the effect of the inflow velocity of the conveyed fluid.
- In order to get a more accurate feeling of the different fatigue levels of pipes in different materials, a closer look has to be taken at the fatigue models with which they were checked. In this research, for each material the fatigue model had a different form, which means they might differ in terms of definition. Furthermore, a very conservative estimate of the maximum stresses in the pipe was made in this research. For a more accurate the check the maximum principal stress in the pipe as result of normal stress, in-line bending stress and cross-flow bending stress has to be calculated more accurately.
- For a more realistic overview of VIV, a more detailed location specific current profile could be implemented. This current profile could also include variations in angle over depth, as well as variations over time.

Bibliography

[1] The White House. Remarks by the President at U.N. Climate Change Summit, September 2014. URL `https://obamawhitehouse.archives.gov/the-press-office/2014/09/23/remarks-president-un-climate-change-summit`.

[2] J. Cook, N. Oreskes, P. T. Doran, W. R. L. Anderegg, B. Verheggen, E. W. Maibach, S. J. Carlton, S. Lewandowsky, A. G. Skuce, S. A. Green, D. Nuccitelli, P. Jacobs, M. Richardson, B. Winkler, R. Painting, and K. Rice. Consensus on consensus: a synthesis of consensus estimates on human-caused global warming. *Environmental Research Letters*, 11(4):048002, 2016.

[3] REN21. Renewables 2016 Global Status Report, 2016.

[4] K. Rajagopalan and G. C. Nihous. An Assessment of Global Ocean Thermal Energy Conversion Resources With a High-Resolution Ocean General Circulation Model. *Journal of Energy Resources Technology*, 135: 041202, 2013.

[5] Bluerise. Ocean Thermal Energy Conversion – OTEC. URL `http://www.bluerise.nl/technology/ocean-thermal-energy-conversion/`.

[6] D. Acevedo, R. Blokker, P. Dinnissen, J. Kirkenier, and B. J. Kleute. General arrangement of a 10MW offshore OTEC plant, April 2015.

[7] New Scientist. 20,000 megawatts under the sea: Oceanic steam engines, February 2014. URL `https://www.newscientist.com/article/mg22129580-900-20000-megawatts-under-the-sea-oceanic-steam-engines/`.

[8] J.P. Rafferty and J.L. Mero. Ocean thermal energy conversion (OTEC). URL `https://www.britannica.com/technology/ocean-thermal-energy-conversion#ref1120916`.

[9] Power from the Sea. *Popular Mechanics Magazine*, 54(6):881–882, 1930.

[10] S.M. Masutani and P.K. Takahashi. Ocean Thermal Energy Conversion (OTEC), 2001.

[11] M.M. Takahashi, K. Kitazawa, and P. Snowden. *Deep Ocean Water as Our Next Natural Resource*. Terra Scientific Publishing Company, 2000.

[12] K.A. Finney. Ocean Thermal Energy Conversion. *Guelph Engineering Journal*, 1:17–23, 2008.

[13] J. Daly. Hawaii About to Crack Ocean Thermal Energy Conversion Roadblocks?, December 2011. URL `https://oilprice.com/Alternative-Energy/Renewable-Energy/Hawaii-About-To-Crack-Ocean-Thermal-Energy-Conversion-Roadblocks.html`.

[14] R. D. Blevins. *Flow-Induced Vibration*. Van Nostrand Reinhold, 1977.

[15] J.H. Lienhard. Synopsis of Lift, Drag, and Vortex Frequency Data for Rigid Circular Cylinders, 1966.

[16] C.H.K. Williamson and R. Govardhan. A brief review of recent results in vortex-induced vibrations. *Journal of Wind Engineering and Industrial Aerodynamics*, 96:713–735, 2008.

[17] R. D. Gabbai and H. Benaroya. An overview of modeling and experiments of vortex-induced vibration of circular cylinders. *Journal of Sound and Vibration*, 282:575–616, 2005.

[18] P. W. Bearman. Vortex shedding from oscillating bluff bodies. *Annual Review of Fluid Mechanics*, 16: 195–222, 1984.

[19] T. Sarpkaya. Fluid forces on oscillating cylinders. *Journal of Waterway, Port, Coastal and Ocean Engineering*, 104:275–290, 1978.

[20] O. M. Griffin and G. H. Koopmann. The vortex-excited lift and reaction forces on resonantly vibrating cylinders. *Journal of Sound and Vibration*, 54:435–448, 1977.

[21] M. L. Facchinetti, E. De Langre, and F. Biolley. Coupling of structure and wake oscillators in vortex-induced vibrations. *Journal of Fluids and Structures*, 19:123–140, 2004.

[22] R.H.M. Ogink and A. V. Metrikine. A wake oscillator with frequency dependent coupling for the modeling of vortex-induced vibration. *Journal of Sound and Vibration*, 329:5452–5473, 2010.

[23] C.H.K. Williamson and A. Roshko. Vortex formation in the wake of an oscillating cylinder. *Journal of Fluids and Structures*, 2:355–381, 1988.

[24] T. Sarpkaya. A critical review of the intrinsic nature of vortex-induced vibrations. *Journal of Fluids and Structures*, 19:389–447, 2004.

[25] M.M. Zdravkovich. Review and classification of various aerodynamic and hydrodynamic means for suppressing vortex shedding. *Journal of Wind Engineering and Industrial Aerodynamics*, 7:145–189, 1981.

[26] S. Huang. VIV suppression of a two-degree-of-freedom circular cylinder and drag reduction of a fixed circular cylinder by the use of helical grooves. *Journal of Fluids and Structures*, 27:1124–1133, 2011.

[27] M. Khorasanchi and S. Huang. Instability analysis of deepwater riser with fairings. *Ocean Engineering*, 79:26–34, 2014.

[28] Y. Yu, F. Xie, H. Yan, Y. Constantinides, O. Oakley, and G. E. Karniadakis. Suppression of vortex-induced vibrations by fairings: A numerical study. *Journal of Fluids and Structures*, 54:679–700, 2015.

[29] S.T. Slocum, Z.J. Ding, W. R. Frank, and M.R. Cox. Flutter Instability in Riser Fairings. In *Offshore Technology Conference*, number 16342, Houston, Texas, U.S.A., May 2004.

[30] M. P. Païdoussis and G. X. Li. Pipes conveying fluid: a model dynamical problem. *Journal of Fluids and Structures*, 7:137–204, 1993.

[31] G.L. Kuiper. *Stability of Offshore Risers Conveying Fluid.* PhD thesis, Delft University of Technology, January 2008.

[32] S. Rao. *Mechanical Vibrations.* Prentice Hall, 5th edition, 2011.

[33] G.S. Baarholm, C.M. Larsen, and H. Lie. On fatigue damage accumulation from in-line and cross-flow vortex-induced vibrations. *Journal of Fluids and Structures*, 22:109–127, 2006.

[34] P.C.J. Hoogenboom and R. Spaan. Shear Stiffness and Maximum Shear Stress of Tubular Members. In *The Fifteenth International Offshore and Polar Engineering Conference*, Seoul, Korea, June 2005.

[35] ASTM E1049-85. Standard Practices for Cycle Counting in Fatigue Analysis. Technical report, American Society for Testing and Materials, 2017.

[36] N-004. Design of Steel Structures. Technical report, NORSOK, December 1998.

[37] W. Hwang and K.S. Han. Fatigue of Composites - Fatigue Modulus Concept and Life Prediction. *Journal of Composite Materials*, 20:154–165, March 1986.

[38] M. Bourchak and A. Aid. PE-HD fatigue damage accumulation under variable loading based on various damage models. *eXPRESS Polymer Letters*, 11(2):117–126, 2017.

[39] A.D. Trim, H. Braaten, H. Lie, and M.A. Tognarelli. Experimental investigation of vortex-induced vibration of long marine risers. *Journal of Fluids and Structures*, 21:335–361, 2005.

[40] J.B. Wanderley and C. Levi. Vortex induced loads on marine risers. *Ocean Engineering*, 32:1281–1295, 2005.

[41] H.R. Öz and H. Boyaci. Transverse vibrations of tensioned pipes conveying fluid with time-dependent velocity. *Journal of Sound and Vibration*, 236(2):259–276, 2000.

[42] J.M.J. Spijkers, A.W.C.M. Vrouwenvelder, and E.C. Klaver. *Structural Dynamics Part 1 - Structural Vibrations.* Delft University of Technology, 2005.

[43] J. Brugmans. Parametric Instability of Deep-Water Risers. Master's thesis, Delft University of Technology, Delft, the Netherlands, 2005.

[44] R. Courant, K. Friedrichs, and H. Lewy. On the Partial Difference Equations of Mathematical Physics. *IBM Journal of Research and Development*, 11(2):215, 1967.

[45] DNV-RP-F204. Riser Fatigue. Technical report, Det Norske Veritas, October 2010.

A

Software implementation of model

All the equations that are used for this model are defined in Chapters 3 and 4. These are coupled higher order partial differential equations (PDEs), turned into second order ordinary differential equations (ODEs) by discretising them in the z-direction. However, in order to use the numerical integration method *odeint* of the Python *scipy.integrate*-package, they have to be turned in a set of first order ODEs. This Appendix is therefore dedicated to showing the software implementation of this model.

A.1. Rewriting system to first order ODEs and solution matrix

As mentioned before, the numerical integration method of Python will only work for a set of ordinary differential equations, thus the set of second order ODEs has to be rewritten. Since this process has exactly the same form for every node, it will only be explained for one single node. Every node has three equations to be solved, one for the x-direction, one for the y-direction and one for the wake variable q. Therefore, the set of coupled second order ODEs that has to be solved at a certain time step for a node in the middle of the pipe reads as:

$$\begin{aligned}
&M_1\frac{\partial^2 u_j}{\partial t^2} + K_1\left(u_{j+2}-4u_{j+1}+6u_j-4u_{j-1}+u_{j-2}\right)+K_2\left(u_{j+1}-2u_j+u_{j-1}\right)\\
&+C_1\left(\frac{\partial u_{j+1}}{\partial t}-\frac{\partial u_{j-1}}{\partial t}\right)+K_3\left(u_{j+1}-u_{j-1}\right)=\frac{1}{2}\rho_w D_e V_c^2 C_{VX}-\frac{1}{4}D_e^2\rho_w C_a\frac{\partial^2 u_j}{\partial t^2} \quad ,\\
&M_1\frac{\partial^2 v_j}{\partial t^2} + K_1\left(v_{j+2}-4v_{j+1}+6v_j-4v_{j-1}+v_{j-2}\right)+K_2\left(v_{j+1}-2v_j+v_{j-1}\right)\\
&+C_1\left(\frac{\partial v_{j+1}}{\partial t}-\frac{\partial v_{j-1}}{\partial t}\right)+K_3\left(v_{j+1}-v_{j-1}\right)=\frac{1}{2}\rho_w D_e V_c^2 C_{VY}-\frac{1}{4}D_e^2\rho_w C_a\frac{\partial^2 v_j}{\partial t^2} \quad ,\\
&\frac{\partial^2 q_j}{\partial t^2}+\varepsilon\omega_s(q_j^2-1)\frac{\partial q_j}{\partial t}+\omega_s^2 q_j=\frac{A}{D_e}\left(\frac{\partial^2 v_j}{\partial t^2}\cos(\theta_{cur})-\frac{\partial^2 u_j}{\partial t^2}\sin(\theta_{cur})\right) \quad .
\end{aligned} \tag{A.1}$$

In order to solve this system for every node using *odeint*, it has to be rewritten to a system of first order ODEs where the derivative of the variable that has to be calculated is the only term on the left-hand side of the equation. To do this, the help-variables U, V and Q are introduced. These variables are solely introduced for the purpose of illustrating how the model is implemented in the software. Therefore, the system of Eq. (A.1) will become:

$$
\begin{aligned}
\frac{\partial u_j}{\partial t} &= U_j \quad , \\
\frac{\partial U_j}{\partial t} &= \frac{1}{M_1+\frac{1}{4}D_e^2\rho_w C_a}\Big(\frac{1}{2}\rho_w D_e V_c^2 C_{VX} - K_1\left(u_{j+2}-4u_{j+1}+6u_j-4u_{j-1}+u_{j-2}\right) \\
&\quad -K_2\left(u_{j+1}-2u_j+u_{j-1}\right)-C_1\left(U_{j+1}-U_{j-1}\right)-K_3\left(u_{j+1}-u_{j-1}\right)\Big) \quad , \\
\\
\frac{\partial v_j}{\partial t} &= V_j \quad , \\
\frac{\partial V_j}{\partial t} &= \frac{1}{M_1+\frac{1}{4}D_e^2\rho_w C_a}\Big(\frac{1}{2}\rho_w D_e V_c^2 C_{VY} - K_1\left(v_{j+2}-4v_{j+1}+6v_j-4v_{j-1}+v_{j-2}\right) \\
&\quad -K_2\left(v_{j+1}-2v_j+v_{j-1}\right)-C_1\left(V_{j+1}-V_{j-1}\right)-K_3\left(v_{j+1}-v_{j-1}\right)\Big) \quad , \\
\\
\frac{\partial q_j}{\partial t} &= Q_j \quad , \\
\frac{\partial Q_j}{\partial t} &= \frac{A}{D_e}\left(\frac{\partial V_j}{\partial t}\cos\left(\theta_{cur}\right)-\frac{\partial U_j}{\partial t}\sin\left(\theta_{cur}\right)\right)-\varepsilon\omega_s(q_j^2-1)Q_j-\omega_s^2 q_j \quad .
\end{aligned}
\tag{A.2}
$$

This means that for every node, six ODEs have to be solved. They are being integrated numerically by the *odeint*-function, and all the solutions are stored in matrix-form. For every node the solver produces six outcomes. The matrix with solutions will therefore have a width $6\cdot N$ entries, where N is the number of nodes of the system. Since the *odeint*-function will integrate the system until a certain accuracy and produces outputs at every time step, the matrix will have a height of $t=\frac{T}{dt}$ where T is the total simulation time and dt is the length of the time step. To illustrate, the solution matrix will have the following form (where for example $u_{j,i}$ means u at the jth node and the ith time step) on the top left part:

$$
\begin{bmatrix}
\overbrace{u_{1,1} \quad U_{1,1} \quad v_{1,1} \quad V_{1,1} \quad q_{1,1} \quad Q_{1,1}}^{\text{node 1}} & \overbrace{u_{2,1} \quad U_{2,1} \quad v_{2,1} \quad V_{2,1} \quad q_{2,1} \quad Q_{2,1}}^{\text{node 2}} & \cdots \\
u_{1,2} \quad U_{1,2} \quad v_{1,2} \quad V_{1,2} \quad q_{1,2} \quad Q_{1,2} & u_{2,2} \quad U_{2,2} \quad v_{2,2} \quad V_{2,2} \quad q_{2,2} \quad Q_{2,2} & \cdots \\
\vdots \quad \vdots \quad \vdots \quad \vdots \quad \vdots \quad \vdots & \vdots \quad \vdots \quad \vdots \quad \vdots \quad \vdots \quad \vdots & \ddots
\end{bmatrix} \quad .
\tag{A.3}
$$

On the bottom right part the matrix will have the following form:

$$
\begin{bmatrix}
\ddots & \vdots \quad \vdots \quad \vdots \quad \vdots \quad \vdots \quad \vdots \\
\cdots & u_{N,i-1} \quad U_{N,t-1} \quad v_{N,t-1} \quad V_{N,t-1} \quad q_{N,t-1} \quad Q_{N,t-1} \\
\cdots & \underbrace{u_{N,t} \quad U_{N,t} \quad v_{N,t} \quad V_{N,t} \quad q_{N,t} \quad Q_{N,t}}_{\text{node N}}
\end{bmatrix} \quad .
\tag{A.4}
$$

The complete solution matrix will have the following form:

$$
t \text{ rows}\left\{\begin{bmatrix}
\overbrace{\cdots \quad \cdots \quad \cdots}^{6\cdot N \text{ columns}} \\
\cdots \quad \cdots \quad \cdots \\
\cdots \quad \cdots \quad \cdots
\end{bmatrix}\right. \quad .
\tag{A.5}
$$

Understanding the way the solution matrix is formed makes it easy to find all the relevant displacements, which can then be used for further processing. This software implementation of the model is easily changeable for multiple variables, making it useful for calculating forces, moments, stresses and performing analyses of multiple scenarios.

A.2. Time steps and element length considering stability

Due to computational limitations, the grid in this thesis will be relatively coarse. Element length will vary between 25 and 50 meters, and time steps will be in the order of 0.1 or 0.01 seconds. Therefore it is important to check whether the stability of this model is still intact. In order to check whether this model will converge, the Courant-Friedrichs-Lewy (CFL) condition can be checked. More about the CFL condition can be found in the work of Courant et al. [44]. The CFL condition is defined as:

$$C = \frac{u\Delta t}{\Delta x} \leq C_{max} \quad , \tag{A.6}$$

where u is the magnitude of the velocity, Δt is the magnitude of the time interval, Δx is the magnitude of the length interval and C_{max}. It can be assumed that no values above $u = 2$ m/s will be evaluated, and therefore in worst case scenario with $\Delta t = 0.1$ s and $\Delta x = 25$ m the CFL condition will be $C = 0.008$. It can be therefore assumed that stability is always preserved in this model.

Furthermore, the time step should be small enough for the solver to produce results that completely visualise the nature of the oscillation. It can be assumed that 16 points will be enough to capture an entire oscillation. The highest frequencies will have the shortest oscillation period, which means that the time step should be at least:

$$\Delta t \leq \frac{T_{min}}{16} = \frac{1}{16 f_{max}} \quad , \tag{A.7}$$

where T_{min} is the minimum occurring vibration period and f_{max} is the corresponding maximum occurring frequency. If it is once again assumed that no values above $u = 2$ m/s will be evaluated and that the diameters evaluated will not be smaller than $D_e = 2$ m, then the maximum occurring shedding frequency from Eq. (2.2) will be $f_{max} = 0.2$ Hz. This means that the time step should never be bigger than $\Delta t = 0.3125$ s. Therefore, the chosen maximum of $\Delta t = 0.1$ s proves more than sufficient to capture all the characteristics of the VIV in this pipe.

B

Analysis results

This Appendix contains all the model results that were deemed redundant for the main matter of the report, but can nonetheless be consulted in order to get a more in depth view in the outputs.

B.1. Typical riser

This section contains the full overview of the benchmark model run of Section 5.1 The model is run over a time period of 5000 s to make sure the equilibrium is reached. First, an overview of the first natural frequencies is given with the corresponding current velocity that might cause shedding in said mode.

Table B.1: Natural frequencies and corresponding current velocities

Mode number	**Nat. freq. in rad/s**	**Nat. freq. in Hz**	**Current velocity in m/s**
1	0.080	0.013	0.017
2	0.184	0.029	0.038
3	0.289	0.046	0.060
4	0.398	0.063	0.082
5	0.513	0.082	0.106
6	0.634	0.101	0.131
7	0.758	0.121	0.156
8	0.885	0.141	0.182
9	1.013	0.161	0.209
10	1.142	0.182	0.235

Fig. B.1 and Fig. B.2 show the in-line vibration over time and the cross-flow vibration over time respectively. With these displacements the formulas listed in Section 4.4 can be used to calculate the other outputs. An algorithm is used to find the maximum value of each output in time along the pipe, since those will be the defining values. All the calculated outputs can be found in Tab. B.2.

Table B.2: Relevant outputs of the model for the typical riser

Output		**Minimum**	**Maximum**	**Unit**
Moment in x-direction	M_x	$-0.393 \cdot 10^3$	$12.93 \cdot 10^3$	Nm
Moment in y-direction	M_y	$-3.891 \cdot 10^3$	$3.891 \cdot 10^3$	Nm
Shear force x-direction	$F_{s,x}$	-93.58	58.21	N
Shear force y-direction	$F_{s,y}$	-253.7	253.7	N
Bending stress in x-direction	$\sigma_{z,IL}$	$-6.415 \cdot 10^6$	$21.05 \cdot 10^6$	N/m^2
Bending stress in y-direction	$\sigma_{z,CF}$	$-6.336 \cdot 10^6$	$6.336 \cdot 10^6$	N/m^2
Shear-stress in x-direction	τ_x	$-17.40 \cdot 10^3$	$10.83 \cdot 10^3$	N/m^2
Shear-stress in y-direction	τ_y	$-47.19 \cdot 10^3$	$47.20 \cdot 10^3$	N/m^2

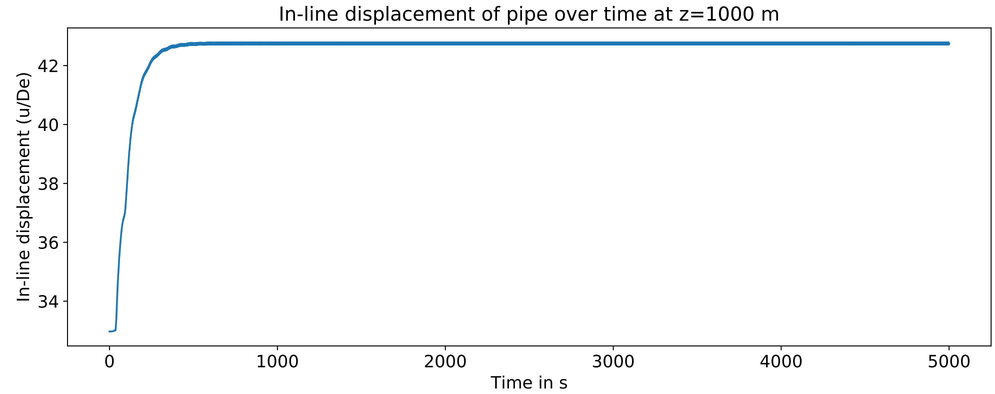

Figure B.1: In-line displacement per diameter of pipe over time

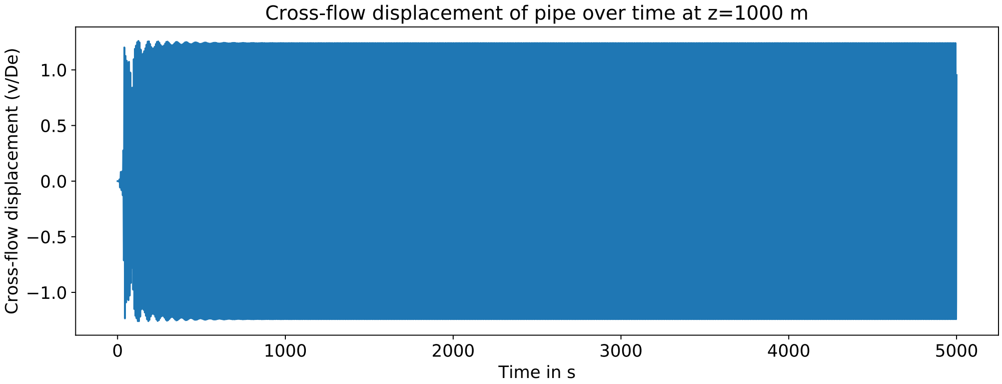

Figure B.2: Cross-flow displacement per diameter of pipe over time

With all the obtained outputs, a fatigue analysis can be performed. According to DNV-RP-F204 [45], for the fatigue damage calculation of a riser the cyclic principal stress has to be considered. For the most conservative estimate, at each node the stress cycle in in-flow and cross-flow direction is added together and an algorithm is used to determine the node with the largest stress cycle. This stress cycle is then used in the formula Eq. (4.40). Since this is a steel pipe, the SN-curve from Eq. (4.41) is valid here and can be used. From N-004 [36] it can be found that for a steel marine riser $\log a = 11.687$ and $m = 3$. Using a rainflow-counting method, the fatigue damage for this pipe can be found as $D = 0.0192$ per year.

B.2. Typical cold water pipe

This section contains the full overview of the cold water pipe model run of Section 5.2 An overview of the first natural frequencies is given with the corresponding current velocity that might cause shedding in said mode.

Table B.3: Natural frequencies and corresponding current velocities

Mode number	**Nat. freq. in rad/s**	**Nat. freq. in Hz**	**Current velocity in m/s**	**Mode number**	**Nat. freq. in rad/s**	**Nat. freq. in Hz**	**Current velocity in m/s**
1	0.024	0.004	0.049	6	0.304	0.048	0.626
2	0.076	0.012	0.156	7	0.364	0.058	0.750
3	0.130	0.021	0.267	8	0.425	0.068	0.875
4	0.186	0.030	0.384	9	0.486	0.077	1.001
5	0.245	0.039	0.504	10	0.546	0.087	1.125

Fig. B.3 and Fig. B.4 show the in-line vibration over time and the cross-flow vibration over time respectively. With these displacements the other outputs can be calculated. All the calculated outputs can be found in Tab. B.4.

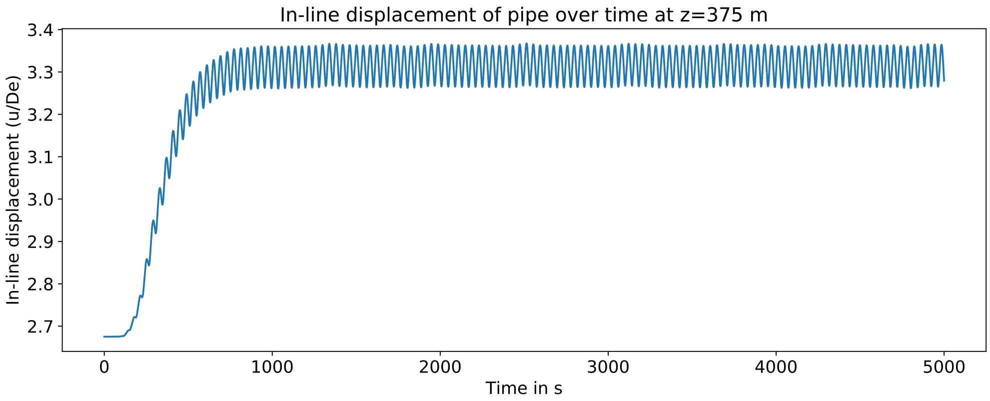

Figure B.3: In-line displacement per diameter of pipe over time

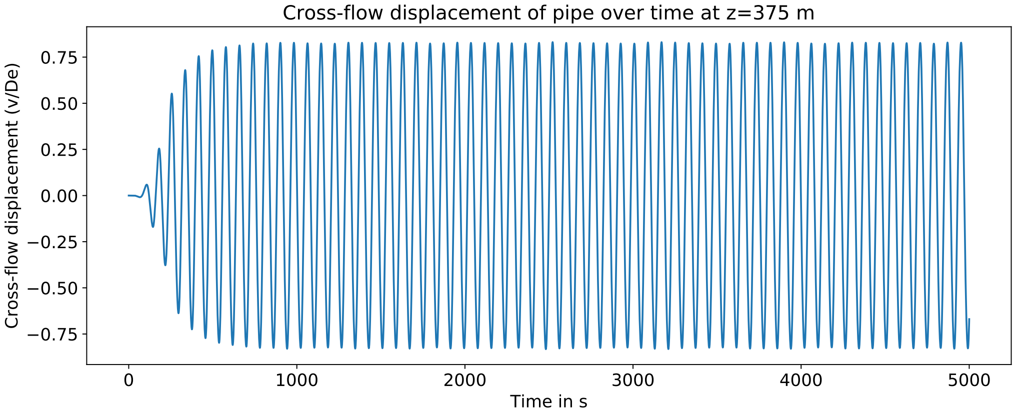

Figure B.4: Cross-flow displacement per diameter of pipe over time

Table B.4: Relevant outputs of the model for the typical cold water pipe

Output		**Minimum**	**Maximum**	**Unit**
Moment in x-direction	M_x	$-11.19\cdot10^3$	$585.5\cdot10^3$	Nm
Moment in y-direction	M_y	$-187.5\cdot10^3$	$187.8\cdot10^3$	Nm
Shear force x-direction	$F_{s,x}$	-3508	90.37	N
Shear force y-direction	$F_{s,y}$	-1201	1204	N
Bending stress in x-direction	$\sigma_{z,IL}$	$-0.182\cdot10^6$	$0.953\cdot10^6$	N/m^2
Bending stress in y-direction	$\sigma_{z,CF}$	$-0.305\cdot10^6$	$0.305\cdot10^6$	N/m^2
Shear-stress in x-direction	τ_x	$-6.525\cdot10^3$	$0.168\cdot10^3$	N/m^2
Shear-stress in y-direction	τ_y	$-2.235\cdot10^3$	$2.239\cdot10^3$	N/m^2

With all the obtained outputs, a fatigue analysis can be performed. Since this is a HDPE pipe, the SN-curve from Eq. (4.43) is valid here and can be used. From Bourchak and Aid [38] it can be found that for a HDPE pipe $A = 33.5$ and $b = -0.0728$. Using a rainflow-counting method, the fatigue damage for this pipe can be found as $D = 1.360\cdot10^{-30}$ per year.

B.3. Materials

This section contains the full overview of the model run that is done to visualise the differences in the use of material of Section 5.3 An overview of the first natural frequencies of the pipe in each separate material is given with the corresponding current velocity that might cause shedding in said mode.

Table B.5: Natural frequencies and corresponding current velocities

	Steel			**FRP**			**HDPE**		
Mode number	**Nat. freq. in rad/s**	**Nat. freq. in Hz**	**Current velocity in m/s**	**Nat. freq. in rad/s**	**Nat. freq. in Hz**	**Current velocity in m/s**	**Nat. freq. in rad/s**	**Nat. freq. in Hz**	**Current velocity in m/s**
1	0.076	0.012	0.156	0.038	0.006	0.079	0.024	0.004	0.049
2	0.192	0.031	0.396	0.110	0.018	0.227	0.076	0.012	0.156
3	0.364	0.058	0.751	0.159	0.025	0.327	0.130	0.021	0.267
4	0.551	0.088	1.135	0.203	0.032	0.418	0.186	0.030	0.384
5	0.556	0.089	1.146	0.314	0.050	0.646	0.245	0.039	0.504
6	0.586	0.093	1.207	0.426	0.068	0.878	0.304	0.048	0.626
7	0.818	0.130	1.685	0.443	0.071	0.913	0.364	0.058	0.750
8	0.855	0.136	1.760	0.592	0.094	1.220	0.425	0.068	0.875
9	1.119	0.178	2.304	0.711	0.113	1.464	0.486	0.077	1.001
10	1.131	0.180	2.330	0.737	0.117	1.518	0.546	0.087	1.125

Tab. B.6 lists all of the relevant outputs for the model run of the cold water pipe in different materials. The summary of the most important outputs can be found in Tab. 5.9.

Table B.6: Relevant outputs of the model for the pipe in different materials

Output steel		**Minimum**	**Maximum**	**Unit**
Moment in x-direction	M_x	$-0.378 \cdot 10^6$	$15.96 \cdot 10^6$	Nm
Moment in y-direction	M_y	$-15.62 \cdot 10^3$	$15.62 \cdot 10^3$	Nm
Shear force x-direction	$F_{s,x}$	$-11.21 \cdot 10^3$	$6.497 \cdot 10^3$	N
Shear force y-direction	$F_{s,y}$	$-107.5 \cdot 10^3$	$107.5 \cdot 10^3$	N
Bending stress in x-direction	$\sigma_{z,IL}$	$-0.616 \cdot 10^6$	$25.97 \cdot 10^6$	N/m^2
Bending stress in y-direction	$\sigma_{z,CF}$	$-25.43 \cdot 10^6$	$25.43 \cdot 10^6$	N/m^2
Shear-stress in x-direction	τ_x	$-208.6 \cdot 10^3$	$12.09 \cdot 10^3$	N/m^2
Shear-stress in y-direction	τ_y	$-200.0 \cdot 10^3$	$200.0 \cdot 10^3$	N/m^2
Output FRP		**Minimum**	**Maximum**	**Unit**
Moment in x-direction	M_x	$-469.7 \cdot 10^3$	$1286 \cdot 10^3$	Nm
Moment in y-direction	M_y	$-4.380 \cdot 10^6$	$4.416 \cdot 10^3$	Nm
Shear force x-direction	$F_{s,x}$	$-95.39 \cdot 10^3$	$8.601 \cdot 10^3$	N
Shear force y-direction	$F_{s,y}$	$-35.57 \cdot 10^3$	$35.73 \cdot 10^3$	N
Bending stress in x-direction	$\sigma_{z,IL}$	$0.765 \cdot 10^6$	$20.95 \cdot 10^6$	N/m^2
Bending stress in y-direction	$\sigma_{z,CF}$	$-7.133 \cdot 10^6$	$7.192 \cdot 10^6$	N/m^2
Shear-stress in x-direction	τ_x	$-177.4 \cdot 10^3$	$16.00 \cdot 10^3$	N/m^2
Shear-stress in y-direction	τ_y	$-66.17 \cdot 10^3$	$66.47 \cdot 10^3$	N/m^2
Output HDPE		**Minimum**	**Maximum**	**Unit**
Moment in x-direction	M_x	$-49.11 \cdot 10^3$	$2270 \cdot 10^3$	Nm
Moment in y-direction	M_y	$-360.8 \cdot 10^3$	$360.8 \cdot 10^3$	Nm
Shear force x-direction	$F_{s,x}$	$-13.84 \cdot 10^3$	$0.513 \cdot 10^3$	N
Shear force y-direction	$F_{s,y}$	$3.159 \cdot 10^3$	$3.159 \cdot 10^3$	N
Bending stress in x-direction	$\sigma_{z,IL}$	$-0.080 \cdot 10^6$	$3.697 \cdot 10^6$	N/m^2
Bending stress in y-direction	$\sigma_{z,CF}$	$-0.588 \cdot 10^6$	$0.588 \cdot 10^6$	N/m^2
Shear-stress in x-direction	τ_x	$-25.75 \cdot 10^3$	$0.954 \cdot 10^3$	N/m^2
Shear-stress in y-direction	τ_y	$-5.877 \cdot 10^3$	$5.877 \cdot 10^3$	N/m^2

With all the obtained outputs, a fatigue analysis can be performed. For the steel pipe, the FRP pipe and the HDPE pipe the SN-curves from Eqs. (4.41), (4.42) and (4.43) respectively. For the steel pipe, with $\log a = 11.687$ and $m = 3$, the fatigue damage per year will be $D = 0.005$. For the FRP pipe, it can be found from Hwang and Han [37] that $B = 10.33$ and $c = 0.14012$. Using a rainflow-counting method it can be found that for this pipe the fatigue damage per year will be $D = 0.060$. Finally, for the HDPE pipe using $A = 33.5$ and $b = -0.0728$ the fatigue damage per year can be found as $D = 4.37 \cdot 10^{-30}$.

B.4. Diameters

This section contains the full range of outputs of the research conducted in Section . It has to be noted that the outputs considered relevant for this study are listed in the corresponding section. Tab. B.7 contains all the outputs for the different diameters. Fig. B.5 shows an overview of the states of cross-flow vibrations of the pipe in several manually chosen diameters. The diameters that are chosen are 2.0 m, 4.0 m, 5.0 m and 6.0 m because these diameters give a clear overview of the transfer of shedding modes from fourth to third as the diameter increases.

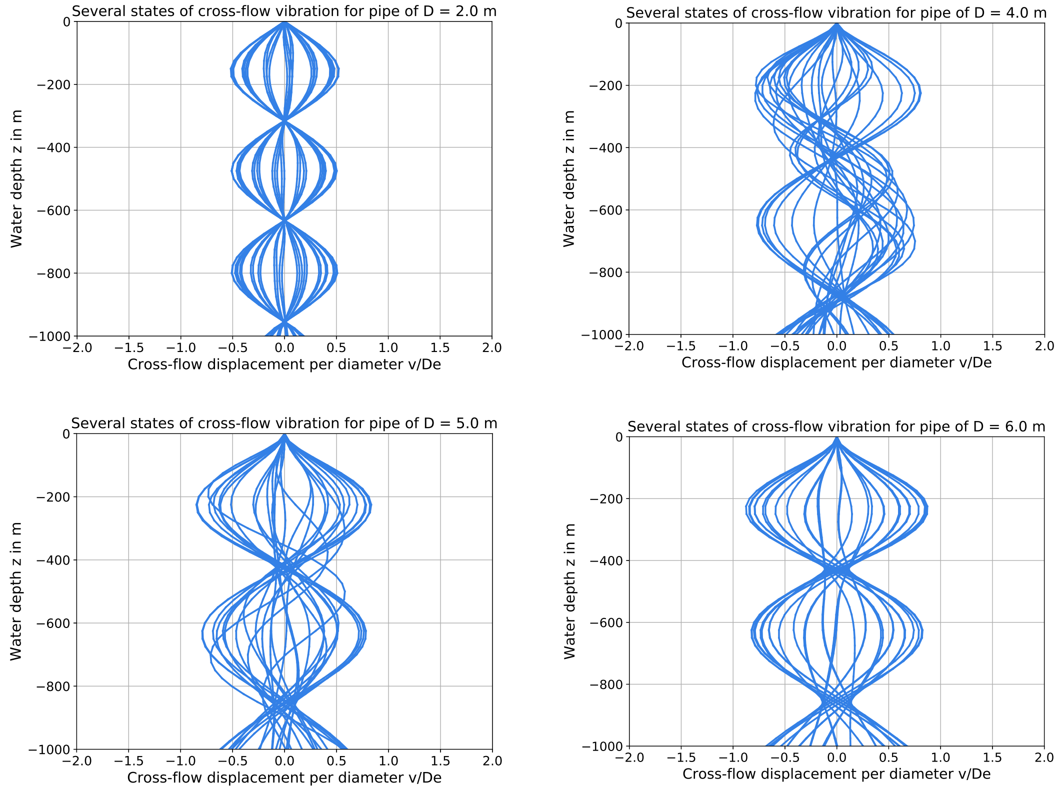

Several states of cross-flow vibration for pipe of D = 2.0 m

Several states of cross-flow vibration for pipe of D = 4.0 m

Several states of cross-flow vibration for pipe of D = 5.0 m

Several states of cross-flow vibration for pipe of D = 6.0 m

Figure B.5: States of cross-flow displacement of pipe in several diameters: 2.0 m (top left), 4.0 m (top right), 5.0 m (bottom left), 6.0 m (bottom right)

Table B.7: Complete list of outputs gathered from the VIV model with a HDPE pipe in different diameters

Diameter (m)	**2.0**	**2.5**	**3.0**	**3.5**	**4.0**	**4.5**	**5.0**	**5.5**	**6.0**
Shedding mode	4	3-4	3-4	3-4	3-4	3-4	3-4	3	3
Max. u/D_e	12.68	13.18	14.14	15.00	16.14	17.64	19.63	22.38	26.34
Max. v/D_e	0.564	0.625	0.799	0.821	0.821	0.834	0.853	0.869	0.878
Min. M_x (kNm)	-8.060	-26.16	-77.42	-189.2	-396.2	$-0.754\cdot10^{3}$	$-1.463\cdot10^{3}$	$-2.770\cdot10^{3}$	$-5.234\cdot10^{3}$
Max. M_x (kNm)	389.1	$1.251\cdot10^{3}$	$3.226\cdot10^{3}$	$6.908\cdot10^{3}$	$13.14\cdot10^{3}$	$23.04\cdot10^{3}$	$38.17\cdot10^{3}$	$61.23\cdot10^{3}$	$96.89\cdot10^{3}$
Min. M_y (kNm)	-77.39	-261.8	-697.6	$-1.449\cdot10^{3}$	$-2.742\cdot10^{3}$	$-4.633\cdot10^{3}$	$-7.472\cdot10^{3}$	$-11.15\cdot10^{3}$	$-15.09\cdot10^{3}$
Max. M_y (kNm)	76.34	261.2	696.6	$1.446\cdot10^{3}$	$2.734\cdot10^{3}$	$4.796\cdot10^{3}$	$7.656\cdot10^{3}$	$11.22\cdot10^{3}$	$14.80\cdot10^{3}$
Min. $F_{s,x}$ (kN)	-0.932	-5.625	-21.10	-54.13	-109.4	-188.8	-292.4	-416.4	-574.1
Max. $F_{s,x}$ (kN)	0.129	0.294	0.994	2.267	4.805	7.255	11.15	16.71	25.61
Min. $F_{s,y}$ (kN)	-0.620	-2.130	-56.65	-13.81	-29.12	-52.41	-82.29	-115.6	-139.7
Max. $F_{s,y}$ (kN)	0.620	2.104	5.704	13.84	29.11	50.74	81.59	116.5	147.0
Min. $\sigma_{z,IL}$ (MN/m^2)	-0.030	-0.050	-0.085	-0.131	-0.183	-0.245	-0.347	-0.493	-0.718
Max. $\sigma_{z,IL}$ (MN/m^2)	1.441	2.371	3.538	4.772	6.080	7.487	9.044	10.90	13.29
Min. $\sigma_{z,CF}$ (MN/m^2)	-0.287	-0.496	-0.765	-1.001	-1.269	-1.508	-1.770	-1.985	-2.069
Max. $\sigma_{z,CF}$ (MN/m^2)	0.283	0.495	0.764	0.999	1.265	1.559	1.814	1.998	2.029
Min. τ_x (KN/m^2)	-3.201	-12.36	-32.21	-60.71	-93.94	-128.1	-160.7	-189.1	-2.191
Max. τ_x (KN/m^2)	0.444	0.646	1.517	2.542	4.126	4.922	6.125	7.589	9.774
Min. τ_y (KN/m^2)	-2.128	-4.682	-8.647	-15.49	-25.01	-35.56	-45.22	-52.52	-53.32
Max. τ_y (KN/m^2)	2.131	4.626	8.706	15.52	24.99	34.424	44.83	52.91	56.09
Max. cycle $\Delta\sigma_i$ (MN/m^2)	0.107	0.081	0.229	0.408	0.511	0.665	0.820	0.978	1.148
Fatigue D (1/yr)	$4.78\cdot10^{-29}$	$2.95\cdot10^{-31}$	$3.79\cdot10^{-25}$	$4.91\cdot10^{-22}$	$4.82\cdot10^{-20}$	$1.61\cdot10^{-18}$	$2.68\cdot10^{-17}$	$2.66\cdot10^{-16}$	$2.27\cdot10^{-15}$

B.5. Wall thickness

This section contains the full range of outputs of the research conducted in Section 5.5. It has to be noted that the outputs considered relevant for this study are listed in the corresponding section. Tab. B.8 contains all the outputs for the different diameter to wall thickness ratios. Since all the pipes shed completely in the fourth mode there are no further figures to show.

Table B.8: Complete list of outputs gathered from the VIV model with a HDPE pipe with different diameter to wall thickness ratios

Diameter to wall thickness ratio (D_e/t)	**12**	**14**	**16**	**18**	**20**	**22**	**24**	**26**
Shedding mode	4	4	4	4	4	4	4	4
Max. u/D_e	22.17	21.42	20.89	20.48	20.17	19.91	19.70	19.53
Max. v/D_e	0.717	0.703	0.693	0.686	0.681	0.677	0.673	0.671
Min. M_x (kNm)	-74.49	-60.97	-51.62	-44.74	-39.48	-35.31	-31.93	-29.13
Max. M_x (kNm)	$3.152\cdot10^{3}$	$2.701\cdot10^{3}$	$2.365\cdot10^{3}$	$2.103\cdot10^{3}$	$1.893\cdot10^{3}$	$1.721\cdot10^{3}$	$1.578\cdot10^{3}$	$1.457\cdot10^{3}$
Min. M_y (kNm)	-482.6	-422.0	-374.4	-336.3	$-305.0\cdot10^{3}$	-279.1	-257.1	-238.4
Max. M_y (kNm)	482.6	422.0	374.4	336.3	$305.0\cdot10^{3}$	279.1	257.1	238.4
Min. $F_{s,x}$ (kN)	-22.04	-17.78	-14.69	-12.36	-10.59	-9.146	-8.002	-7.064
Max. $F_{s,x}$ (kN)	0.720	0.603	0.533	0.476	0.429	0.389	0.356	0.328
Min. $F_{s,y}$ (kN)	-4.702	-3.916	-3.325	-2.864	-2.497	-2.201	-1.959	-1.758
Max. $F_{s,y}$ (kN)	4.702	3.916	3.325	2.864	2.497	2.201	1.959	1.758
Min. $\sigma_{z,IL}$ (MN/m^2)	-0.094	-0.086	-0.081	-0.078	-0.075	-0.073	-0.071	-0.069
Max. $\sigma_{z,IL}$ (MN/m^2)	3.969	3.827	3.725	3.648	3.589	3.540	3.500	3.467
Min. $\sigma_{z,CF}$ (MN/m^2)	-0.607	-0.598	-0.590	-0.583	-0.578	-0.574	-0.570	-0.563
Max. $\sigma_{z,CF}$ (MN/m^2)	0.607	0.598	0.590	0.583	0.578	0.574	0.570	0.563
Min. τ_x (KN/m^2)	-30.61	-28.28	-26.33	-24.67	-23.23	-21.96	-20.84	-19.83
Max. τ_x (KN/m^2)	1.000	0.959	0.956	0.950	0.942	0.934	0.926	0.921
Min. τ_y (KN/m^2)	-6.531	-6.229	-5.962	-5.714	-5.489	-5.285	-5.108	-4.934
Max. τ_y (KN/m^2)	6.531	6.229	5.962	5.714	5.489	5.285	5.108	4.934
Max. cycle $\Delta\sigma_i$ (MN/m^2)	0.186	0.168	0.153	0.140	0.130	0.120	0.112	0.104
Fatigue D (1/yr)	$9.08\cdot10^{-26}$	$2.25\cdot10^{-26}$	$6.41\cdot10^{-27}$	$1.98\cdot10^{-27}$	$6.57\cdot10^{-28}$	$2.35\cdot10^{-28}$	$8.73\cdot10^{-29}$	$3.40\cdot10^{-29}$

B.6. Ballast mass

This section contains the full range of outputs of the research conducted in Section 5.6. It has to be noted that the outputs considered relevant for this study are listed in the corresponding section. Tab. B.9 contains all the outputs for the different ballast masses. Fig. B.6 shows the states of cross-flow vibrations for each pipe setup that has been evaluated.

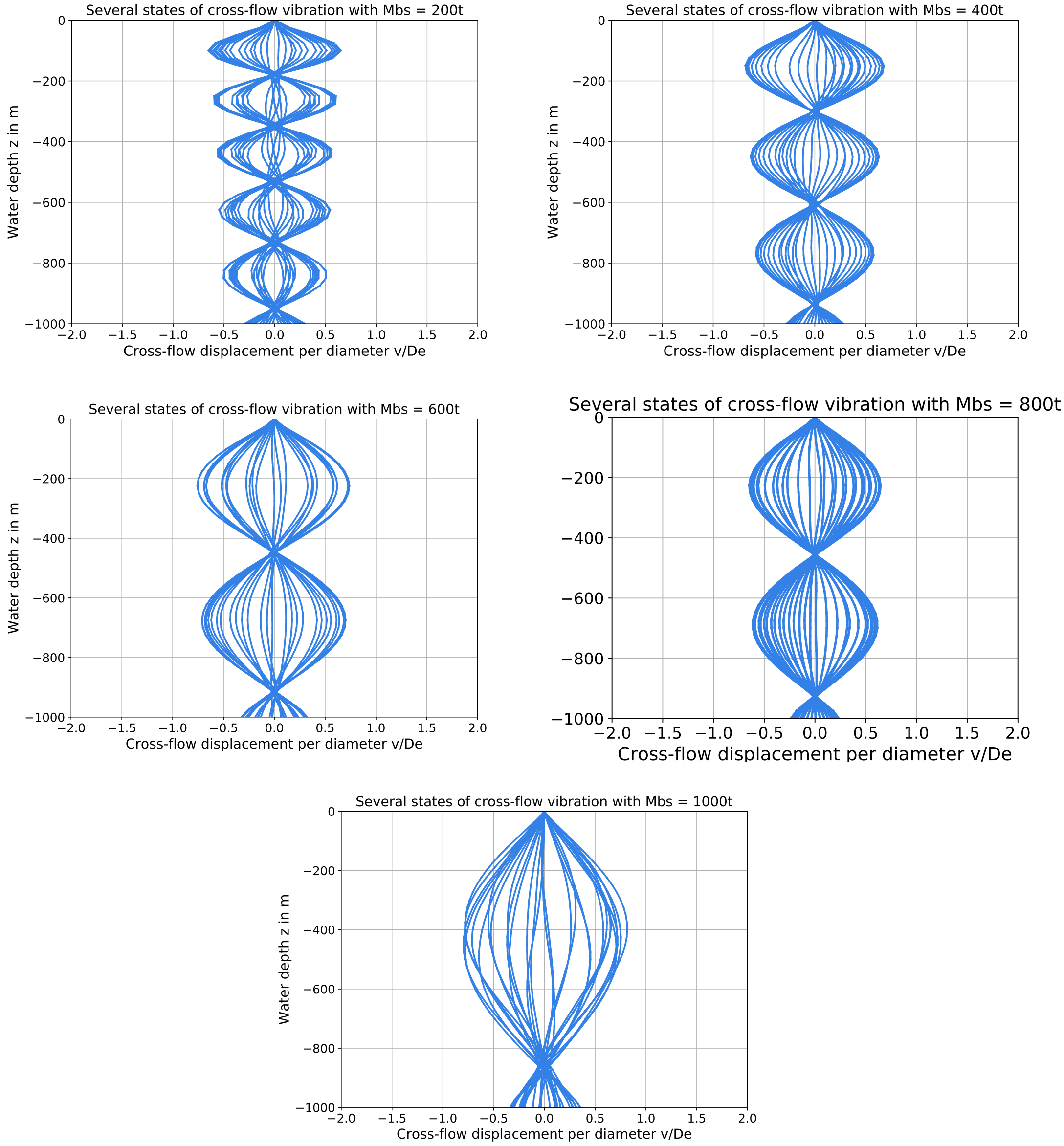

Figure B.6: States of cross-flow displacement of pipe tensioned with several ballast masses: $200 \cdot 10^3$ kg (top left), $400 \cdot 10^3$ kg (top right), $600 \cdot 10^3$ kg (centre left), $800 \cdot 10^3$ kg (centre right), $1000 \cdot 10^3$ kg (bottom)

Table B.9: Complete list of outputs gathered from the VIV model with a HDPE pipe with different ballast masses

Ballast mass (10^3 kg)	**200**	**400**	**600**	**800**	**1000**
Ballast mass compared to pipe mass	0.19	0.38	0.57	0.76	0.95
Shedding mode	6	4	3-4	2-3	2-3
Max. u/D_e	66.78	20.48	12.28	8.70	6.43
Max. v/D_e	0.654	0.685	0.757	0.755	0.833
Min. M_x (kNm)	-315.6	-58.03	-31.84	-18.88	-11.92
Max. M_x (kNm)	$7301 \cdot 10^3$	$2271 \cdot 10^3$	$1369 \cdot 10^3$	$967.8 \cdot 10^3$	718.1
Min. M_y (kNm)	-524.4	-358.2	-300.1	-239.2	-173.6
Max. M_y (kNm)	524.4	358.2	304.7	235.9	174.0
Min. $F_{s,x}$ (kN)	-65.54	-16.97	-8.279	-4.917	3.105
Max. $F_{s,x}$ (kN)	3.222	0.541	0.375	0.172	0.120
Min. $F_{s,y}$ (kN)	-9.536	-3.688	-2.370	-1.443	-1.263
Max. $F_{s,y}$ (kN)	9.536	3.688	2.251	1.445	1.221
Min. $\sigma_{z,IL}$ (MN/m^2)	-0.514	-0.095	-0.052	-0.031	-0.019
Max. $\sigma_{z,IL}$ (MN/m^2)	11.89	3.697	2.230	1.576	1.169
Min. $\sigma_{z,CF}$ (MN/m^2)	-0.854	-0.583	-0.489	-390	-0.283
Max. $\sigma_{z,CF}$ (MN/m^2)	0.854	0.583	0.496	0.384	0.283
Min. τ_x (KN/m^2)	-121.9	-31.57	-15.40	-9.147	-5.775
Max. τ_x (KN/m^2)	5.994	1.006	0.698	0.319	0.223
Min. τ_y (KN/m^2)	-17.74	-6.861	-4.409	-2.685	-2.350
Max. τ_y (KN/m^2)	17.74	6.861	4.187	2.688	2.271
Max. cycle $\Delta\sigma_i$ (MN/m^2)	0.332	0.192	0.132	0.085	0.058
Fatigue D (1/yr)	$2.80 \cdot 10^{-22}$	$1.47 \cdot 10^{-25}$	$5.49 \cdot 10^{-28}$	$2.03 \cdot 10^{-30}$	$1.75 \cdot 10^{-33}$

B.7. Inflow velocity

This section contains the full range of outputs of the research conducted in Section 5.7. It has to be noted that the outputs considered relevant for this study are listed in the corresponding section.

No inflow velocity

Fig. B.7 and Fig. B.8 show an overview of the states of cross-flow displacement and the frequency density spectrum respectively of a pipe with an inner fluid velocity of 0 m/s.

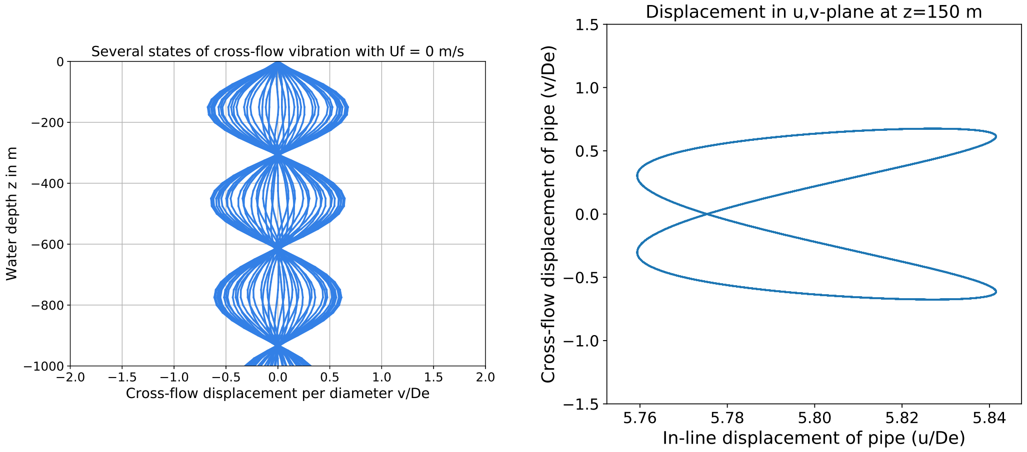

Figure B.7: Several snapshots of the state of the cross-flow vibration of the pipe divided by the diameter(left) and the displacement in the u,v-plane at the point of maximum displacement (right)

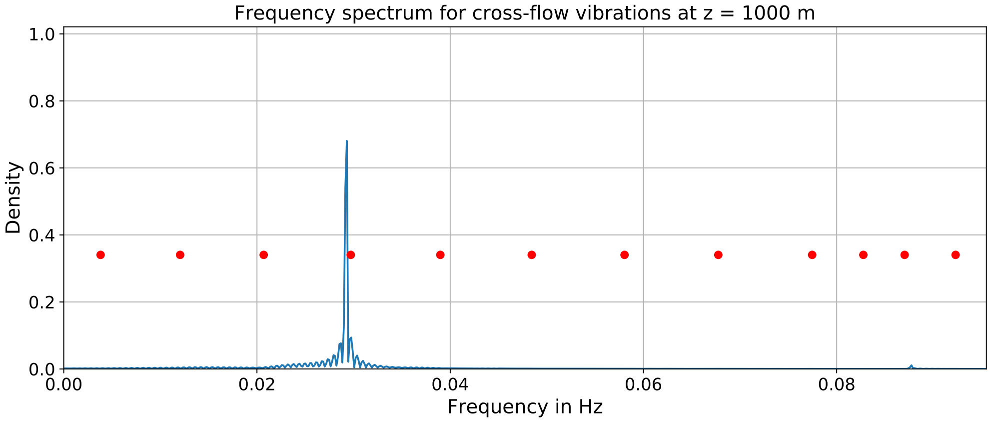

Figure B.8: Frequency density spectrum for the pipe with an inflow velocity of 0 m/s (natural frequencies depicted with red dots)

Varying inflow velocity

Tab. B.10 contains all the outputs for the model simulations with different inflow velocities.

Table B.10: Complete list of outputs gathered from the VIV model with a HDPE pipe with different inflow velocities

Inflow velocity (m/s)	**1.0**	**2.0**	**3.0**
Shedding mode	4	4	4
Max. u/D_e	20.65	20.72	20.81
Max. v/D_e	0.682	0.688	0.695
Min. M_x (kNm)	-48.75	-49.01	-49.35
Max. M_x (kNm)	$2.259 \cdot 10^3$	$2.267 \cdot 10^3$	$2.279 \cdot 10^3$
Min. M_y (kNm)	-356.9	-359.9	-363.1
Max. M_y (kNm)	356.9	359.9	363.1
Min. $F_{s,x}$ (kN)	-13.75	-13.82	-13.91
Max. $F_{s,x}$ (kN)	0.501	0.510	0.520
Min. $F_{s,y}$ (kN)	-3.116	-3.149	-3.186
Max. $F_{s,y}$ (kN)	3.116	3.149	3.186
Min. $\sigma_{z,IL}$ (MN/m^2)	-0.079	-0.080	-0.080
Max. $\sigma_{z,IL}$ (MN/m^2)	3.678	3.692	3.711
Min. $\sigma_{z,CF}$ (MN/m^2)	-0.581	-0.586	-0.591
Max. $\sigma_{z,CF}$ (MN/m^2)	0.581	0.586	0.591
Min. τ_x (KN/m^2)	-25.58	-25.70	-25.88
Max. τ_x (KN/m^2)	9.931	0.949	0.968
Min. τ_y (KN/m^2)	-5.797	-5.857	-5.926
Max. τ_y (KN/m^2)	5.797	5.857	5.926
Max. cycle $\Delta\sigma_i$ (MN/m^2)	0.146	0.148	0.151
Fatigue D (1/yr)	$3.27 \cdot 10^{-27}$	$4.06 \cdot 10^{-27}$	$5.19 \cdot 10^{-27}$

Inflow velocity (m/s)	**4.0**	**5.0**	**6.0**
Shedding mode	4	4	4
Max. u/D_e	20.93	21.09	21.28
Max. v/D_e	0.703	0.712	0.721
Min. M_x (kNm)	-49.75	-50.25	-50.84
Max. M_x (kNm)	$2.294 \cdot 10^3$	$2.312 \cdot 10^3$	$2.335 \cdot 10^3$
Min. M_y (kNm)	-366.7	-370.6	-374.9
Max. M_y (kNm)	366.7	370.6	374.9
Min. $F_{s,x}$ (kN)	-14.04	-14.19	-14.38
Max. $F_{s,x}$ (kN)	0.531	0.541	0.552
Min. $F_{s,y}$ (kN)	-3.229	-3.279	-3.338
Max. $F_{s,y}$ (kN)	3.229	3.279	3.338
Min. $\sigma_{z,IL}$ (MN/m^2)	-0.081	-0.082	-0.083
Max. $\sigma_{z,IL}$ (MN/m^2)	3.736	3.766	3.802
Min. $\sigma_{z,CF}$ (MN/m^2)	-0.597	-0.604	-0.611
Max. $\sigma_{z,CF}$ (MN/m^2)	0.597	0.604	0.611
Min. τ_x (KN/m^2)	-26.11	-26.40	-26.75
Max. τ_x (KN/m^2)	0.987	1.007	1.027
Min. τ_y (KN/m^2)	-6.006	-6.100	-6.209
Max. τ_y (KN/m^2)	6.006	6.100	6.209
Max. cycle $\Delta\sigma_i$ (MN/m^2)	0.154	0.158	0.163
Fatigue D (1/yr)	$7.09 \cdot 10^{-27}$	$1.02 \cdot 10^{-26}$	$1.52 \cdot 10^{-26}$

B.8. Current velocity

This section contains the full range of outputs of the research conducted in Section 5.8. It has to be noted that the outputs considered relevant for this study are listed in the corresponding section.

Uniform

Tab. B.11 contains all the outputs for the model simulations with different current velocities.

Table B.11: Complete list of outputs gathered from the VIV model with a HDPE pipe with different inflow velocities

Current velocity (m/s)	**0.1**	**0.2**	**0.3**	**0.4**
Shedding mode	1	2	3	4
Max. u/D_e	1.288	5.239	11.73	20.74
Max. v/D_e	0.814	0.831	0.733	0.690
Min. M_x (kNm)	-2.029	-11.19	-27.39	-49.11
Max. M_x (kNm)	$0.129 \cdot 10^3$	$0.585 \cdot 10^3$	$1.294 \cdot 10^3$	$2.270 \cdot 10^3$
Min. M_y (kNm)	-58.86	-187.4	-277.5	-360.8
Max. M_y (kNm)	58.78	187.8	277.5	360.8
Min. $F_{s,x}$ (kN)	-0.764	-3.508	-7.834	-13.84
Max. $F_{s,x}$ (kN)	0.031	0.090	0.266	0.513
Min. $F_{s,y}$ (kN)	-0.347	-1.201	-2.071	-3.159
Max. $F_{s,y}$ (kN)	0.347	1.204	2.117	3.159
Min. $\sigma_{z,IL}$ (MN/m^2)	-0.003	-0.018	-0.045	-0.080
Max. $\sigma_{z,IL}$ (MN/m^2)	0.210	0.953	2.108	3.697
Min. $\sigma_{z,CF}$ (MN/m^2)	-0.096	-0.305	-0.452	-0.588
Max. $\sigma_{z,CF}$ (MN/m^2)	0.095	0.306	0.452	0.588
Min. τ_x (KN/m^2)	-1.421	-6.525	-14.57	25.75
Max. τ_x (KN/m^2)	0.058	0.168	0.495	0.954
Min. τ_y (KN/m^2)	-0.644	-2.235	-3.852	-5.877
Max. τ_y (KN/m^2)	0.645	2.238	3.938	5.877
Max. cycle $\Delta\sigma_i$ (MN/m^2)	0.027	0.089	0.128	0.149
Fatigue D (1/yr)	$3.11 \cdot 10^{-38}$	$4.06 \cdot 10^{-30}$	$5.19 \cdot 10^{-28}$	$4.30 \cdot 10^{-27}$
Current velocity (m/s)	**0.5**	**0.6**	**0.7**	**0.8**
Shedding mode	4-5	6	6	6-7
Max. u/D_e	32.46	46.00	63.21	83.01
Max. v/D_e	0.853	0.667	0.778	0.884
Min. M_x (kNm)	-77.05	-108.4	-147.7	-190.4
Max. M_x (kNm)	$3.549 \cdot 10^3$	$5.009 \cdot 10^3$	$6.895 \cdot 10^3$	$8.946 \cdot 10^3$
Min. M_y (kNm)	-458.2	-506.0	-596.1	-689.6
Max. M_y (kNm)	458.4	506.0	596.1	687.0
Min. $F_{s,x}$ (kN)	-21.67	-30.84	-42.42	55.17
Max. $F_{s,x}$ (kN)	0.967	2.080	2.720	5.025
Min. $F_{s,y}$ (kN)	-4.475	-6.359	-7.794	-10.41
Max. $F_{s,y}$ (kN)	4.459	6.359	7.794	10.43
Min. $\sigma_{z,IL}$ (MN/m^2)	-0.125	-0.177	-0.241	-0.310
Max. $\sigma_{z,IL}$ (MN/m^2)	5.779	8.157	11.23	14.63
Min. $\sigma_{z,CF}$ (MN/m^2)	-0.746	-0.824	-0.971	-1.123
Max. $\sigma_{z,CF}$ (MN/m^2)	0.747	0.824	0.971	1.112
Min. τ_x (KN/m^2)	-40.31	-57.37	-78.91	-102.6
Max. τ_x (KN/m^2)	1.799	3.869	5.061	9.348
Min. τ_y (KN/m^2)	-8.294	-11.83	-14.50	-19.37
Max. τ_y (KN/m^2)	8.854	11.83	14.50	19.406
Max. cycle $\Delta\sigma_i$ (MN/m^2)	0.217	0.147	0.194	0.266
Fatigue D (1/yr)	$3.17 \cdot 10^{-25}$	$6.03 \cdot 10^{-27}$	$2.68 \cdot 10^{-25}$	$8.33 \cdot 10^{-24}$

Sheared

Tab. B.12 contains all the outputs for the model simulation with a sheared current velocity profile.

Table B.12: Complete list of outputs gathered from the VIV model with a HDPE pipe with a sheared current velocity profile

Current velocity (m/s)	**0.7 (top) - 0.2 (bottom)**
Max. u/D_e	11.35
Max. v/D_e	0.620
Min. M_x (kNm)	-63.38
Max. M_x (kNm)	$1.724 \cdot 10^3$
Min. M_y (kNm)	-267.2
Max. M_y (kNm)	311.7
Min. $F_{s,x}$ (kN)	-10.646
Max. $F_{s,x}$ (kN)	1.951
Min. $F_{s,y}$ (kN)	-3.361
Max. $F_{s,y}$ (kN)	2.902
Min. $\sigma_{z,IL}$ (MN/m^2)	-0.103
Max. $\sigma_{z,IL}$ (MN/m^2)	2.808
Min. $\sigma_{z,CF}$ (MN/m^2)	-0.435
Max. $\sigma_{z,CF}$ (MN/m^2)	0.507
Min. τ_x (KN/m^2)	-19.8
Max. τ_x (KN/m^2)	3.629
Min. τ_y (KN/m^2)	-6.253
Max. τ_y (KN/m^2)	5.399
Max. cycle $\Delta\sigma_i$ (MN/m^2)	0.135
Fatigue D (1/yr)	$1.41 \cdot 10^{-28}$

C

Model verification

This Appendix is dedicated to the verification of the numerical model. It is impossible to validate the values related to VIV analytically. Therefore it is chosen to verify the drag and the natural frequencies of the pipe to see whether the equations were implemented correctly. In order to perform the check, the values related to time and vertical location were omitted (tension, pressure difference and inner pipe fluid), creating essentially a cantilever beam. Furthermore, the lift force caused by vortex shedding will not be considered. The material of choice is steel. The other parameters can be found in Tab. C.1

Table C.1: Pipe parameters and model parameters for cantilever beam for model verification

Pipe parameters			
Material		Steel	
Length	L	1000	m
Outer diameter	D_e	2.5	m
Wall thickness	t	0.10	m
Pipe material density	ρ_p	7800	kg/m^3
Young's modulus	E	$211 \cdot 10^9$	N/m^2
Seawater and fluid parameters			
Sea water density	ρ_w	1026.6	kg/m^3
Fluid intake density	ρ_f	0	kg/m^3
Fluid intake velocity	U_f	0	m/s
Model parameters			
Element length	Δz	50	m
Drag coefficient	$\hat{C}_{x0}^{0}$	1.1856	-
Current parameters			
Type		Uniform	
Magnitude	V_c	0.2	m/s

C.1. Drag force

The pipe will experience a drag force caused by the current velocity on the pipe. This drag force per meter length is given by part of Morison's equation as:

$$F_d = \frac{1}{2}\rho_w \hat{C}_{x0}^{0} D_e V_c^2 \quad , \tag{C.1}$$

where all the variables are given in Tab. C.1. The maximum displacement of the end of a cantilever beam subjected by a force per meter length is analytically known as:

$$u_{max} = \frac{F_d L^4}{8EI} \quad . \tag{C.2}$$

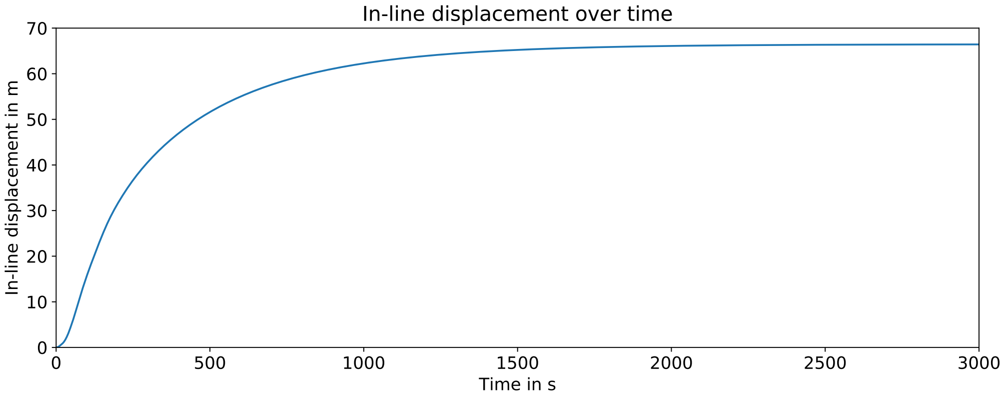

Figure C.1: In-line displacement of pipe end over time

This means that for a current velocity of $V_c = 0.2$ m/s, the analytical maximum displacement for this steel cantilever beam is $u_{max} = 66.30$ m. The numerical maximum in-line displacement can be found from Fig. C.1. As can be seen, the pipe reaches an equilibrium at around 2000 s. The maximum displacement of the numerical displacement of the pipe is 66.43. This is within 0.2% of the analytically determined value. Therefore it can be concluded that the pipe equations have been applied correctly.

C.2. Natural frequencies

Another check that can be performed in order to verify the equations of the model, is seeing whether the numerically determined natural frequencies coincide with the natural frequencies that are determined analytically as in Eq. (4.29). The natural frequencies of the pipe can be numerically determined by setting the density of the ambient flow (seawater) to 0, allowing the pipe to have a free vibration. The pipe is then given an initial displacement, after which it will freely vibrate. The frequency at which the density has peaks are the natural frequencies of the system. Fig. C.2 shows these numerically determined frequencies, along with the analytically determined natural frequencies plotted in red. It can be seen that these values coincide and exceptionally well and therefore it can be concluded that the equations of the pipe model have been applied correctly.

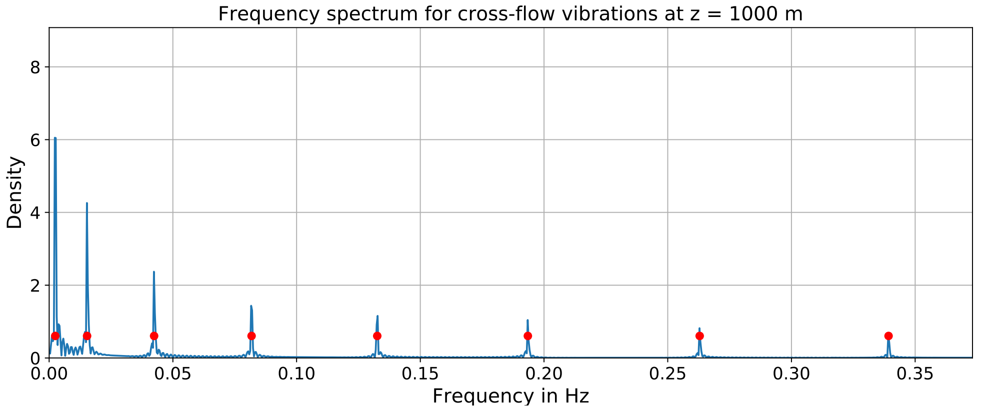

Figure C.2: Frequency density spectrum of free vibrating steel cantilever beam with analytically determined natural frequencies in red

D

Stability of pipe conveying fluid with varying inflow velocity

This Appendix contains the numericals and outputs of the analysis of the stability of the pipe conveying fluid with varying inflow velocity of Chapter 6.

D.1. One-mode approximation

This section shows the numerical values that were used for the one-mode analysis of the stability of the pipe. Tab. D.1 gives a full overview of the model parameters and the numerically calculated integrals.

Table D.1: Model parameters and numerical values used for calculation of stability ranges

Model parameters			
Pipe length	L	1000	m
Pipe outer diameter	D_e	2.5	m
Pipe inner diameter	D_i	2.2	m
Pipe material	-	Steel	-
Young's modulus	E	211	MN/m^2
Pipe density	ρ_p	7800	kg/m^3
Sea water density	ρ_w	1026.6	kg/m^3
Density of inflow fluid	ρ_f	1027.6	kg/m^3
Added mass coefficient	C_a	1.0	-
Computed numerical values			
-	Q_1	108.362	-
Total mass per unit length	m_tot	17583.4	kg/m
Natural frequency first mode	ω_1	0.01067	rad/s
-	$\int_0^L \phi_1 \phi_1'' dz$	$9.301 \cdot 10^-5$	-